AN EXPERIMENTAL AND FINITE ELEMENT INVESTIGATION OF ADDED MASS EFFECTS ON SHIP STRUCTURES

By

DAVID GEORGE GLENWRIGHT

B.A.Sc., The University of British Columbia, 1985

A THESIS SUBMITTED IN PARTIAL FULFILLMENT OF

THE REQUIREMENTS FOR THE DEGREE OF

MASTER OF APPLIED SCIENCE

in

THE FACULTY OF GRADUATE STUDIES

Department of Mechanical Engineering

We accept this thesis as conforming

to the required standard

THE UNIVERSITY OF BRITISH COLUMBIA

September 1987

4 6

In presenting this thesis in partial fulfilment of the requirements for an advanced degree at the University of British Columbia, I agree that the Library shall make it freely available for reference and study. I further agree that permission for extensive copying of this thesis for scholarly purposes may be granted by the head of my department or by his or her representatives. It is understood that copying or publication of this thesis for financial gain shall not be allowed without my written permission.

Department of Mechanical Engineering

The University of British Columbia
1956 Main Mall
Vancouver, Canada
V6T 1Y3

Date September 15, 1987

DE-6(3/81)

ABSTRACT

The Experimental and Finite Element Investigation of Added Mass Effects on Ship Structures comprised three phases : 1) investigation of the fluid modelling capabilities of the Finite Element Program VAST, 2) experimental investigation to determine the effect of the fluid on the lowest natural frequencies and mode shapes of a ship model, and 3) comparison of these experimental results with numerical results obtained from VAST. The fluid modelling capabilities of VAST were compared with experimental results for submerged vibrating plates, and the effect of fluid element type and mesh discretization was considered. In general, VAST was able to accurately predict the frequency changes caused by the presence of the fluid. Experimental work both in air and water was performed on a ship model. The lowest four modes of vertical, horizontal, and torsional vibration were identified, and the effect of draught on the frequencies and mode shapes was recorded. When the experimentally obtained frequencies and mode shapes for the ship model were compared with the numerical predictions of VAST, good agreement was found in both air and water tests for the vertical vibration modes.

TABLE OF CONTENTS

Page

Page

LIST OF TABLES

Page

Page

LIST OF FIGURES

Page

Page

Page

Page

Page

Page

NOMENCLATURE

Matrices and vectors are denoted by boldface type.

[ ]	Rectangular or Square Matrix
{ }	Column Vector
$[\ ]^{-1}$	Matrix Inverse
$[\ ]^{T}$	Matrix Transpose
$\cdot$	Time Differentiation; $\dot{u} = \frac{\partial u}{\partial t}$
$\cdot\cdot$	Time Differentiation; $\ddot{u} = \frac{\partial^2 u}{\partial^2 t}$
∇^2	Laplacian Operator
a	Span Length of Plate
b	Cord Length of Plate
D	Extent of Fluid Domain
E	Young's Modulus
E	Energy in Fluid
g	Acceleration Due to Gravity
I	Moment of Inertia
[J]	Jacobian Matrix
[K]	Stiffness Matrix
N	Shape Functions
M	Moment

$[M]$	Mass Matrix
$[M_A]$	Added Mass Matrix
$[M_S]$	Structural Mass Matrix
p	Pressure in the Fluid
t	Plate Thickness
u	Displacement
v	Velocity
x, y, z	Cartesian Coordinates
$\beta_i l$	Constant for Vibration that depends on the end conditions of the beam
ϵ	Strain
ϕ	Velocity Potential
ρ	Density
ω_i	Frequency of mode i
Ψ_i	Eigenvector of mode i
π	3.1415926536 . . .
ν	Poisson's Ratio
K	Bulk Modulus of Fluid
u_y	Amplitude of a Surface Wave
λ	Wave Length
ξ, η, ζ	Isoparametric Coordinates

ACKNOWLEDGEMENT

I would like to thank my advisor, Dr. Stanley G. Hutton, Department of Mechanical Engineering, University of British Columbia for his support and guidance throughout the work on this thesis. I would also like to thank Alan Steeves, Department of Mechanical Engineering, University of British Columbia without whom much of the computer work contained in this thesis would never have been completed. As well, I would like to thank Gerry N. Stensgaard, Manager of B.C. Research, Ocean Engineering Department, for allowing me access to their towing tank in which the water tests on the model were conducted.

This work was funded through Contract Serial Number 9 SC 97727-4-6248 with Defence Research Establishment Atlantic (D.R.E.A.) Department of National Defence.

1 INTRODUCTION

1.1 BACKGROUND

Naval architects have long recognized the fact that fluid affects the vibration characteristics of ships. The exact solution to the equations of motion of a flexible structure involves solving a system of equations in which the fluid and structure are coupled. Not only does the fluid coupling introduce many complications, but the fact that the ship is not uniform further complicates the task.

The general equations of motion of the ship girder vibrating in a fluid have been recently developed by Bishop and Price [9-13]. The equations they present deal with the ship girder and attempt to account for the effects of shear deflection, rotary inertia, and warping on the frequencies and mode shapes of the beam. They assume that the effect of the fluid may be expressed as distributed forces exerted on the beam.

Daidola [16] presents a solution to the equations of motion for a uniform circular Euler beam in vertical vibration, ignoring the effects of shear deflection and rotary inertia. He solves the three-dimensional Laplace equation for the velocity potential as a function of position along the length of the beam, time, and the unknown deflection shape (mode shape) of the beam. The effective force is then determined from the linearized Bernoulli equation (see Chapter 2) and inserted into the Euler equation of the beam.

The concept of an added mass to account for the effect of the fluid, which could be incorporated into the simple beam equations, was first introduced by F.M. Lewis [27] in 1929 and independently by J.L. Taylor [38] in 1930. Until that time, ship vibration had been dealt with by using data from sister ships and/or empirical formulas. Lewis and Taylor proposed a method which accounted for the inertia effects of the fluid and allowed the two and three node vertical vibration modes to be analytically calculated. Lanweber and Macagno [26] extended the method to include horizontal vibration modes. Taylor [38] similarly developed J-factors for horizontal vibration in the presence of a free surface. Subsequently, various authors have either extended this method by developing more analytic procedures [25,26], or they have widened the range of applicability by introducing a mode dependent J-factor to account for the three-dimensional effects of the fluid [2,23,40].

There has been very little experimental work done in this field. Moullin, Browne, and Perkins [31] in 1930 were the first to perform experiments on prisms made of wood. However, these prisms were not allowed to float freely in water but were suspended from the underside of a steel bar. This arrangement allowed various levels of immersion to be examined. They compared their results with those of their contemporary, Lewis and they found that the experimentally added masses were below those predicted by Lewis's method.

In 1962, Burrill, Robson, and Townsin [14] reported experimental work that had been performed with prismatic bars of various constant cross-sections over their length of 120 inches. These bars were made of an aluminium alloy so that the entrained water masses would be relatively high in relation to the weight of the bars in air. Their experimental procedure was similar to Moullin et al, in that these bars were suspended at their nodal locations, and the level of water in the tank was varied in order to give the desired draughts. The results showed that the added mass fell between that derived by Lewis and that of Taylor. Further experimental work was performed by Townsin in 1969 [40], and he published an empirical formula for the three-dimensional correction factor known as the J-factor.

In 1960, Kuo published his PhD Thesis [24] in which he conducted experimental work on a scale model of a ship. Unlike the other experimental work, Kuo's model was constructed from acrylic. These results were very interesting, as Kuo made what would seem to be the first attempt to scale the vibration characteristics of a real ship. His results for the 2-node vertical bending mode agreed very well with Lewis's method, but as mode number was increased, the agreement began to deteriorate. He explained this deterioration as being due to the effects of the real three-dimensional flow around the hull and the lack of precision in the calculation of the added mass for a section.

There has been tremendous progress recently in the development of the Finite Element Method [15,45], and it now can be applied to the ship structure, yielding complex three-dimensional finite element models involving many thousand degrees of freedom [4,5,35,37]. These models seem to adequately model the stiffness, rigidity, and mass distribution of the structure. But to extend finite elements to include the fluid-structure interaction problem, the structural mass must be matched by a comparable technique in the fluid to determine an added mass matrix.

Various authors have presented different methods that allow the Finite Element Method to handle the fluid-structure interaction problem. Zienkiewicz and Bettess [46,47], Armand [4], Orsero [35], and Kiefling [21] have proposed a standard finite element discretization of the fluid in which the three-dimensional Laplace equation is solved, from which an added mass matrix is determined and added to the structural mass matrix of the elements in contact with the fluid. As well, Beer and Meek [6], Bettess [7], and Zienkiewiz and Bettess [47] have proposed the use of infinite fluid elements to reduce the size of the finite element fluid matrices. Hylarides and Vorus [19,43] have proposed a panel source distribution to derive the added mass of the vibrating ship hull. Deruntz and Geers [17] and Zienkiewicz, Kelly, and Bettess [48] have also proposed boundary element solution procedures which can determine the added mass matrix that in turn is added to the structural mass matrix. All of these methods are very similar; they all produce an added mass matrix which is added to the structural mass matrix, followed by solving for the vibration characteristics of the structure.

1.2 Purpose and Scope

The purpose of the work detailed in this thesis was three-fold. First, the fluid modelling capabilities of the Finite Element Program VAST were investigated. This was done by comparing the frequencies predicted by VAST with experimental results found in the literature for vibrating cantilever plates in a fluid. The effect of the extent of the fluid domain, the degree of discretization, and the type of fluid element used were examined. Second, experimental investigations were conducted to determine the effect of the fluid on the lowest natural frequencies and mode shapes of a ship-like model. Finally, these experimental results were compared with analytical results obtained from VAST for the vibration characteristics of this ship-like model.

2. THEORY

This chapter will present the equations of motion that describe the vibration response of a structure in the presence of a fluid. These equations are based upon the assumption of an inviscid, incompressible, and irrotational fluid. Having developed the differential equations defining the continuum problem, the finite element equations that are used by VAST are presented here.

2.1 Continuum Formation

The fluid is assumed to be incompressible and inviscid, and the flow irrotational. As a result, the fluid motion can be described by a velocity potential $\phi = \phi(x,y,z)$, which satisfies Laplace's equation

$$\nabla^2\phi = 0 \qquad (2.1)$$

Bernoulli's equation, (Newman [34] and Armand [4]), can be expressed as

$$\frac{\partial\phi}{\partial t} + \frac{p}{\rho} + V + \frac{q^2}{2} = C(t) \qquad (2.2)$$

where p is the pressure, ρ the fluid density, $q = \sqrt{v_x^2 + v_y^2 + v_z^2}$ the velocity, V the potential of the applied external forces per unit volume, and C(t) an integration function that may be a function of time.

If gravity is the only external force, V is a linear function of y and represents the hydrostatic pressure. If only the hydrodynamic forces are of concern, V may be neglected. C(t) may be chosen arbitrarily and can be set equal to zero, as will be done in this analysis. If motions are small enough, such that q^2 is a second order term, the linearized Bernoulli's equation becomes

$$\frac{\partial \phi}{\partial t} + \frac{p}{\rho} = 0 \tag{2.3}$$

Rearranging terms gives

$$p = -\rho \frac{\partial \phi}{\partial t} \tag{2.4}$$

From continuity

$$\frac{\partial v_x}{\partial x} + \frac{\partial v_y}{\partial y} + \frac{\partial v_z}{\partial z} = \frac{1}{K}\frac{\partial p}{\partial t} \tag{2.5}$$

where v_x, v_y, and v_z are the velocities in the x, y, and z directions, respectively, and K is the bulk modulus of the fluid. Noting that

$$\frac{\partial \phi}{\partial x} = v_x \quad \frac{\partial \phi}{\partial y} = v_y \quad \frac{\partial \phi}{\partial z} = v_z \tag{2.6}$$

and combining equations 2.5 and 2.6 yields

$$\nabla^2 \phi - \frac{1}{K}\frac{\partial p}{\partial t} = 0 \tag{2.7}$$

Taking the derivative of equation 2.4 with respect to time, and substituting into equation 2.7 results in

$$\nabla^2\phi + \frac{\rho}{K}\ddot{\phi} = 0 \tag{2.8a}$$

Alternatively, equation 2.8a can be expressed in terms of the pressure, such that

$$\nabla^2 p + \frac{\rho}{K}\ddot{p} = 0 \tag{2.8b}$$

Since the fluid is incompressible, equations 2.8a,b reduce to

$$\nabla^2\phi = 0 \tag{2.9a}$$

$$\nabla^2 p = 0 \tag{2.9b}$$

which must be satisfied at every point inside the fluid domain.

The Finite Element Method will be used to solve 2.9a, with the boundary conditions described below. The developed equation assumes an inviscid, incompressible, and irrotational fluid flow. These limitations affect the finite element's ability to represent the real flow in the fluid around a vibrating structure. (The development of the Finite Element Theory is presented in Section 3.2.)

At the fluid-structure interface, the fluid must always be in contact with the structure; and hence, the velocity of the fluid normal to the structure must be equal to the velocity of the structure at that point, given by

$$\frac{\partial\phi}{\partial n} = v_n = \dot{u}_n \tag{2.10a}$$

or in terms of the pressure using equation 2.4

$$\frac{\partial p}{\partial n} = -\rho \ddot{u}_n \tag{2.10b}$$

The equilibrium condition for the free surface ($y = 0$) is

$$p = \rho g u_y \tag{2.11}$$

where u_y is the amplitude of a wave on the free surface. This equation may be further developed by noting that from equation 2.4 and 2.6

$$\ddot{u}_y = \dot{v}_y = -\frac{1}{\rho}\frac{\partial p}{\partial y}$$

which in turn yields

$$\frac{\partial p}{\partial y} = \frac{1}{g}\ddot{p} \tag{2.12a}$$

A corresponding equation dealing with ϕ may be developed by examining the amplitude u_y of the waves on the free surface, such that

$$\dot{u}_y = \frac{\partial \phi}{\partial y}$$

and

$$u_y = -\frac{1}{g}\frac{\partial \phi}{\partial t}$$

Combining the two above equations leads to

$$\frac{\partial \phi}{\partial y} = \frac{1}{g}\ddot{\phi} \tag{2.12b}$$

If $\phi(x,y,z,t) = \phi(x,y,z)e^{iwt}$

$$\phi = \frac{g}{\omega^2}\frac{\partial \phi}{\partial y} \tag{2.13}$$

which is the free surface boundary condition expressed in terms of the velocity potential ϕ. For most structural vibrations, $\omega^2 >> g$. More accurately, one should look at $\omega^2 l/g$ (where l is the characteristic length of the body), since ω and g are dimensional quantities. A good approximation of equation 2.13 on the free surface is

$$\phi = 0 \tag{2.14a}$$

Similarly, on the free surface

$$p = 0 \tag{2.14b}$$

Equations 2.14a,b assume that any surface waves generated are negligible. This is a safe assumption if : 1) the structure is completely submerged at a large distance from the free surface; and 2) the structure is floating and the wavelength λ of the generated waves is less than the characteristic dimension l of the structure, which for ships would be the beam.

For a finite element discretization of the fluid, the infinite boundary has to be truncated at some large distance from the structure. At this imposed boundary, a suitable condition is nonreflection of waves, given by

$$\frac{\partial p}{\partial n} = 0 \quad \text{or} \quad \phi = 0 \tag{2.15}$$

as these waves are generated by the structure and finally absorbed by the fluid.

The equations of motion for the coupled fluid-structure interaction are

$$[M(x,y,z)]\begin{Bmatrix} \ddot{u} \\ \ddot{v} \\ \ddot{w} \end{Bmatrix} + [K(x,y,z)]\begin{Bmatrix} u \\ v \\ w \end{Bmatrix} = F(t) \tag{2.16}$$

$$\nabla^2\phi(x,y,z) = 0 \tag{2.17}$$

F(t) is given by the pressure distribution of the fluid on the structure as

$$F(t) = \int_S p(x,y,z,t)dS$$

$$p(x,y,z,t) = -\rho\frac{\partial}{\partial t}\phi(x,y,z)$$

$$F(t) = -\rho\int_S \frac{\partial}{\partial t}\phi(x,y,z)dS \tag{2.18}$$

When there is no fluid, there is no pressure on the structure from the fluid, and F(t) becomes zero. Equation 2.16 simplifies to the standard equation of motion for a structure.

2.2 Finite Element Formulation

It is possible to solve numerically using finite elements for the velocity potential in the fluid and then use this information to determine the force that is exerted on the structure from the fluid, thus solving the coupled fluid-structure interaction problem. The theory will be presented below [4,22,36,37,48].

The variational principle that governs this problem is given by

$$\delta\iiint \frac{1}{2}\left[\left(\frac{\partial\phi}{\partial x}\right)^2+\left(\frac{\partial\phi}{\partial y}\right)^2+\left(\frac{\partial\phi}{\partial z}\right)^2\right]dxdydz - \delta\iint \frac{\partial\phi}{\partial n}\,\phi\, dS_n = 0 \quad (2.19)$$

where ϕ is the velocity potential, dS_n the interface surface area, and v_n the velocity normal to S_n. The velocity potential is zero at the boundaries and on the free surface. (This functional is shown to be the correct one for this problem in Appendix A.)

Proceeding with the finite element idealization of the surrounding fluid, the fluid domain is divided into three-dimensional finite elements. The velocity potential ϕ_e within each element is expressed in terms of the nodal values as

$$\phi_e = \sum_{i=1}^{NNE} N_i \phi_i \quad (2.22)$$

where NNE is the number of fluid nodes in an element, the N_i are the shape functions, and ϕ_i is the velocity potential at node i (which is to be determined). The first term of equation 2.19 for one element may be expressed as

$$\delta\iiint \frac{1}{2}\begin{Bmatrix}\frac{\partial\phi}{\partial x}\\ \frac{\partial\phi}{\partial y}\\ \frac{\partial\phi}{\partial z}\end{Bmatrix}_e^T \begin{bmatrix}1 & & \\ & 1 & \\ & & 1\end{bmatrix} \begin{Bmatrix}\frac{\partial\phi}{\partial x}\\ \frac{\partial\phi}{\partial y}\\ \frac{\partial\phi}{\partial z}\end{Bmatrix}_e dxdydz \quad (2.23)$$

Using equation 2.22, an expression can be determined

$$\begin{Bmatrix} \dfrac{\partial\phi}{\partial x} \\ \dfrac{\partial\phi}{\partial y} \\ \dfrac{\partial\phi}{\partial z} \end{Bmatrix}_e = [J]^{-1} \begin{bmatrix} \dfrac{\partial N_1}{\partial\xi} & \dfrac{\partial N_2}{\partial\xi} & \cdots & \dfrac{\partial N_{NNE}}{\partial\xi} \\ \dfrac{\partial N_1}{\partial\eta} & \dfrac{\partial N_2}{\partial\eta} & \cdots & \dfrac{\partial N_{NNE}}{\partial\eta} \\ \dfrac{\partial N_1}{\partial\zeta} & \dfrac{\partial N_2}{\partial\zeta} & \cdots & \dfrac{\partial N_{NNE}}{\partial\zeta} \end{bmatrix} \begin{Bmatrix} \phi_1 \\ \phi_2 \\ \vdots \\ \phi_{NNE} \end{Bmatrix}$$

$$= [B]\{\phi\}_e \tag{2.24}$$

where $[J]$ is the Jacobian Matrix and $(\xi\ \eta\ \zeta)$ are the local curvilinear coordinates of the element. The volume dxdydz of one element can be expressed as

$$dxdydz = |J|\,d\xi d\eta d\zeta \tag{2.25}$$

After combining equations 2.23, 2.24, and 2.25, the first term of the functional becomes

$$\delta\{\phi\}_e^T \left[\int_{-1}^{1}\int_{-1}^{1}\int_{-1}^{1} \frac{1}{2}\,[B]^T[B]\,|J|\,d\xi d\eta d\zeta\right]\{\phi\}_e \tag{2.26}$$

Or, setting

$$[H]_e = \int_{-1}^{1}\int_{-1}^{1}\int_{-1}^{1} \frac{1}{2}\,[B]^T[B]\,|J|\,d\xi d\eta d\zeta \tag{2.27}$$

and simplifying, the first term of equation 2.19 becomes

$$\delta\{\phi\}_e^T[H]_e\{\phi\}_e \tag{2.28}$$

Integrating over the whole fluid domain, which has been divided into NFE fluid elements, the first term of the functional becomes

$$\delta\iiint \frac{1}{2}\left[\left(\frac{\partial\phi}{\partial x}\right)^2 + \left(\frac{\partial\phi}{\partial y}\right)^2 + \left(\frac{\partial\phi}{\partial z}\right)^2\right]dxdydz = \sum_{e=1}^{NFE} \delta\{\phi\}_e^T[H]_e\{\phi\}_e$$

$$= \{\phi\}^T[H]\{\phi\} \tag{2.29}$$

The second term of the variational principle remains to be calculated. The boundary conditions that exist for each fluid element that comes in contact with the structure's surface must be introduced, namely

$$\frac{\partial \phi}{\partial n} = v_n = \dot{u}_n \tag{2.10}$$

The second term of equation 2.19 then becomes

$$\delta \iint \frac{\partial \phi}{\partial n} \phi \, dS_n = \delta \iint v_n \phi \, dS_n \tag{2.30}$$

At the interface, the velocity potential ϕ and the normal velocity v_n can be expressed in terms of their nodal values, using the relations

$$\phi = \sum_{i=1}^{NI} N_i \phi_i \tag{2.31}$$

$$v_n = \sum_{i=1}^{NI} N_i v_{n_i} \tag{2.32}$$

where the N_i are the shape functions of the interface elements, ϕ_i is the velocity potential of the fluid, v_{n_i} is the normal velocity of the structure at node i, and NI is the number of nodes in an interface element.

The shape functions used for the interface elements are the two-dimensional projections of those used for the full three-dimensional velocity potential field, with the local curvilinear coordinate ζ set equal to one. (See Appendix B.) Thus, equation 2.30 for one interface element can be expressed as

$$\delta\{\phi\}_e^T \left[\iint \begin{Bmatrix} N_1 \\ N_2 \\ \vdots \\ N_{NI} \end{Bmatrix} \{N_1 N_2 \cdots N_{NI}\} dS_n \right] \{v_n\}_e \tag{2.33}$$

Further, dS_n can be expressed in terms of the curvilinear coordinates (ξ,η) as

$$\begin{aligned} dS_n &= \cos(n,x)dydz + \cos(n,y)dxdz + \cos(n,z)dxdy \\ &= \cos(n,x)|J_1|d\xi d\eta + \cos(n,y)|J_2|d\xi d\eta + \cos(n,z)|J_3|d\xi d\eta \end{aligned} \tag{2.34}$$

with

$$\begin{aligned} |J_1| &= \det\begin{bmatrix} \partial y/\partial\xi & \partial z/\partial\eta \\ \partial y/\partial\eta & \partial z/\partial\eta \end{bmatrix} \\ |J_2| &= \det\begin{bmatrix} \partial z/\partial\xi & \partial x/\partial\eta \\ \partial z/\partial\eta & \partial x/\partial\eta \end{bmatrix} \\ |J_3| &= \det\begin{bmatrix} \partial x/\partial\xi & \partial y/\partial\eta \\ \partial x/\partial\eta & \partial y/\partial\eta \end{bmatrix} \end{aligned} \tag{2.35}$$

Combining equations 2.33, 2.34, and 2.35 gives

$$\delta\{\phi\}_e^T \left[\int_{-1}^{1}\int_{-1}^{1} \begin{Bmatrix} N_1 \\ N_2 \\ \vdots \\ N_{NI} \end{Bmatrix} \{N_1 N_2 \cdots N_{NI}\} dS_n \right] \{v_n\}_e = \delta\{\phi\}_e^T [\bar{F}]_e \{v_n\}_e \tag{2.36}$$

where

$$[\bar{F}]_e = \left[\int_{-1}^{1}\int_{-1}^{1} \begin{Bmatrix} N_1 \\ N_2 \\ \vdots \\ N_{NI} \end{Bmatrix} \{N_1 N_2 \cdots N_{NI}\} dS_n \right] \tag{2.37}$$

It now remains to express the normal velocity in terms of the displacements of the structure. This can be done by the transformation

$$\{v_n\}_e = [T]_e\{\dot{u}\}_e \qquad (2.38)$$

where

$$[T]_e = \begin{bmatrix} [T_1]_e & & & \\ & [T_2]_e & & \\ & & \ddots & \\ & & & [T_{NI}]_e \end{bmatrix} \qquad (2.39)$$

In equation 2.39, $[T_i]_e$ contains the direction cosines for node i, such that

$$[T_i]_e = [\cos(n,x)_i \ \cos(n,y)_i \ \cos(n,z)_i] \qquad (2.40)$$

Substituting equation 2.38 into 2.36 yields

$$\delta\{\phi\}_e^T[\bar{F}]_e\{v_n\}_e = \delta\{\phi\}_e^T[\bar{F}]_e[T]_e\{\dot{u}\}_e = \delta\{\phi\}_e^T[F]_e\{\dot{u}\}_e \qquad (2.41)$$

with

$$[F]_e = [\bar{F}]_e[T]_e \qquad (2.42)$$

After integrating equation 2.41 over the interface surface, the second term of the variational principle becomes

$$\delta\iint \frac{\partial\phi}{\partial n}\phi \ dS_n = \sum_{e=1}^{NIE}\delta\{\phi\}_e^T[F]_e\{\dot{u}\}_e = \delta\{\phi_I\}^T[F]\{\dot{u}\} \qquad (2.43)$$

where NIE is the total number of interface elements, $\{\phi_I\}$ the velocity potential of the interface nodes, $\{\dot{u}\}$ the velocity of the interface nodes in terms of the global coordinates, and [F] the assembled interface matrix. Combining equations 2.29 and 2.43 gives

$$\delta\{\phi\}^T[H]\{\phi\} - \delta\{\phi_I\}^T[F]\{\dot{u}\} = 0 \qquad (2.44)$$

and partitioning the matrices [H] and [F] with respect to the interface terms yields

$$\delta\begin{Bmatrix}\phi_R\\ \phi_I\end{Bmatrix}^T \begin{bmatrix}H_{RR} H_{RI}\\ H_{IR} H_{II}\end{bmatrix}\begin{Bmatrix}\phi_R\\ \phi_I\end{Bmatrix} = \delta\{\phi_I\}^T[F]\{\dot{u}\} \tag{2.45}$$

After simplification, equation 2.45 becomes

$$\begin{bmatrix}H_{RR} H_{RI}\\ H_{IR} H_{II}\end{bmatrix}\begin{Bmatrix}\phi_R\\ \phi_I\end{Bmatrix} = \begin{Bmatrix}0\\ [F]\{\dot{u}\}\end{Bmatrix} \tag{2.46}$$

The above equation describes the coupled fluid-structure interaction problem in terms of the nodal velocity potential of the fluid $\{\phi_R\}$, $\{\phi_I\}$ and the nodal velocities of the structure $\{\dot{u}\}$. [H] has units of length (L), while [F] has those of area (L^2); so, equation 2.46 has units of length^3/time (L^3T^{-1}).

Equation 2.46 can be further reduced to

$$\{\phi_I\} = [H^*]^{-1}[F]\{\dot{u}\} \tag{2.47}$$

with $[H^*]$ being the reduced fluid matrix given by

$$[H^*] = [H_{II}] - [H_{IR}][H_{RR}]^{-1}[H_{RI}] \tag{2.48}$$

The next step is to solve for the pressure on the fluid-structure interface. Since the velocity potential $\{\phi_I\}$ is known at this interface, the pressure may be determined from

$$\{p\} = -\rho\frac{\partial\phi}{\partial t} \tag{2.4}$$

$$\{p\} = -\rho\frac{\partial\phi}{\partial t} = -\rho\,[H^*]^{-1}[F]\{\ddot{u}\} \tag{2.49}$$

where {p} is the vector containing the interface pressures, ρ the fluid density, and $\{\ddot{u}\}$ the vector containing the accelerations of the interface nodes of the structure.

The equation of motion for the structure is

$$[M_S]\{\ddot{u}\} + [C]\{\dot{u}\} + [K]\{u\} = \{F_s\} + \{R_f\} \tag{2.50}$$

where $[M_S]$ is the structural mass matrix of the dry structure, $[C]$ the dry damping matrix of the structure, $[K]$ the stiffness matrix of the dry ship, $\{F_s\}$ the vector of external excitation, and $\{R_f\}$ the vector of hydrodynamic nodal forces acting on the fluid-structure interface.

The hydrodynamic nodal forces $\{R_f\}$ may be determined from virtual work arguments. The virtual displacement of an element in the structure is given as

$$\delta\{u_n\}_e = [N]^T_e \delta\{U_n\}_e \tag{2.51}$$

where the subscript n refers to the normal of the variable, and N are the shape functions as before. The pressure distribution within each element is given as

$$\{p^*\}_e = [N]^T_e \{p\}_e \tag{2.52}$$

The work done by the pressure on the interface due to this virtual displacement is

$$\delta W_e = - \iint \{p^*\}_e \delta\{u_n\}_e \, dS_e \tag{2.53}$$

Replacing $\{p^*\}$ and $\delta\{u_n\}_e$ by their expressions given above yields

$$\delta W_e = - \delta\{U_n\}_e^T \left[\iint \{N\}^T_e \{N\}_e \, dS_e \right] \{p\}_e \tag{2.54}$$

The work done by the nodal forces $\{R_{fn}\}_e$ moving through a virtual displacement $\delta\{U_n\}_e$ can be expressed as

$$\delta W_e = \delta\{U_n\}_e^T\{R_{fn}\}_e \tag{2.55}$$

Equating equations 2.54 and 2.55 and noting that

$$[\bar{F}]_e = \iint \{N\}_e\{N\}_e^T \, dS_e \tag{2.37}$$

an expression relating pressure and the nodal forces may be obtained, namely

$$\{R_{fn}\}_e = - [\bar{F}]_e^T\{p\}_e \tag{2.56}$$

But

$$\{R_f\}_e = [T]_e\{R_{fn}\}_e \tag{2.57}$$

so equation 2.56 becomes

$$\{R_f\}_e = - [F]_e^T\{p\}_e \tag{2.58}$$

Integrating over the interface area and substituting the expression for

$$\{p\} = - \rho [H^*]^{-1}[F]\{\ddot{u}\} \tag{2.49}$$

gives

$$\{R_f\} = - \rho [F]^T[H^*]^{-1}[F]\{\ddot{u}\} \tag{2.59}$$

Finally, substituting this expression for $\{R_f\}$ into equation 2.50 yields

$$[M_S]\{\ddot{u}\} + [C]\{\dot{u}\} + [K]\{u\} = \{F_s\} - \rho[F]^T[H^*]^{-1}[F]\{\ddot{u}\} \tag{2.60}$$

$$\left([M_S] + [M_A]\right)\{\ddot{u}\} + [C]\{\dot{u}\} + [K]\{u\} = \{F_s\} \tag{2.61}$$

where the added mass matrix $[M_A]$ is given by

$$[M_A] = \rho[F]^T[H^*]^{-1}[F] \tag{2.62}$$

The interface matrix [F] has 3*NIN columns and NIN rows, while the reduced fluid matrix $[H^*]$ is square, with NIN columns and NIN rows. The multiplication expressed in equation 2.62 produces an added mass matrix $[M_A]$ that is square, with 3*NIN columns and 3*NIN rows. Since the matrix $[H^*]$ is symmetric and full, the added mass matrix is also symmetric and full. These characteristics have profound effects on the numerical solution of equation 2.61. The structural mass matrix $[M_S]$ is well behaved in that it is symmetric and banded, with the bandwidth being small in comparison to the total size of the matrix. However, the added mass matrix is not banded. Therefore, when the added mass matrix is added to the structural mass matrix, the banding is lost and the solution time greatly increased.

There are two major assumptions in the above derivation of the coupled fluid-structure problem that greatly simplify the equations : 1) the fluid is incompressible, and 2) there are no waves generated on the free surface. If the fluid is compressible, then equation 2.8 cannot be simplified as before, and it remains

$$\nabla^2\phi + \frac{1}{K}\ddot{\phi} = 0 \qquad (2.8)$$

Futhermore, if surface waves are admitted, then equation 2.13 also cannot be simplified, and it remains

$$\phi = \frac{g}{\omega^2}\frac{\partial\phi}{\partial y} \qquad (2.13)$$

These two assumptions lead to the following complications of the equations of motion for the fluid. The simplified equation

$$[H]\{\phi\} = \begin{Bmatrix} 0 \\ [F]\{\dot{u}\} \end{Bmatrix} \tag{2.46}$$

becomes

$$[H]\{\phi\} + [E]\{\ddot{\phi}\} = \begin{Bmatrix} 0 \\ [F]\{\dot{u}\} \end{Bmatrix} \tag{2.63}$$

where [H] and [F] are as before and

$$[E]_e = \frac{1}{g}\int_{\Gamma_s} \{N\}_e\{N\}_e^T d\Gamma + \frac{1}{c^2}\int_{\Omega} \{N\}_e\{N\}_e^T d\Omega \tag{2.64}$$

where Γ_s is the free surface and Ω is the whole fluid domain. The first term of equation 2.64 accounts for surface wave considerations. The second term allows the fluid to be compressible. The inclusion of the terms in equation 2.64 introduces the dependence of the fluid solution on the frequency of vibration of the structure.

2.3 Infinite Fluid Element Formulation

The motivation for using infinite fluid elements is that the fluid domain in the fluid-structure dynamic interaction problem is often very large in comparison to the structure's domain. When conventional fluid elements (discussed above) are used, the fluid mesh is extended to some large distance from the body, and the boundary condition of $\phi = 0$ is imposed. The disadvantages of this extension are two-fold. First, there is a large increase in the size of the problem which increases CPU time. Second, if the boundary is not far enough away, the results will be in error. A large number of nodes will be needed in modelling the region where the change in ϕ is small. The infinite element can deal with this situation very well. This element extends to infinity in one direction, permitting this situation to be modelled with one infinite element.

The infinite elements are very similar to the fluid elements described above, but they have two main differences. In one of the local curvilinear directions ξ, the shape functions have a singularity at $\xi = +1$. Also, the velocity potential ϕ is only interpolated along the finite boundary. In the infinite direction, the velocity potential ϕ is assumed to decay from its value at the finite boundary to zero at the infinite boundary. Within the fluid element, the velocity potential ϕ_e may be expressed in terms of the nodal values, such that

$$\phi_e = \sum_{i=1}^{NNE} \bar{M}_i \phi_i \tag{2.65}$$

where ϕ_i are the nodal values of the velocity potential and $\bar{M}_i$ are the modified shape functions given as

$$\bar{M}_i = N_i f(q) \tag{2.66}$$

Here, N_i are the shape functions, which interpolate along the finite boundary, and $f(q)$ is the decay function, which may be of the form

$$f(q) = e^{Q-q} \qquad\qquad f(q) = \left(\frac{Q}{q}\right)^n \tag{2.67}$$

Both of these functions tend toward zero as $q \to \infty$. The choice of which $f(q)$ to use, decay length Q, and power n (if applicable) determines how quickly the function decays. From this point on, there is no difference between this formulation and the one presented above (in Section 2.2).

3. NUMERICAL EVALUATION OF FLUID ELEMENT MODELLING CAPABILITIES

This chapter will describe the numerical work that was performed in evaluating the finite element fluid modelling capabilities of the Finite Element Program VAST. Three different fluid elements were investigated : the 8-noded fluid element, the 20-noded fluid element, and the 8-noded infinite fluid element. (Details of these elements are given in Appendix B.)

The evaluation of the fluid elements was conducted by comparing the numerical results obtained for different fluid domains, meshes, and elements with experimental results found in the literature. In particular, this work concentrated on modelling the experiments of a cantilever plate vibrating in a fluid performed by Lindholm, Kana, Chu, and Abramson [29] in 1965. Their experiments were performed in a 6′ x 12′ x 8′ deep water tank, with the rectangular plate clamped to a rigid I-beam support structure. In these tests, the cord length b of all plates was 8 inches, and various aspect ratios and thicknesses were examined. (Figure 3.1 shows details of the structure used.)

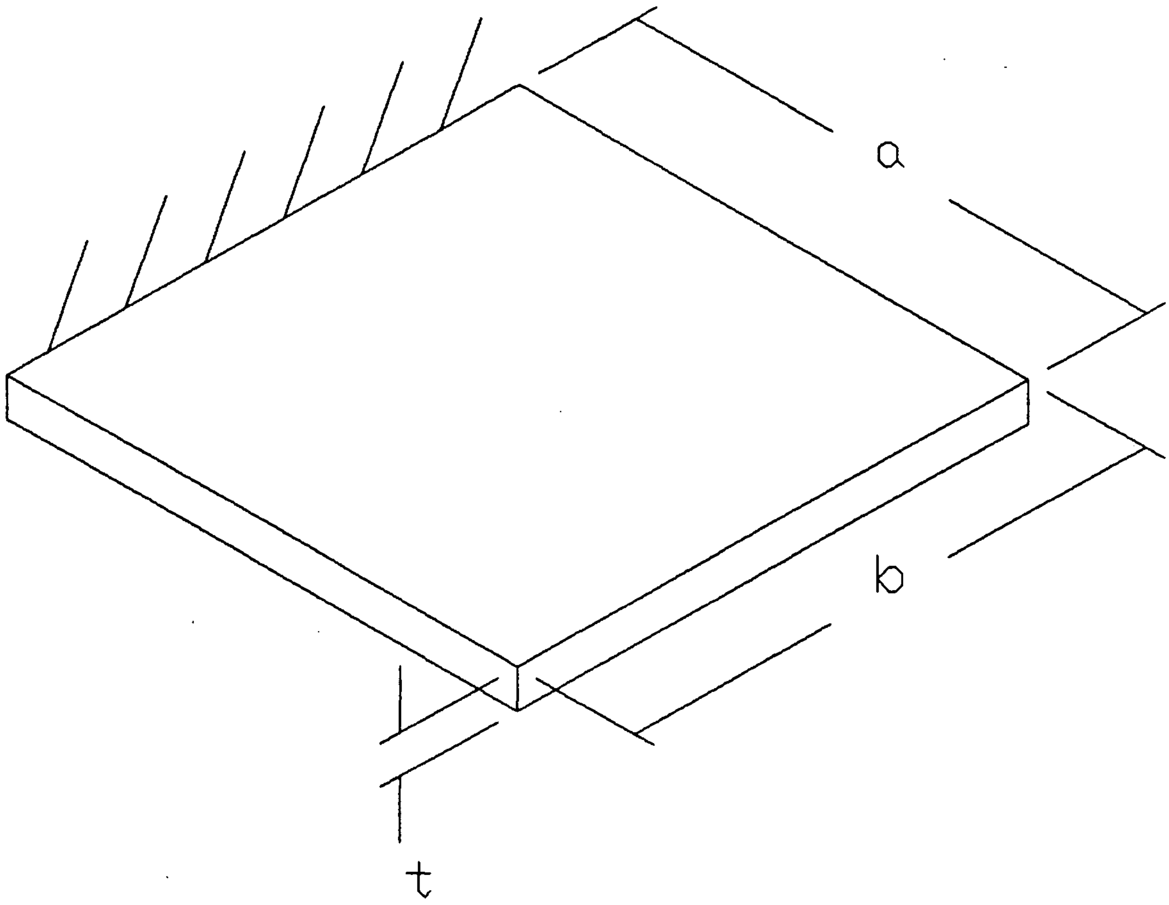

Cord Length b = 8"

Aspect Ratio a/b = 0.5, 1.0, 2.0, and 3.0

Thickness t = 0.105"

Figure 3.1 - Plate Structure

Plates with a thickness of $t = 0.105$ inches and aspect ratio's of $a/b = 0.5$, 1.0, 2.0, and 3.0 were considered in the numerical study detailed here. The cantilever plate was modelled using the Thick/Thin Shell element from the Finite Element Program VAST. This element is an isoparametric element with quadratic shape functions (completely defined in Appendix C). It has 8 nodes in total, 4 corner nodes, and 4 mid-side nodes, with 5 local degrees of freedom per node, 3 translations, and 2 rotations.

In these experiments, the plates were made of 1018 cold-rolled steel, and the fluid used was water. The material properties of steel for the numerical work were taken as : Young's modulus $E = 3.0 \times 10^7$ psi, Poisson's ratio $\nu = 0.3$, and mass density $\rho_s = 7.324 \times 10^{-4}$ lb.sec^2/in^4. The mass density of water was taken as $\rho_w = 9.38 \times 10^{-5}$ lb.sec^2/in^4.

3.1 Vibration in Air

Before attempting to model the plate's vibration in fluid, vibration characteristics in air were examined in order to reduce the error involved in the fluid analysis introduced by the discretization of the plate.

To compare the numerical and experimental results for the plate vibrating in air, three different finite element meshes were considered for each of the four aspect ratios (as shown in Figure 3.2). The first mesh used four Thick/Thin Shell elements to model the plate. The second mesh used sixteen elements, while the third mesh used thirty-two. (The results of these tests are summarized in Table 3.1 - 3.4, and the modes of vibration are shown in Figure 3.3).

The fourth mode was a bending mode in the cord direction (as shown in Figure 3.3). As the aspect ratio of the plate was increased, this mode disappeared, and the 2-node cantilever mode comes into play, which has been denoted as mode 6. Thus, for an aspect ratio of $a/b = 0.5$ or 1.0, there were no results for mode 6, while for an aspect ratio of $a/b = 2.0$ or 3.0, there were no results for mode 4.

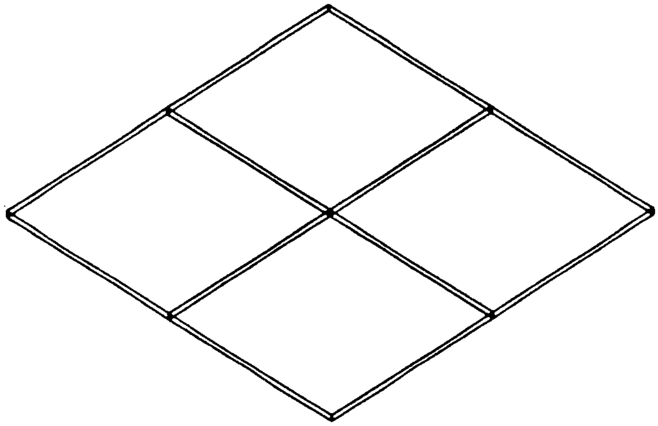

a) 4 Element Mesh

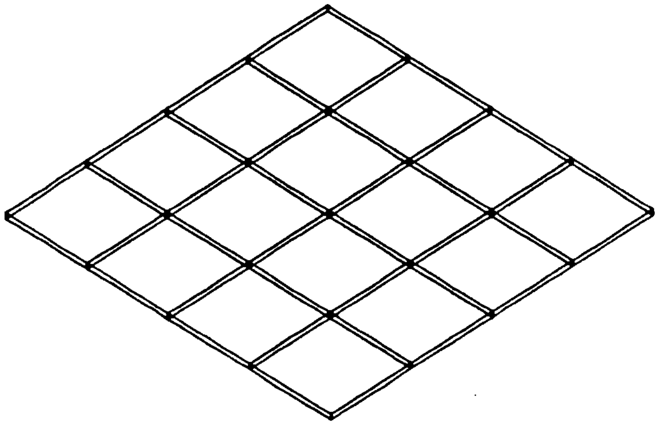

b) 16 Element Mesh

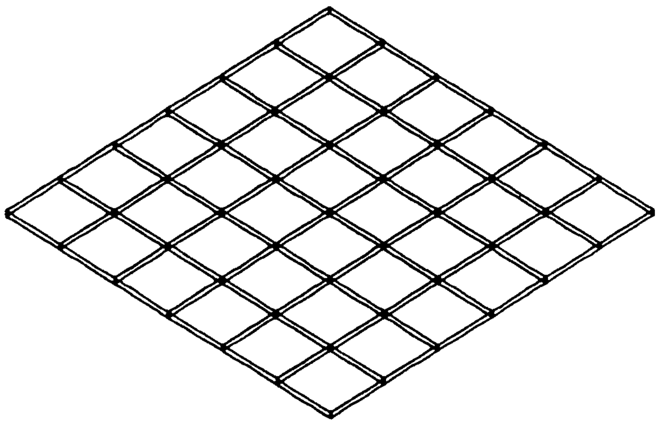

c) 32 Element Mesh

Figure 3.2 - Finite Element Plate Meshes

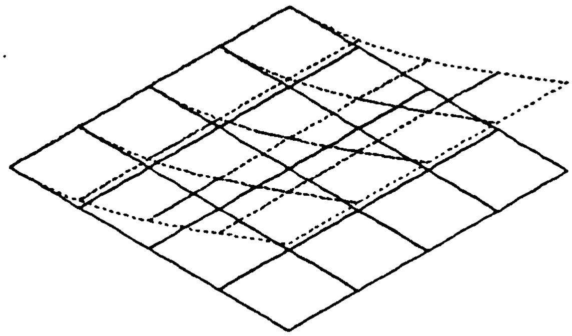

a) Mode 1 - 1^{st} Cantilever

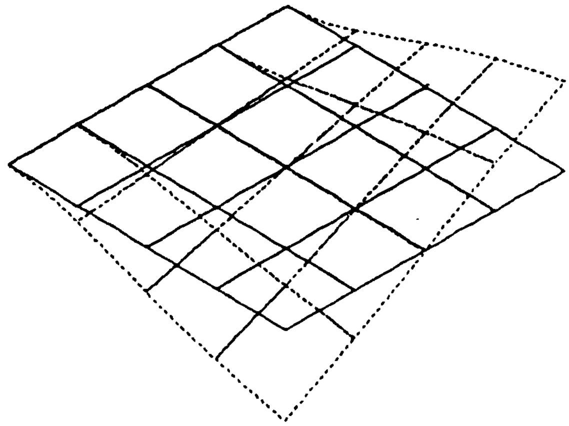

b) Mode 2 - 1^{st} Torsion

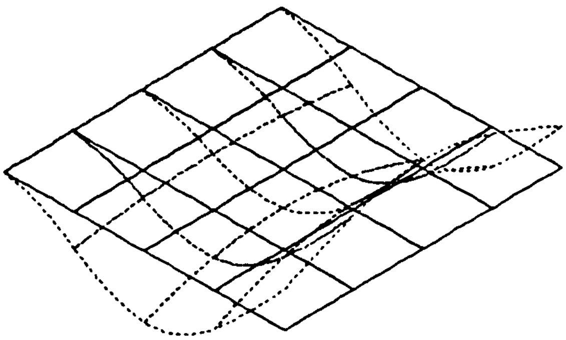

c) Mode 3 - 2^{nd} Cantilever

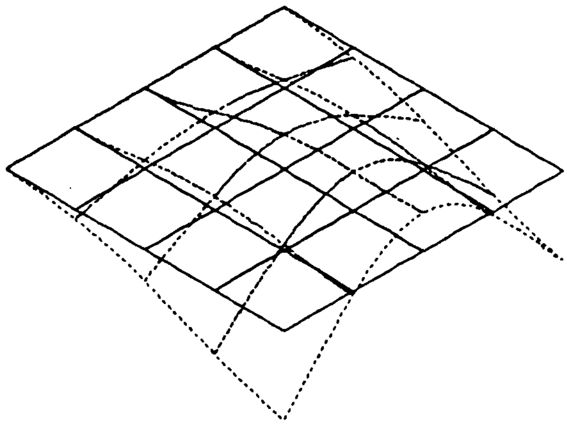

d) Mode 4 - Bending b direction

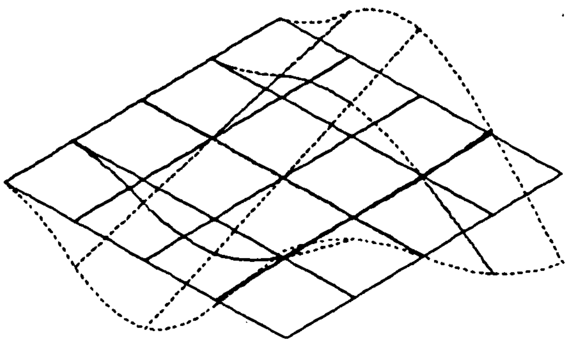

d) Mode 5 - 2^{nd} Cant./1^{st} Tor.

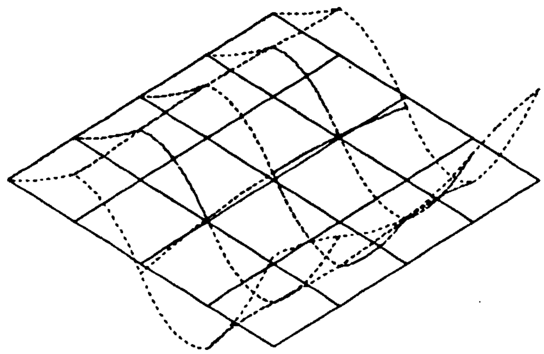

e) Mode 6 - 3^{rd} Cantilever

Figure 3.3 - First Six Mode Shapes of Plate Vibration

Mode #	1	2	3	4	5	6	CPU sec
Plate Theory	223	342	652	1397	1580	-	
Experimental	214	339	649	1339	1518	-	
4-Element Mesh	224	349	727	1490	1664	-	56
16-Element Mesh	224	342	651	1401	1588	-	279
32-Element Mesh	224	341	648	1394	1573	-	1665

Table 3.1 - Plate Theory and Finite Element Results

a/b = 0.5 b = 8.0 inches t = 0.105 inches

Mode #	1	2	3	4	5	6	CPU sec
Plate Theory	55.6	136	341	437	496	-	
Experimental	52.9	129	326	423	476	-	
4-Element Mesh	55.8	137	363	473	531	-	60
16-Element Mesh	55.7	136	342	440	497	-	306
32-Element Mesh	55.6	136	341	435	495	-	1954

Table 3.2 - Plate Theory and Finite Element Results

a/b = 1.0 b = 8.0 inches t = 0.105 inches

Mode #	1	2	3	4	5	6	CPU sec
Plate Theory	13.8	59.3	85.9	-	194	234	
Experimental	12.9	58.2	80.8	-	189	228	
4-Element Mesh	13.9	59.4	91.8	-	204	370	72
16-Element Mesh	13.8	59.2	86.4	-	194	250	449
32-Element Mesh	13.8	59.1	85.9	-	193	242	1369

Table 3.3 - Plate Theory and Finite Element Results

$a/b = 2.0$ $b = 8.0$ inches $t = 0.105$ inches

Mode #	1	2	3	4	5	6	CPU sec
Plate Theory	6.1	38.0	38.1	-	120	104	
Experimental	6.2	40.3	38.7	-	126	109	
4-Element Mesh	6.2	40.7	37.7	-	171	124	97
16-Element Mesh	6.1	37.5	38.1	-	118	108	690
32-Element Mesh	6.1	37.5	38.1	-	118	108	1678

Table 3.4 - Plate Theory and Finite Element Results

$a/b = 3.0$ $b = 8.0$ inches $t = 0.105$ inches

The four element mesh had 105 degrees of freedom, the sixteen element mesh 325 degrees of freedom, and the thirty-two element mesh 665 degrees of freedom. The frequencies predicted by the sixteen element mesh were better than those of the four element mesh; and, in turn, the results of the thirty-two element mesh were better than those of the sixteen element mesh (as displayed in Tables 3.1 - 3.4).

The frequencies predicted for the individual modes of vibration were also affected by the degree of idealization in the finite element model. (Figure 3.3 shows the mode shapes for the first six modes of vibration that the plate experienced.) As the mode number increased so did the complexity of the mode shape, and more degrees of freedom were required to model it. Therefore, in any given finite element mesh, the error in the frequency predicted for a mode increased as the complexity of the modes increased. Thus, in the numerical results as (displayed in Tables 3.1 - 3.4), the four element mesh was able to predict the frequencies of the first and second modes very well, but it was not as accurate with higher modes. The sixteen element mesh was able to model the first five or six modes, and the thirty-two element mesh was able to model further still but showed little improvement in the frequencies predicted for the first five modes.

The frequencies predicted for the individual modes of vibration were also affected by the aspect ratio of the plate. (This effect can be seen in Tables 3.1 - 3.4.) At the lower aspect ratios, a/b = 0.5 and 1.0, the sixteen element mesh predicted the theoretical results exactly, but at aspect ratios of

2.0 or 3.0, some error crept in. As the aspect ratio increased, the length of the element in the span direction a was affected. As a result, the element's ability to model the mode shape of the higher modes was hampered, as the shape functions for this element only modelled quadratic displacements. (See Appendix C.)

The finite element and the theoretical results were very close, but the numerical results were higher in most cases than the experimental results by about five percent. This difference was attributed to two factors : 1) the finite element results did not account for the added mass of the air around the plate, which lowered the frequencies of vibration; and 2) if the cantilever support was not absolutely rigid, this flexibility also could have led to a decrease in the natural frequencies for the experimentally measured values.

The results for the sixteen element mesh were not very different from those of the thirty-two element mesh. However, there was a large difference in the CPU time, with the thirty-two element mesh taking four to six times longer than the sixteen element mesh, depending on which aspect ratio was considered. For this reason, the sixteen element mesh was used for the finite element runs of the cantilever plate vibrating in the fluid.

3.2 Vibration in Fluid

Four plates with different aspect ratios were modelled numerically to determine their vibration characteristics in a fluid. The plate structure was modelled using the sixteen element Thick/Thin Shell mesh, which had been found to be satisfactory in determining the lowest five modes of vibration for the air experiments. The fluid was modelled using the different fluid elements available in VAST. These numerical results were compared with the experimental results of Lindholm et al [29].

The numerical work conducted in this phase of the investigation was directed at determining the effects of various fluid modelling parameters. These were : the extent of the fluid domain that needed to be discretized to give satisfactory results, the number of fluid elements used in the domain, and the type of fluid elements used to model the domain.

Other factors that affected the comparison between the experimental and the numerical results were : the compressibility of the fluid, the extent of the surface waves generated, and the amount of vortex shedding off the edges of the plate. These effects could not be modelled with the present development of the fluid equations in VAST.

3.2.1. Effect of the Extent of the Fluid Domain

In the experimental set up, the plates were immersed in a 6′ x 12′ x 8′ deep water tank parallel to the free surface. The depth of immersion for the experimental deep water results was not given. However, the experimental results showed that if the plate was submerged a distance greater than one half the span length, the resulting frequencies were independent of the submerged depth.

The extent of the fluid domain was very important to the numerical results obtained for the velocity potential ϕ. If the finite element fluid domain did not extend far enough from the structure, the boundary condition of $\phi = 0$ was an artifical constraint on the system. This affected the determination of the velocity potential ϕ in the interior of the fluid domain, causing the frequency to be higher than it was normally.

The range of fluid domains analysed were $D/b = 0.125$, 0.25, 0.5, 0.75, 1.0, 1.5, and 2.0. (Figure 3.4 shows three views of the three meshes used : a plan, an elevation, and a right-side view.) D refers to the dimension of the fluid domain extending out from the plate in all directions, while b was the cord length of the fixed side of the cantilever plate.

Typical results for the 8-noded fluid element (using three different fluid meshes) vibrating in its first mode of vibration show that as the domain of the fluid was enlarged, the frequencies of vibration converged, provided enough elements were used in the fluid domain; however, the frequencies of vibration did not always converge to the experimental results. (See Figure 3.5). The convergence to results other than the experimental results will be explained below (in Section 3.2.3.1).

This convergence clearly displayed the adverse effect on the frequencies of having the fluid domain boundaries too close to the structure. In some cases, the results began to diverge as the domain was increased, as is illustrated by meshes that only used one element in the fluid domain. This divergence was due in part to the limited ability of the shape functions to model the changes in the velocity potential ϕ over one element.

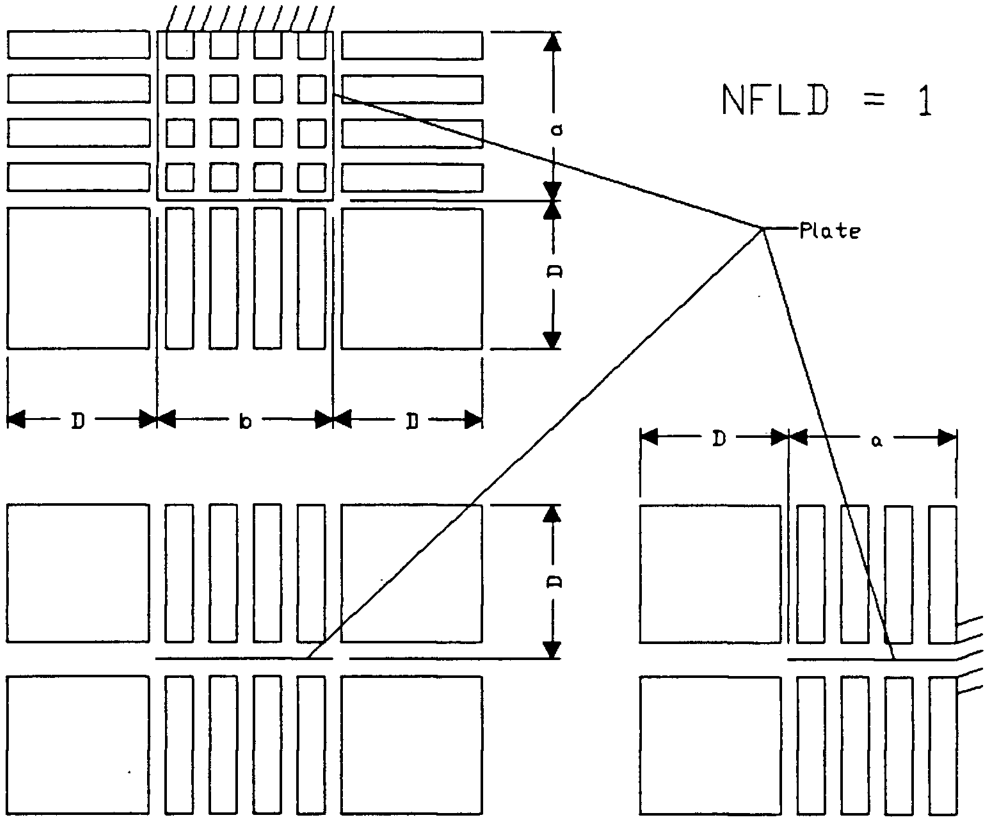

Figure 3.4a - Finite Element Fluid Domain Meshes

NFLD = 1 Mesh

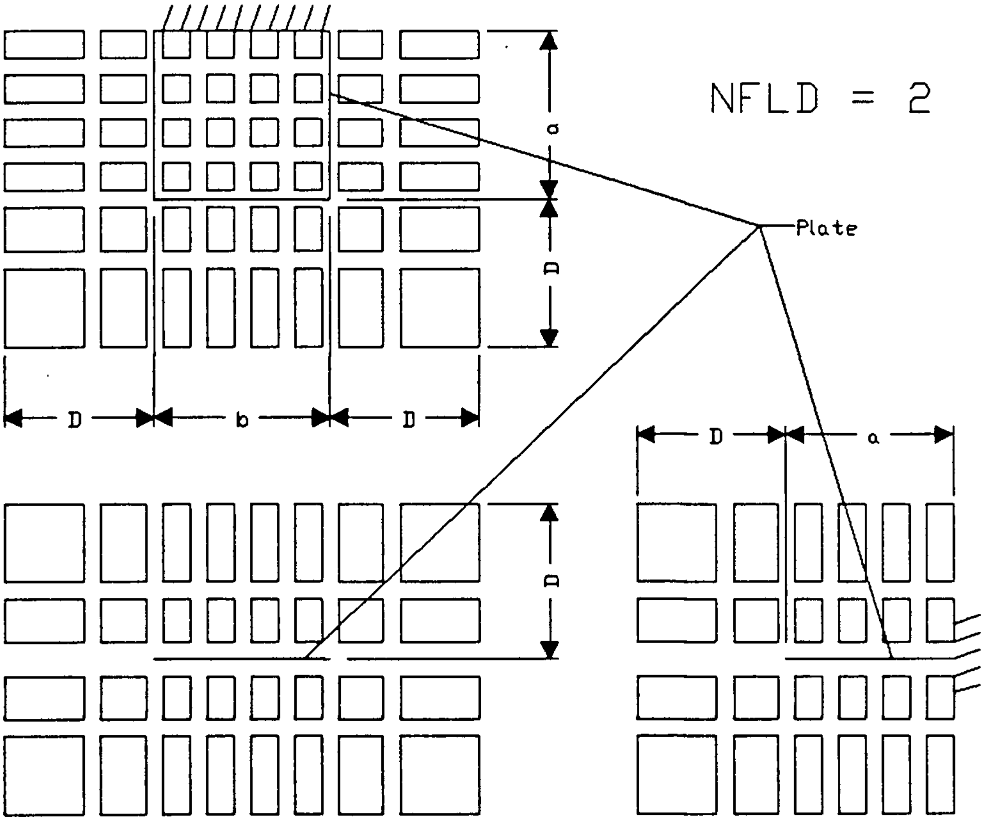

Figure 3.4b - Finite Element Fluid Domain Meshes

NFLD = 2 Mesh

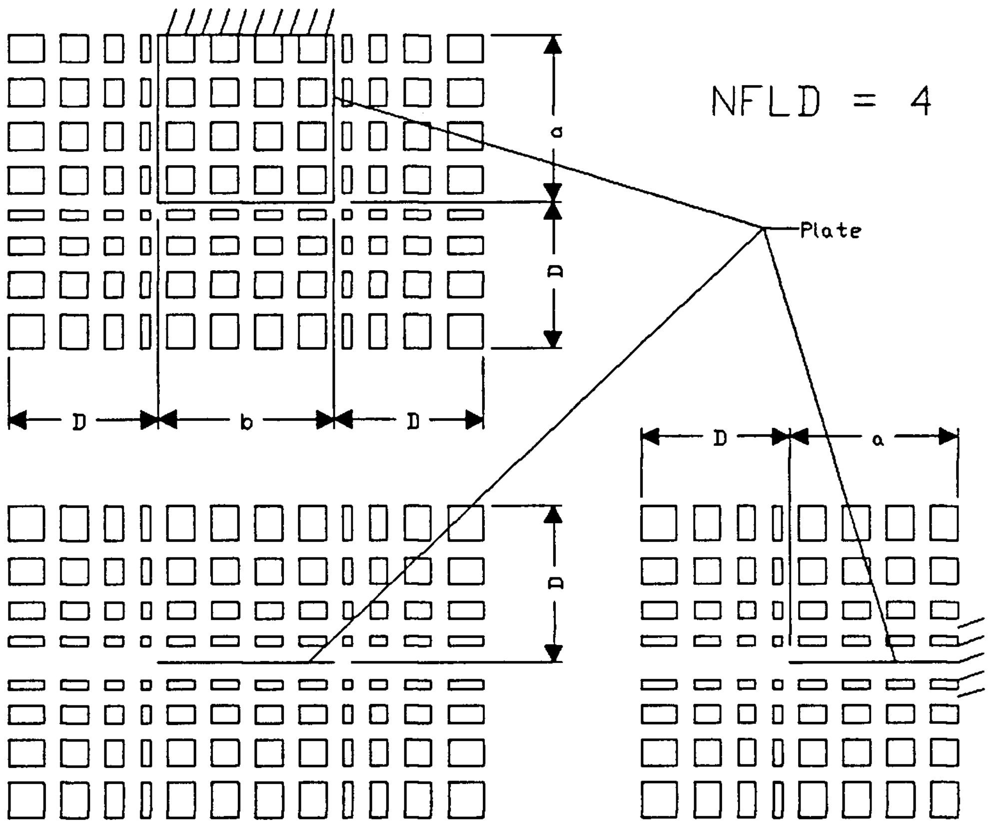

Figure 3.4c - Finite Element Fluid Domain Meshes

NFLD = 4 Mesh

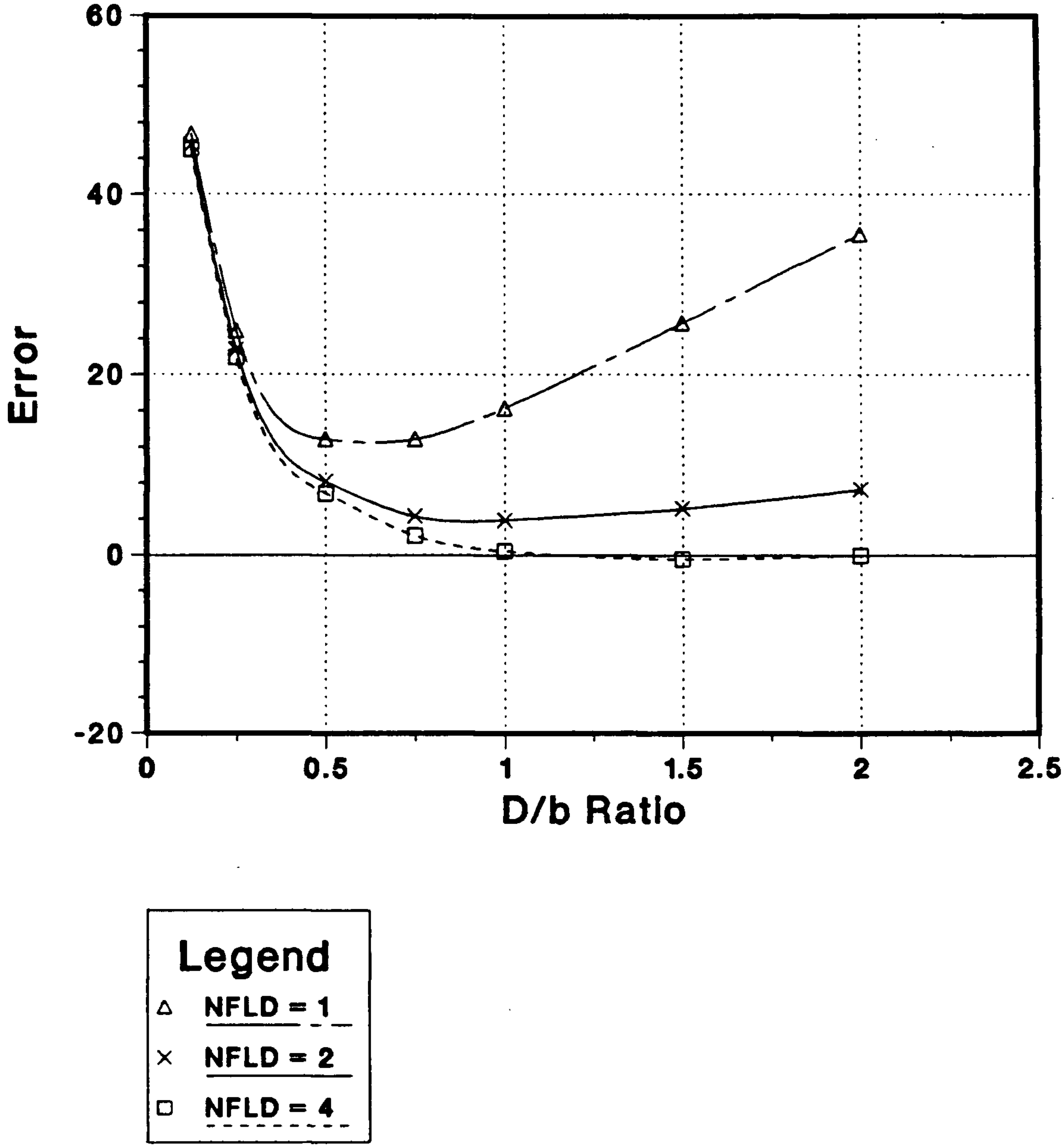

Figure 3.5 - Error Between Finite Element and Experimental Results Using the 8-Noded Fluid Element for Mode 1 with Plate Aspect Ratio a/b = 1.0

3.2.2. Effect of the Number of Elements in the Fluid Domain

The number of fluid elements in the domain also affected the numerical results. As the number of elements in the fluid domain was increased, the idealization error was reduced and the numerical results began to approach the exact solution of Laplace's equation. This phenomenon was similar to the structural discretization discussed above (in Section 3.1).

Within each of the seven different fluid domains considered, three fluid meshes were examined. These meshes were denoted by NFLD = 1, NFLD = 2, and NFLD = 4, where NFLD was the number of fluid elements across the dimension D. (Figure 3.4 presents these meshes.) The fluid mesh NFLD = 1 had 60 elements, while NFLD = 2 had 96 elements, and NFLD = 4 had 192 elements. It should be noted that over the plate, the fluid mesh and the plate mesh corresponded. The elements in the fluid domain were not spaced evenly but were closer together near the edges of the plate, as this was where the velocity potential ϕ was changing most rapidly.

The results of the second mode of vibration of the plate (with an aspect ratio a/b = 1.0) using the three different fluid meshes with both 8 and 20-noded fluid elements were examined. (See Figure 3.6). Within a fluid mesh, the CPU times for each D/b ratio were very similar (thus, only the averaged values are presented in Table 3.5).

	Type of Fluid Element	
Fluid Mesh	8-Noded	20-Noded
NFLD = 1	590	622
NFLD = 2	614	1391
NFLD = 4	861	9952

Table 3.5 - Average CPU Time (sec) Various Fluid Meshes for Plate Aspect Ratio a/b = 1.0 b = 8.0 inches t = 0.105 inches

From these results, it became apparent that the NFLD = 4 mesh predicted frequencies that were closest to the experimental results. But the results of the two element fluid mesh NFLD = 2 were also quite good and took less CPU time, especially for the 20-noded fluid element meshes.

At a specific D/b ratio, the frequencies predicted by the NFLD = 1 mesh were higher than the results of the NFLD = 2 mesh, which in turn were higher than the NFLD = 4 mesh (as seen in Figure 3.6). The NFLD = 1 mesh was underestimating the added mass

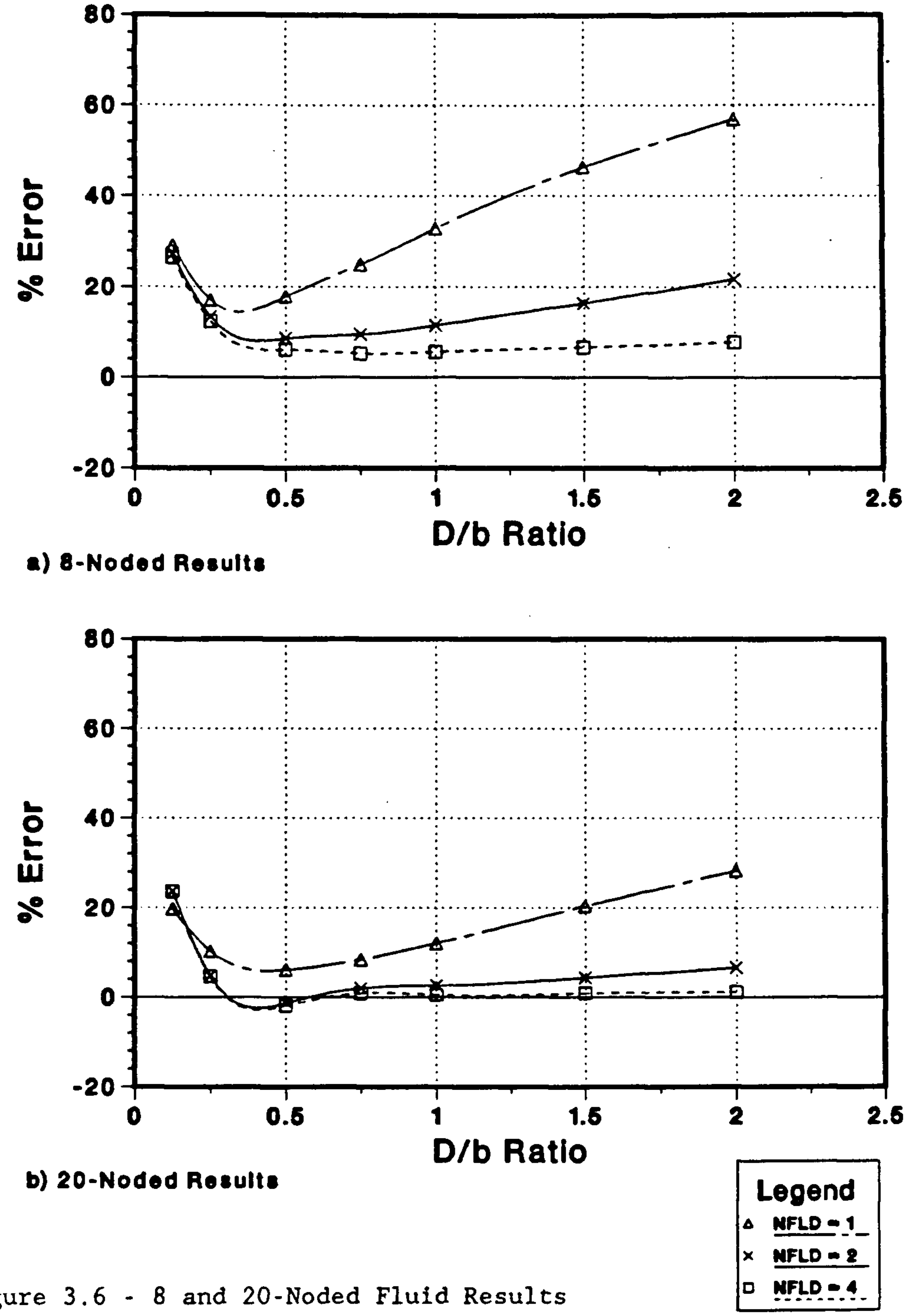

Figure 3.6 - 8 and 20-Noded Fluid Results for Mode 2 with Plate Aspect Ratio a/b = 1.0

matrix the most, while the NFLD = 4 mesh came closest to predicting the experimental results.

It should be noted that the results of the NFLD = 2 mesh for the 8-noded fluid element and the NFLD = 1 mesh of the 20-noded element took about the same CPU time (see Table 3.5), but the 20-noded results were slightly better (as shown in Figure 3.7). This fact is interesting since both meshes had almost the same number of degrees of freedom; the 8-noded mesh had 105 degrees of freedom, while the 20-noded mesh had 109. At higher values of D/b the results of the 8-noded mesh became better than the 20-noded mesh (see Figure 3.7), due to the high aspect ratio that the one 20-noded element was experiencing in this mesh. As well, the results of the NFLD = 4 mesh for the 8-noded element and the NFLD = 2 mesh for the 20-noded element (as displayed in Figure 3.8) took about the same CPU time; but, the results of the 8-noded mesh were worse, even though it had more degrees of freedom. The 8-noded mesh had 539 degrees of freedom, while the 20-noded mesh had 488 degrees of freedom. The accuracy here stemmed from the fact that the 20-noded fluid elements had better shape functions than those of the 8-noded elements. The shape functions for the fluid elements are discussed below (and given in detail in Appendix B).

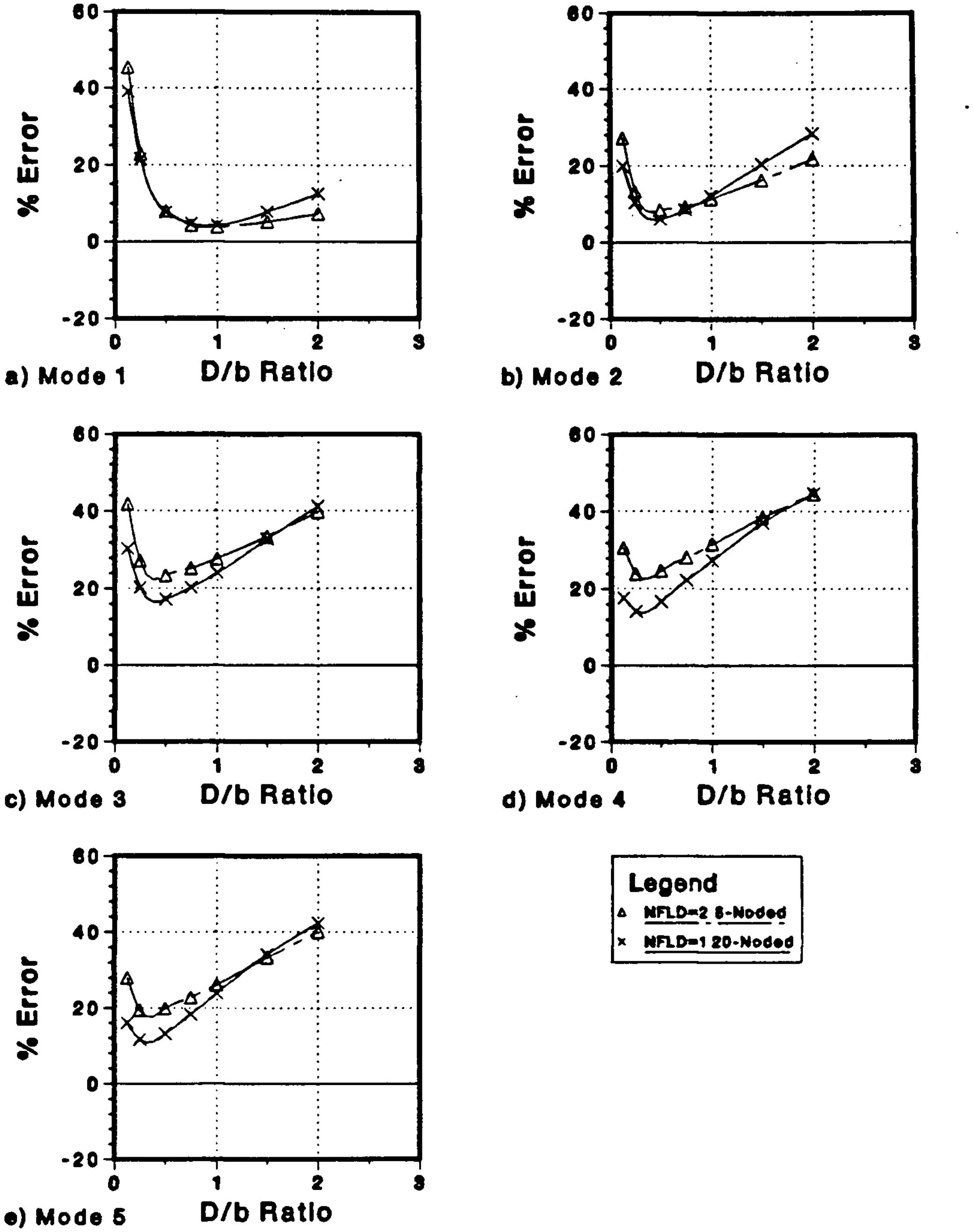

Figure 3.7 - Comparison of Two Fluid Meshes

with Plate Aspect Ratio a/b = 1.0

NFLD = 2 with 8-Node Fluid Element

NFLD = 1 with 20-Noded Fluid Element

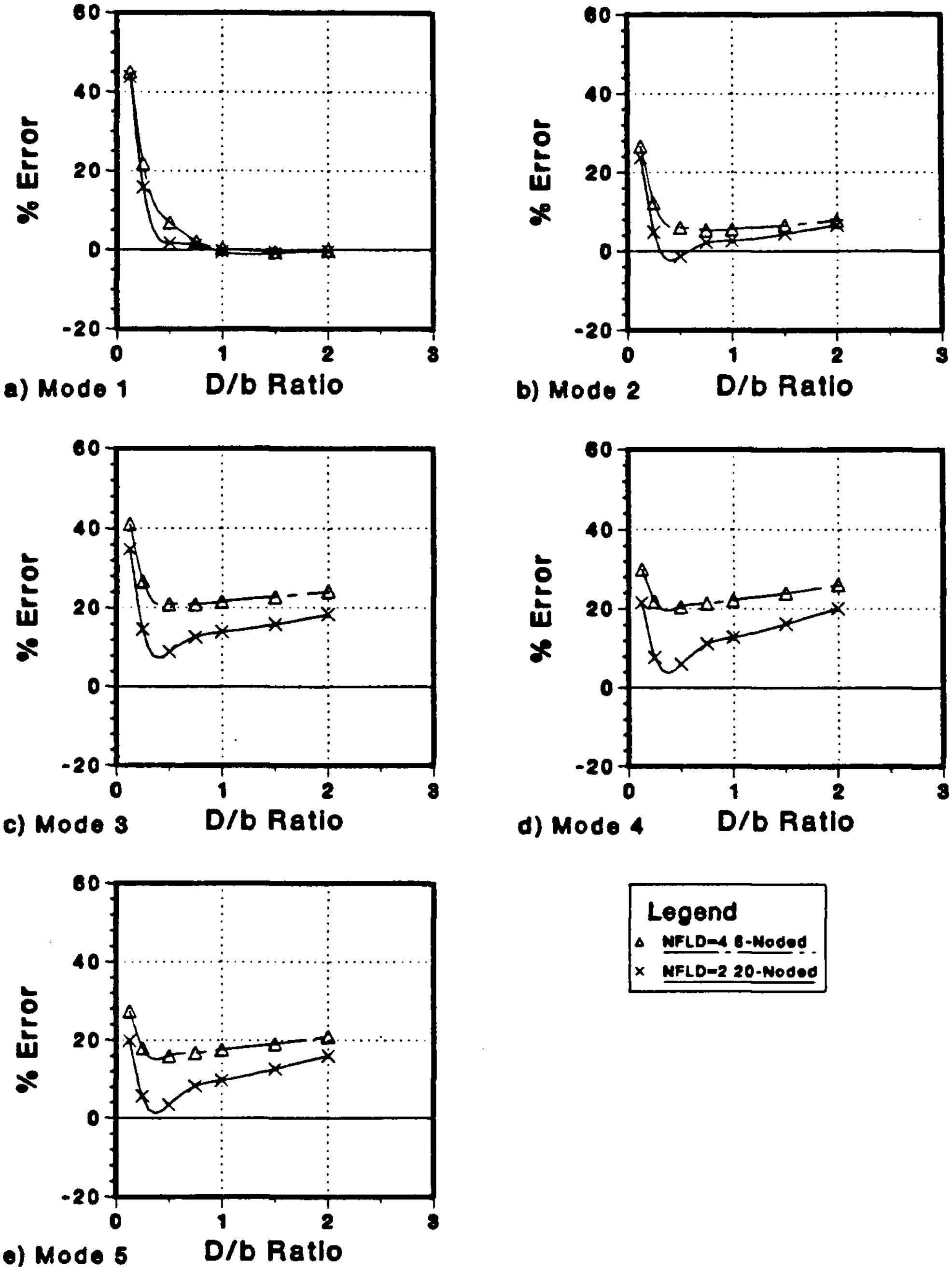

Figure 3.8 - Comparison of Two Fluid Meshes

with Plate Aspect Ratio $a/b = 1.0$

NFLD = 4 with 8-Noded Fluid Element

NFLD = 2 with 20-Noded Fluid Element

3.2.3. Effect of Different Fluid Elements

Three types of fluid elements were used to construct the various fluid meshes : an 8-noded linear element mesh, a 20-noded quadratic isoparametric element mesh, and a mesh containing a combination of the 8-noded element and one row of the 8-noded infinite element. The 8-noded infinite element had the same shape functions as the normal 8-noded fluid element in two of its directions; however, the third direction was the infinite direction, in which the velocity potential had either an exponential decay or an $(1/r)^n$ decay. (For details of these elements see Appendix B.) The meshes that contained the infinite element were different from the others, as the infinite element could be only on the fluid domain boundary. When the infinite element was used, it replaced either the last row, the last two rows, or the last three rows of the conventional fluid elements, depending on which mesh was used.

3.2.3.1. 8 and 20-Noded Fluid Elements

The results of the 8-noded fluid element and the 20-noded fluid element for the first five modes of vibration with an aspect ratio $a/b = 1.0$ were examined (and are presented in

Figures 3.6 and 3.9 - 3.12). In general, the 20-noded results predicted frequencies that were closer to the experimental results than the 8-noded results. This fact was expected since the 20-noded fluid element had quadratic shape functions and could represent a quadratic change in its velocity potential in any local element direction, while the 8-noded element only had linear shape functions and could only represent a linear change.

The results for the first mode of vibration with the four different plate aspect ratios using the 8 and 20-noded fluid elements were examined. (See Figures 3.13 and 3.14.) It was seen that as the aspect ratio increased, the finite element results began to deteriorate. This deterioration was explained by the assumptions that were made in the formulation of the velocity potential ϕ. The flow was assumed to be inviscid, irrotational, and incompressible; however, the real flow had these effects. The deterioration of the results was due to vortex shedding off the side of the plate, and it was the viscous effects in the fluid that caused the vortices. As the aspect ratio of the plate increased, the vortices that were shed from the sides of the plate began to dominate the flow in the area around the edges of the plate. Since the finite element formulation was unable to deal with the complex flow that was produced by the vortices, the results were poor.

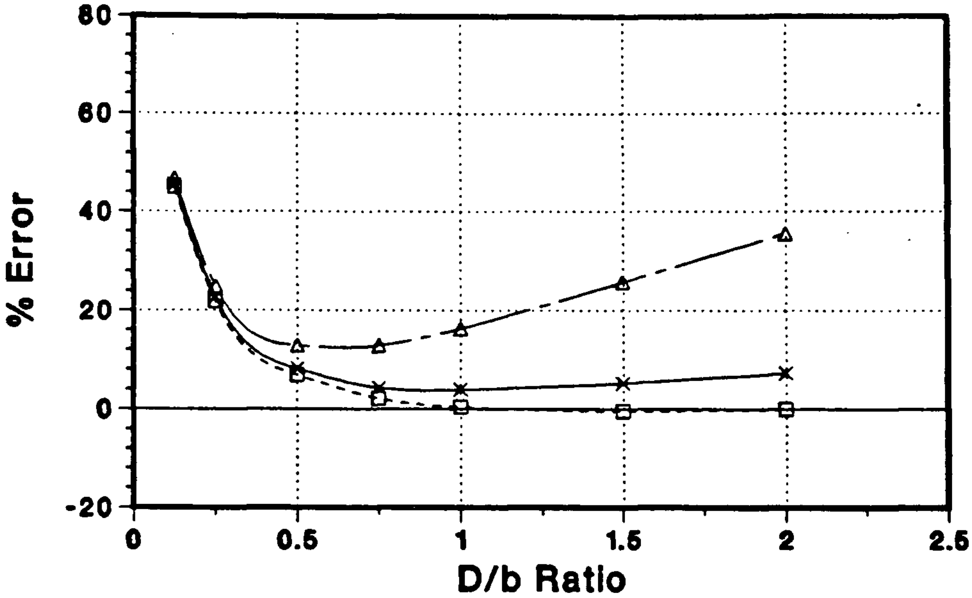

a) 8-Noded Results

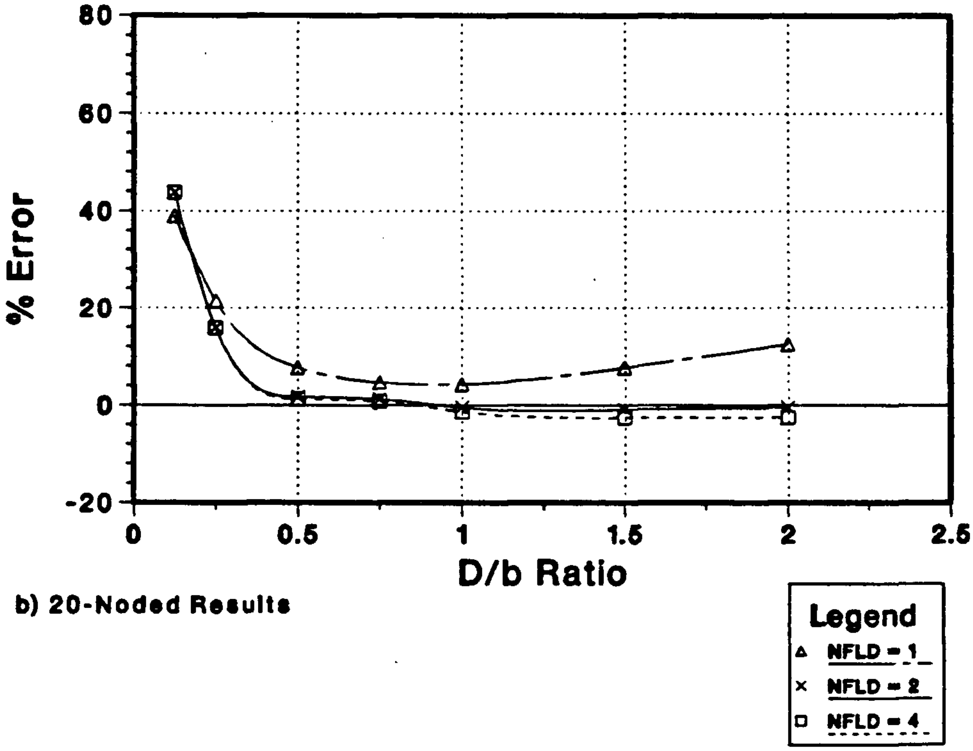

b) 20-Noded Results

Figure 3.9 - 8 and 20-Noded Fluid Results for Mode 1 with Plate Aspect Ratio a/b = 1.0

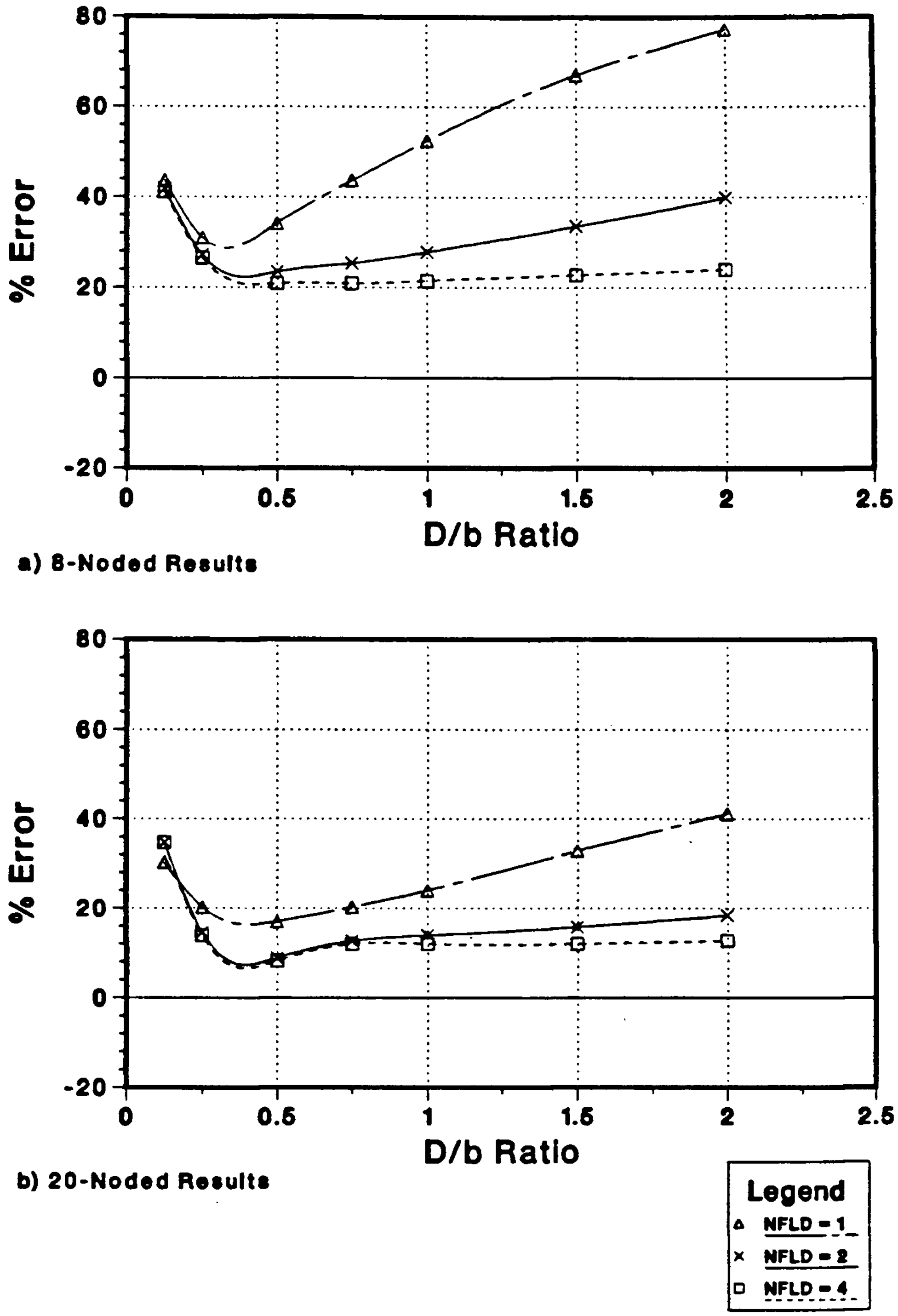

Figure 3.10 - 8 and 20-Noded Fluid Results
for Mode 3 with Plate
Aspect Ratio a/b = 1.0

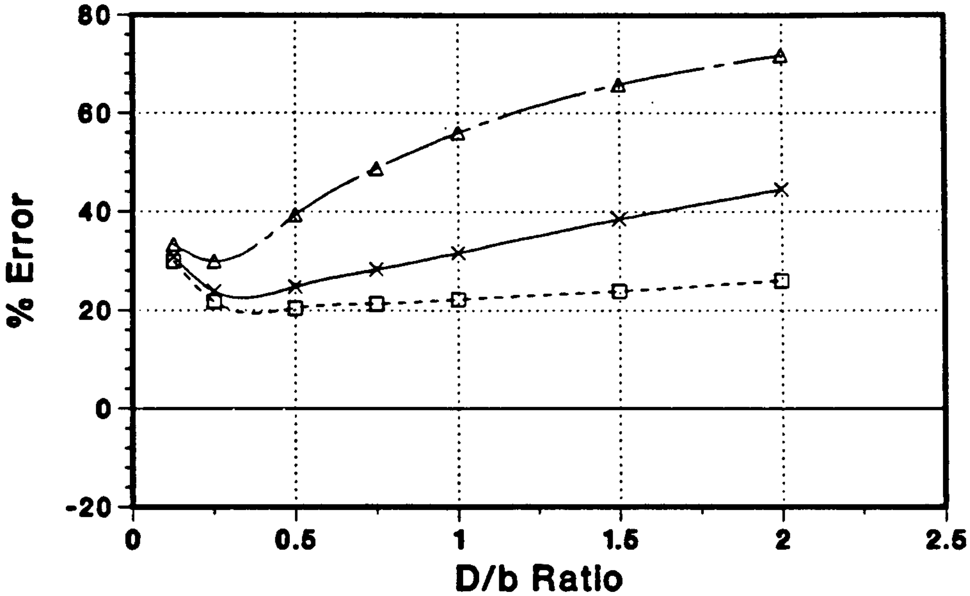

a) 8-Noded Results

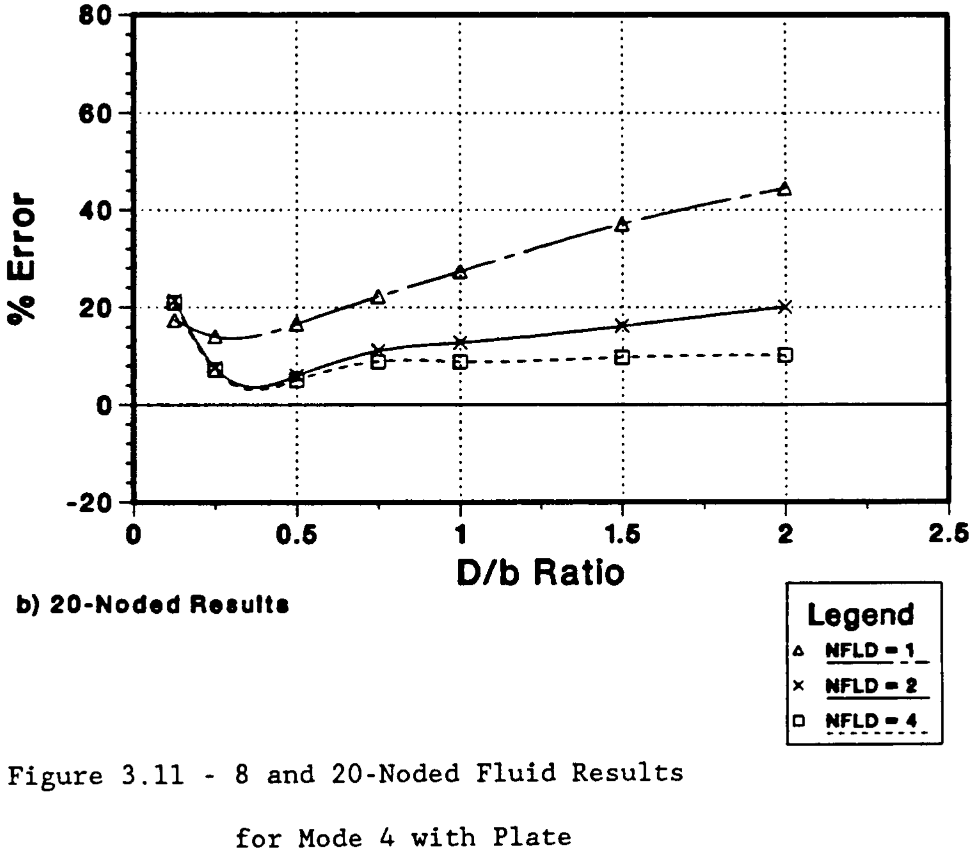

b) 20-Noded Results

Figure 3.11 - 8 and 20-Noded Fluid Results

for Mode 4 with Plate

Aspect Ratio a/b = 1.0

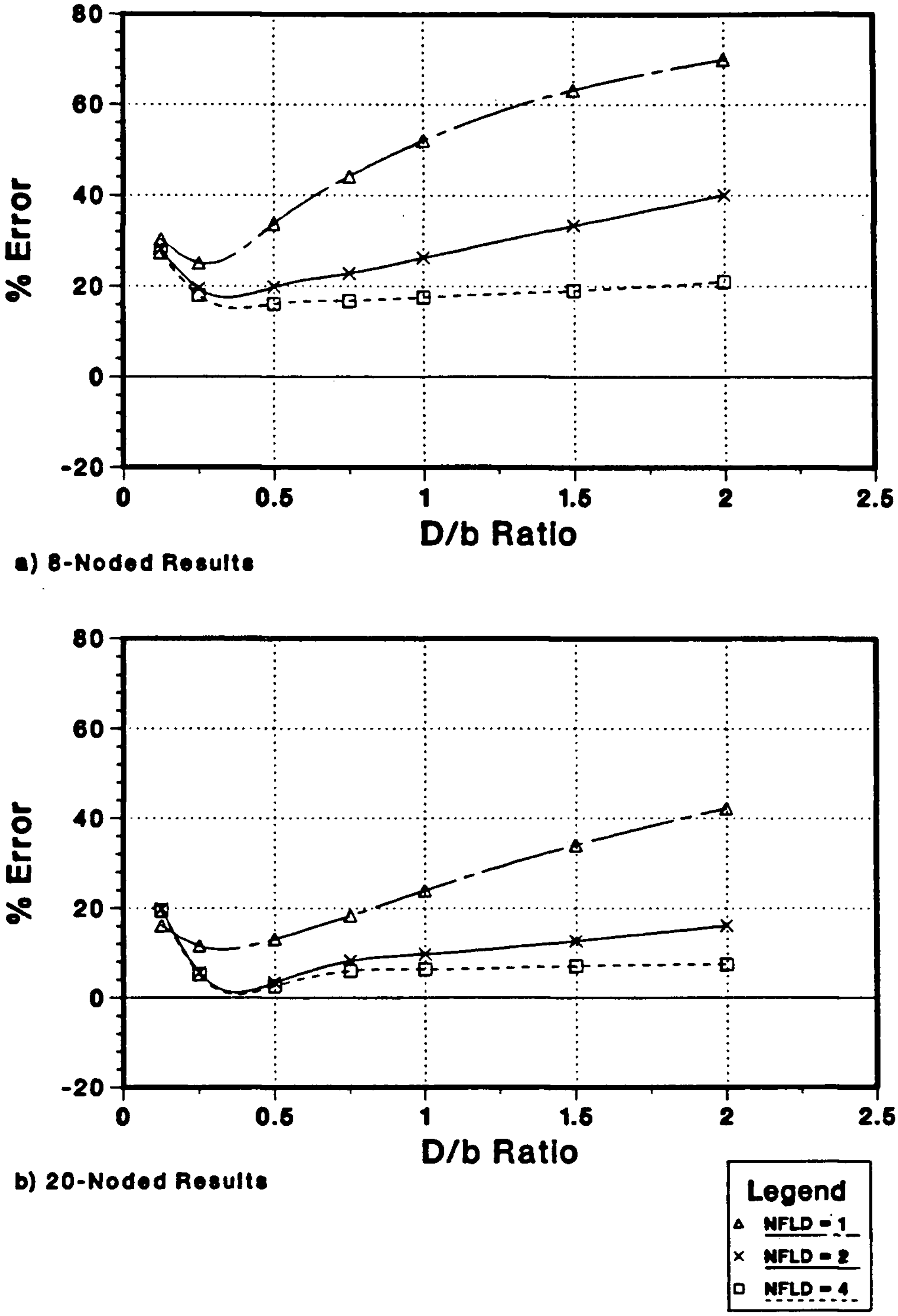

Figure 3.12 - 8 and 20-Noded Fluid Results for Mode 5 with Plate Aspect Ratio a/b = 1.0

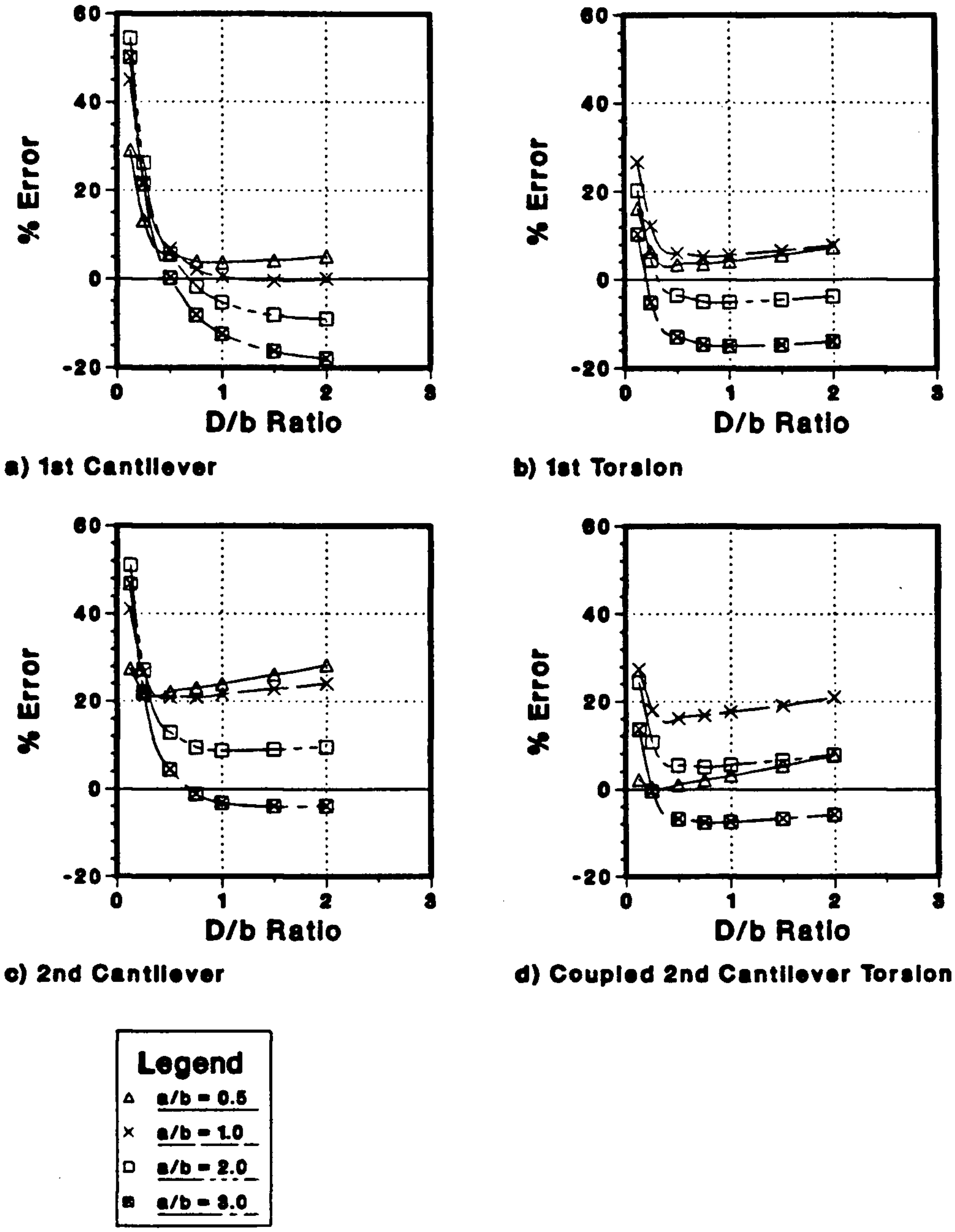

Figure 3.13 - 8-Noded Fluid Results for Various

Plate Aspect Ratios with NFLD = 4

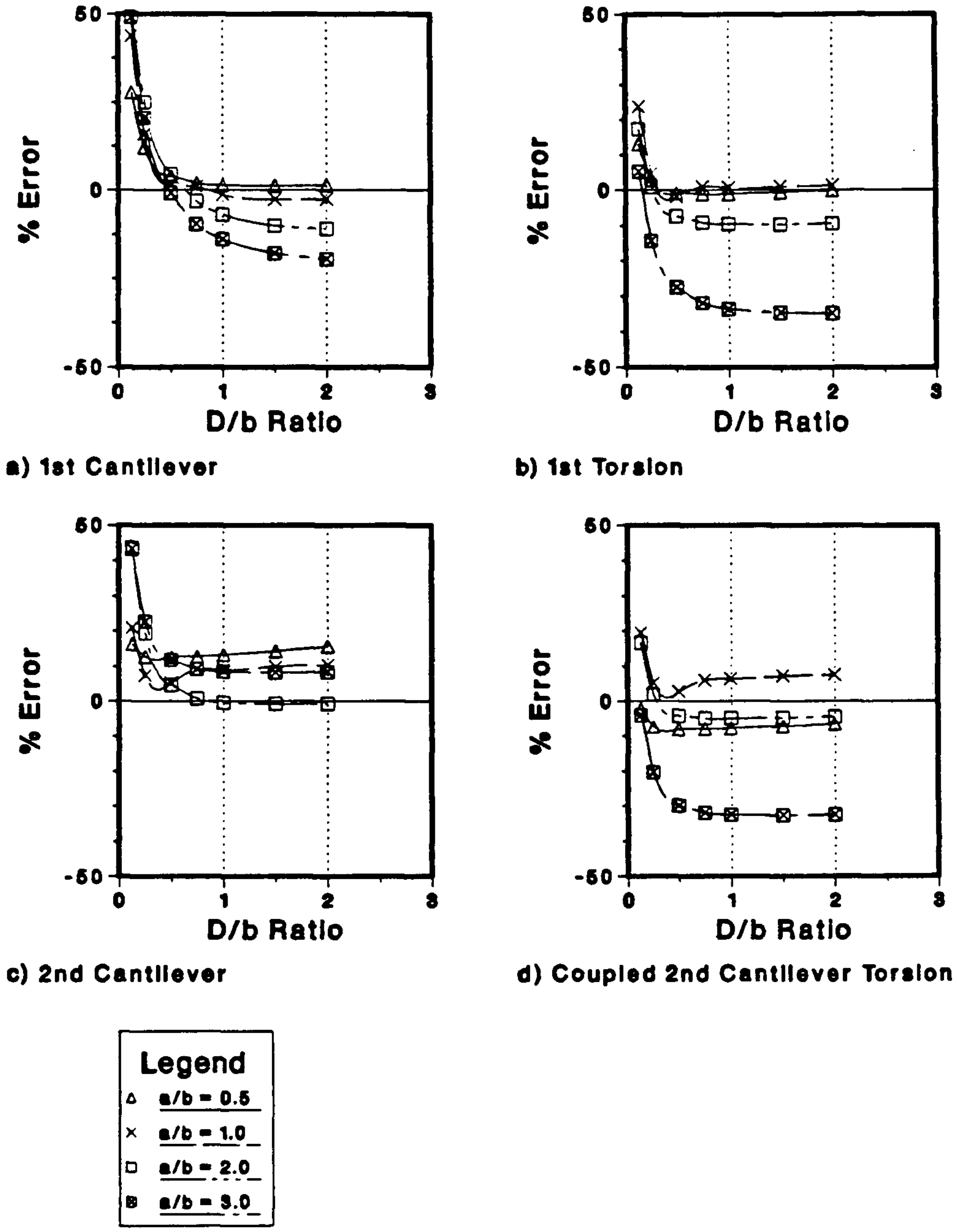

Figure 3.14 - 20-Noded Fluid Results for Various

Aspect Ratios with NFLD = 4

To explain this problem, it was informative to examine the energy in this system. The total energy in the fluid E_T was constant and was produced by the vibration of the structure. If the flow could be considered to be made up of two types of flow--a local flow given by the vortices and a global flow--then, the energy in the flow could be expressed as

$$E_T = E_V^R + E_G^R \tag{3.1}$$

where E_T was the total energy in the flow, E_V^R was the energy in the real vortex flow, and E_G^R was the energy in the real global flow.

Since the total energy in the flow E_T was constant, the presence of vortices consumed some of the energy in the flow, causing the energy in the global fluid flow to decrease. The fluid elements were unable to model the effect of the vortices; they were able to model only the global flow in the fluid. Therefore, the finite elements estimated only the energy in the global flow given by

$$E_T^{FE} = E_G^{FE} \tag{3.2}$$

since the source of energy for the fluid flow came from the structural vibrations in mode i. The energy in that mode was given by

$$E_T = (\omega_i^2 \{\Psi_i\}^T[M_S]\{\Psi_i\} + \{\Psi_i\}^T[K]\{\Psi_i\}) \tag{3.3}$$

which was approximately the same for the real system and the finite element model of the structure. Therefore

$$E_T^{FE} = E_T^R \tag{3.4}$$

which led to

$$E_G^{FE} = E_V^R + E_G^R \tag{3.5}$$

$$E_G^{FE} > E_G^R \tag{3.6}$$

Since the finite element fluid elements were unable to model the vortex shedding, the energy in the global flow was overestimated. This in turn caused the added mass matrix $[M_A]$ to be overestimated; thus, a lower frequency was predicted than that determined experimentally.

When vortex shedding was occurring, the 8-noded fluid element meshes appeared to give better predictions for the frequency of vibration than the 20-noded fluid meshes, although both were below the experimental results. (This effect is displayed in Figure 3.15.) By examining the results of the other tests (given in Figures 3.6 and 3.9 - 3.12), it was concluded that the 8-noded fluid meshes always predicted frequencies that were larger than those predicted by the 20-noded meshes. This finding indicated that for any given fluid mesh NFLD = 1, 2, or 4, the kinetic energy predicted by the 8-noded fluid mesh was lower than that predicted by the 20-noded fluid mesh, or in equation form

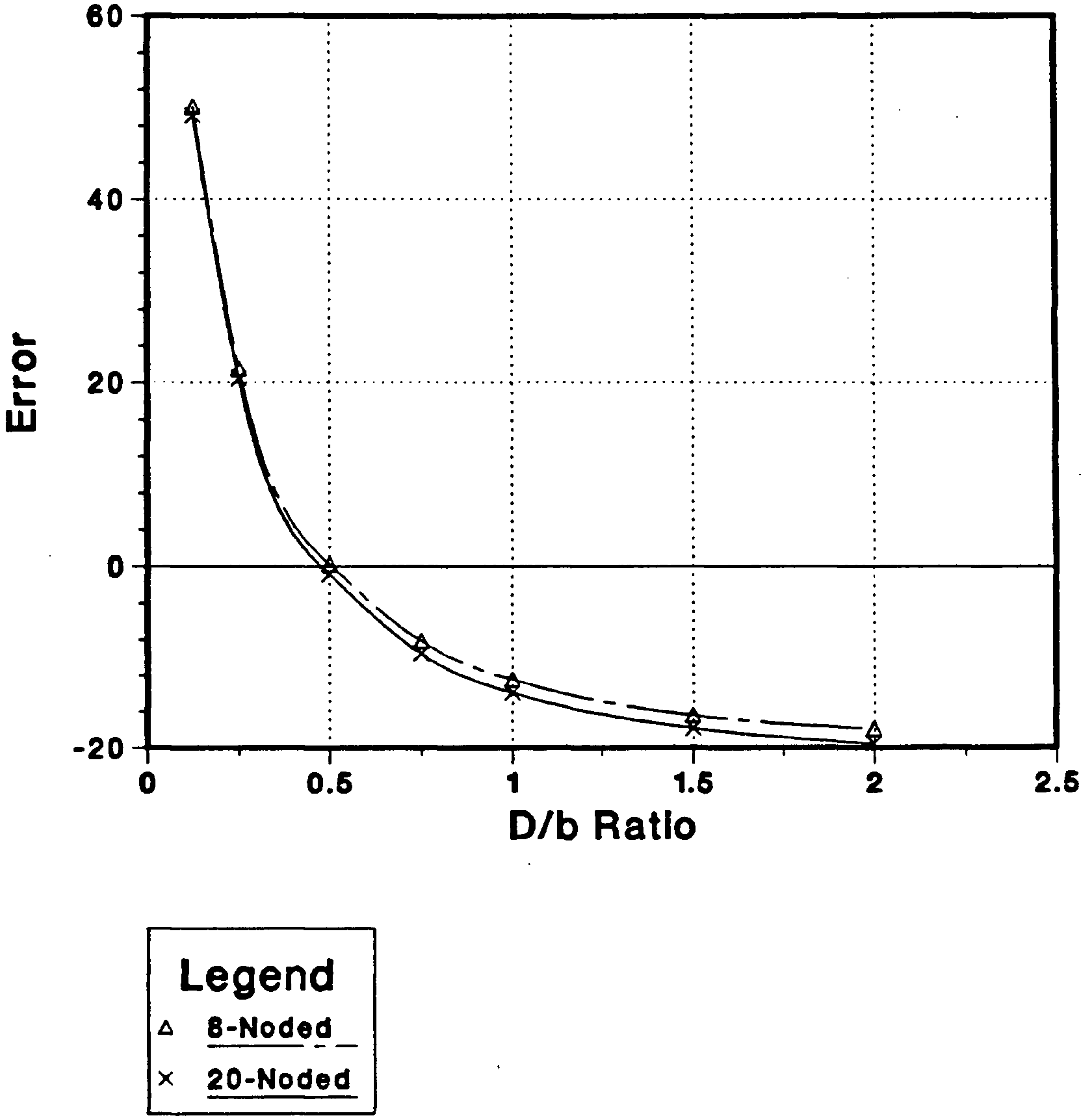

Figure 3.15 - Comparison of 8 and 20-Noded Fluid Results Using NFLD = 4 and Plate Aspect Ratio a/b = 3.0 for Mode 1

$$\omega_{i_8}^2 \{\Psi_i\}^T [M_A]_8 \{\Psi_i\} < \omega_{i_{20}}^2 \{\Psi_i\}^T [M_A]_{20} \{\Psi_i\} \quad .$$

However, the kinetic energy predicted by the 8-noded fluid meshes was less than that predicted by the 20-noded fluid meshes, causing ω_8 to be higher than ω_{20}, which explained the "better" results for the 8-noded fluid element meshes when vortex shedding was occurring.

3.2.3.2. Infinite Element

The infinite element results were obtained for plates with an aspect ratio of only a/b = 1.0, and they considered only the normal 8-noded fluid elements when other fluid elements were needed to model the fluid. The three meshes used for the 8 and 20-noded fluid elements denoted by NFLD =1, NFLD = 2, and NFLD = 4 were examined.

In the NFLD = 1 mesh, all the elements were replaced by the infinite elements. This mesh was denoted as NFLD = 1 INF = 1. In the NFLD = 2 mesh, only the last row of the 8-noded fluid elements was replaced with the infinite elements. This mesh was denoted as NFLD = 2 INF = 1. In the NFLD = 4 mesh, three different combinations of the infinite elements were used. The first mesh replaced only the last row of the 8-noded fluid elements with the infinite elements, and it was denoted as NFLD = 4 INF = 1. The second mesh replaced the last two rows of the 8-noded fluid elements with one row of infinite elements, and it was denoted as NFLD = 4 INF = 2. The third mesh replaced the last three rows of the 8-noded fluid elements with one row of infinite elements, and it was denoted as NFLD = 4 INF = 3. (These five meshes are shown in Figure 3.16.) NFLD referred to the number of normal fluid elements that were used in these meshes. INF referred to the number of rows in the NFLD mesh replaced by the infinite element. For all these meshes, the infinite direction was taken normal to the plate.

The infinite element did an excellent job of modelling the boundary condition of $\phi = 0$, even for small fluid domains, without affecting the determination of the velocity potential ϕ in the interior domain. (See Figure 3.17.) The infinite element results had lower errors than the 8-noded element results for very small fluid domains, such as D/b = 0.125 (as illustrated in Table 3.6).

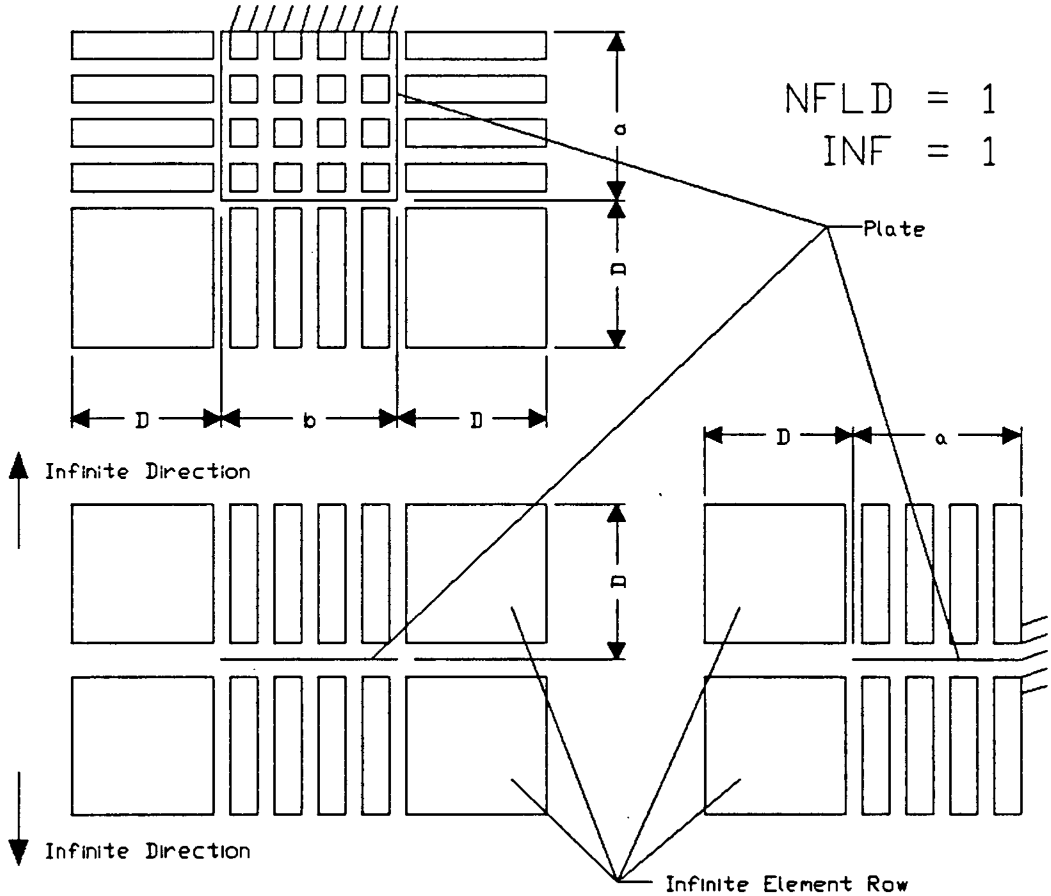

Figure 3.16a - Infinite Element Fluid Domain Meshes

NFLD = 1 INF = 1 Mesh

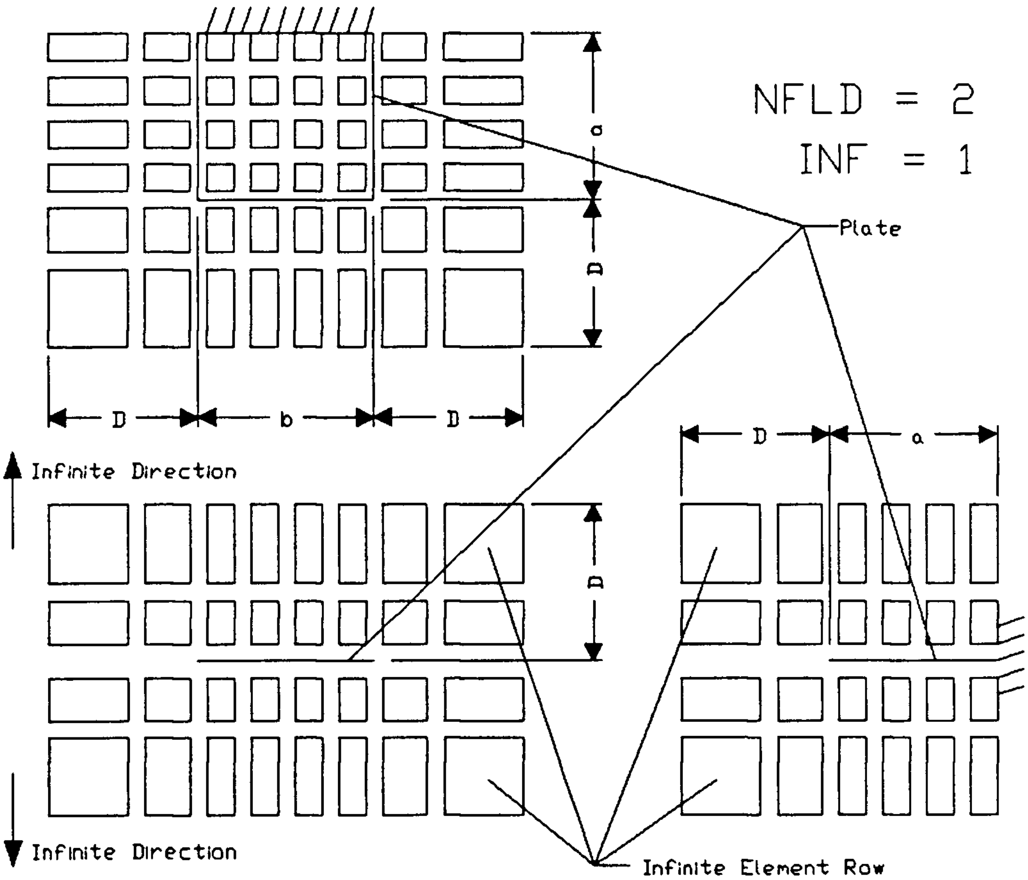

Figure 3.16b - Infinite Element Fluid Domain Meshes

NFLD = 2 INF = 1 Mesh

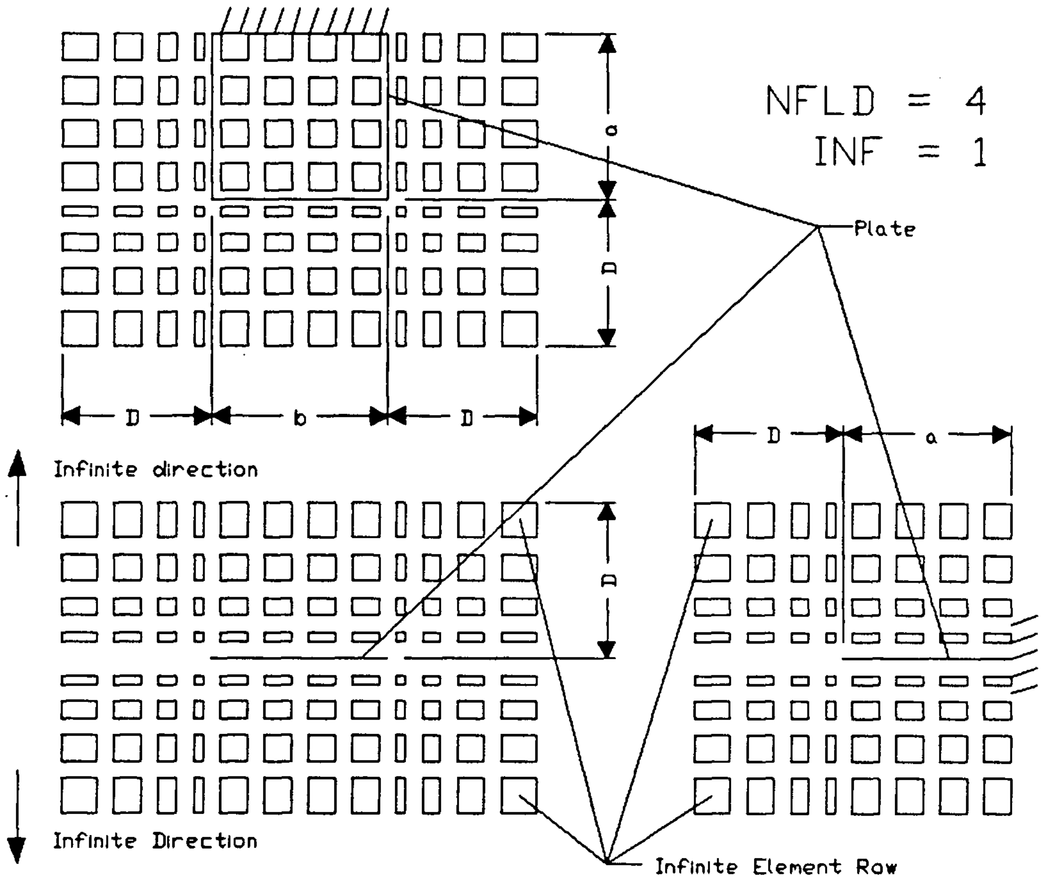

Figure 3.16c - Infinite Element Fluid Domain Meshes

NFLD = 4 INF = 1 Mesh

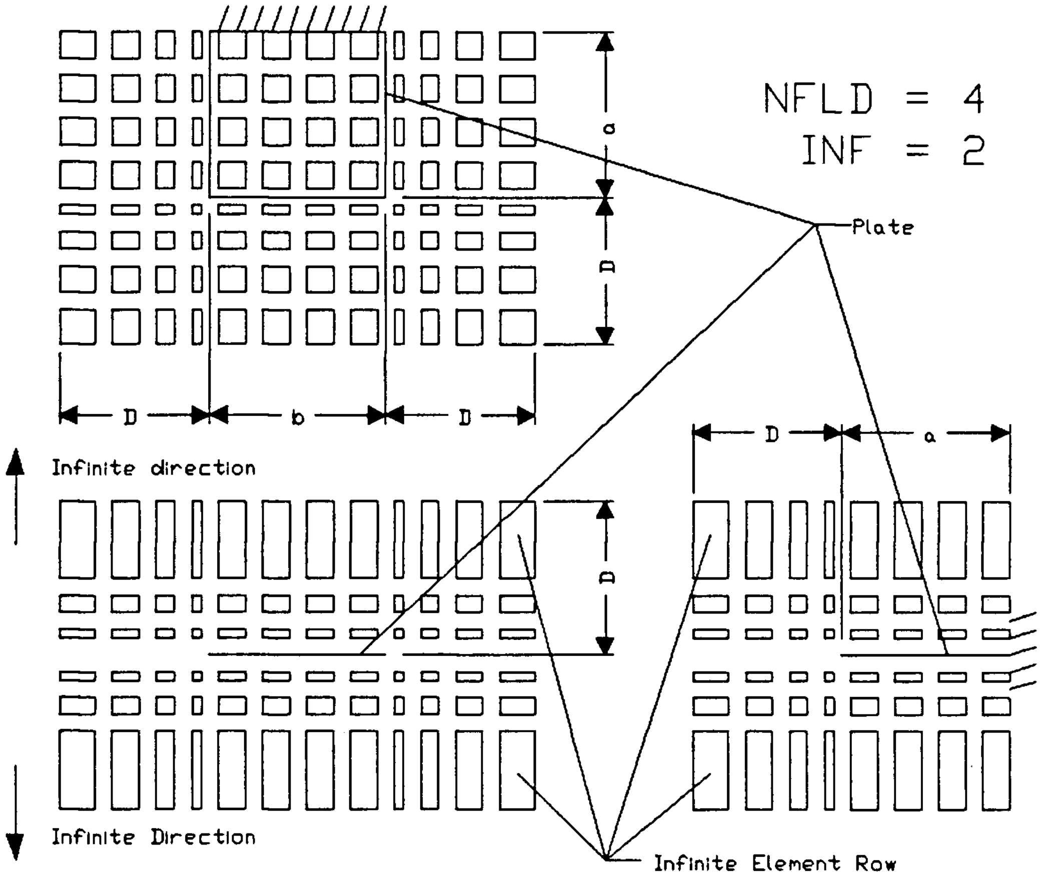

Figure 3.16d - Infinite Element Fluid Domain Meshes

NFLD = 4 INF = 2 Mesh

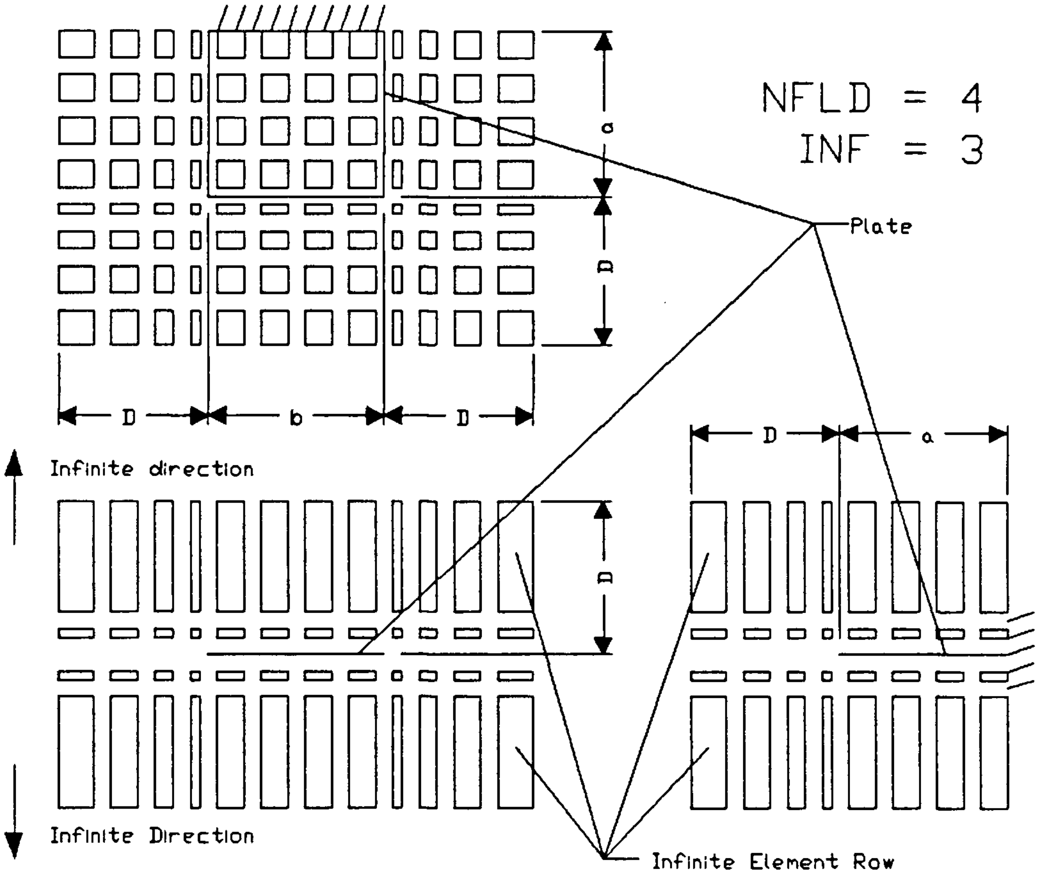

Figure 3.16e - Infinite Element Fluid Domain Meshes

NFLD = 4 INF = 3 Mesh

	Mode #				
Fluid Mesh	1	2	3	4	5
NFLD=1	46.8	29.1	43.7	33.3	30.3
NFLD=2	45.5	27.2	41.8	30.8	28.1
NFLD=4	45.1	26.6	41.1	29.9	27.3
NFLD=1 INF=1	27.1	36.9	48.8	52.7	46.2
NFLD=2 INF=1	12.1	16.5	27.2	28.8	23.9
NFLD=4 INF=1	6.5	8.3	18.9	20.4	15.6
NFLD=4 INF=2	13.0	17.6	28.3	29.6	24.9
NFLD=4 INF=3	21.4	28.6	39.9	42.1	36.7

Table 3.6 - Comparison of Error Between 8-Noded and Infinite Elements for Fluid Domain D/b = 0.125

The mesh combinations of NFLD = 4 INF = 1 and NFLD = 4 INF = 2 gave the best results. These results were comparable to those obtained with the 8-noded fluid element mesh NFLD = 4. (Figure 3.18 displays the results of these three meshes for the first five modes of vibration.) It should also be noted that the CPU times of both of the infinite element meshes were lower than that of the NFLD = 4 mesh (as displayed in Table 3.7).

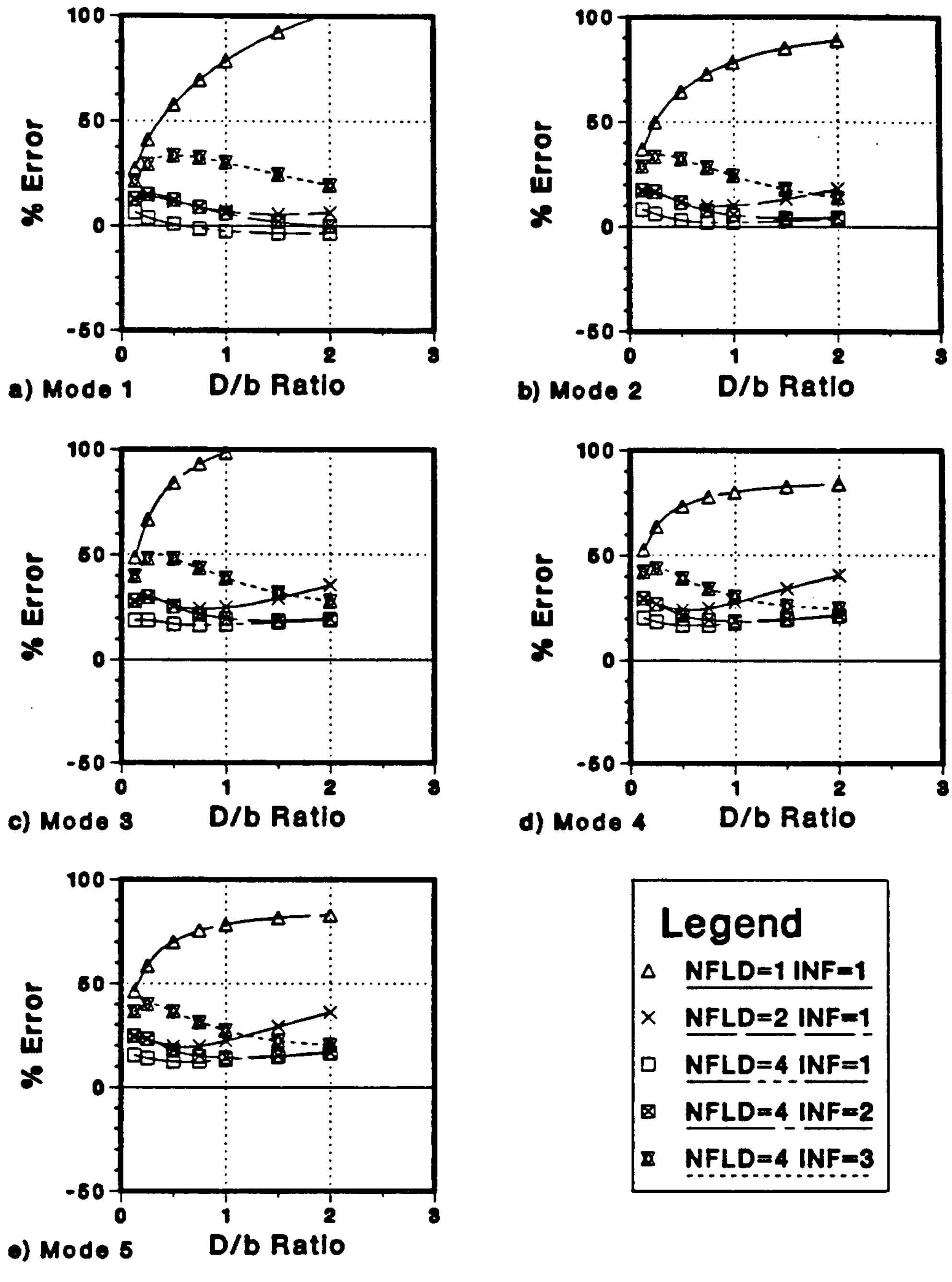

Figure 3.17 - Results for the Infinite Fluid Meshes for Plate Aspect Ratio a/b = 1.0

NFLD = 4	NFLD = 4 INF = 1	NFLD = 4 INF = 2
349 sec	284 sec	201 sec

Table 3.7 - Average CPU Times for Fluid Formulation

Upon examining the results (presented in Figure 3.18) for these three meshes, it was seen that the errors for the 8-noded meshes were larger than the errors in the two infinite element meshes displayed at the higher D/b ratios. In fact, the infinite element results were lower by a constant amount for the last two or three D/b ratios, indicating that the infinite element was still modelling the boundary condition of $\phi = 0$ (on the velocity potential) better than the 8-noded element. There was another effect displayed here too; for all but mode 1, the results of the last three D/b ratios have increasing error. This was due to the increase in the aspect ratio of the fluid elements as the D/b ratio increased. For these meshes, the length in one direction was becoming too long, and the shape functions were experiencing trouble modelling the changes in the velocity potential ϕ.

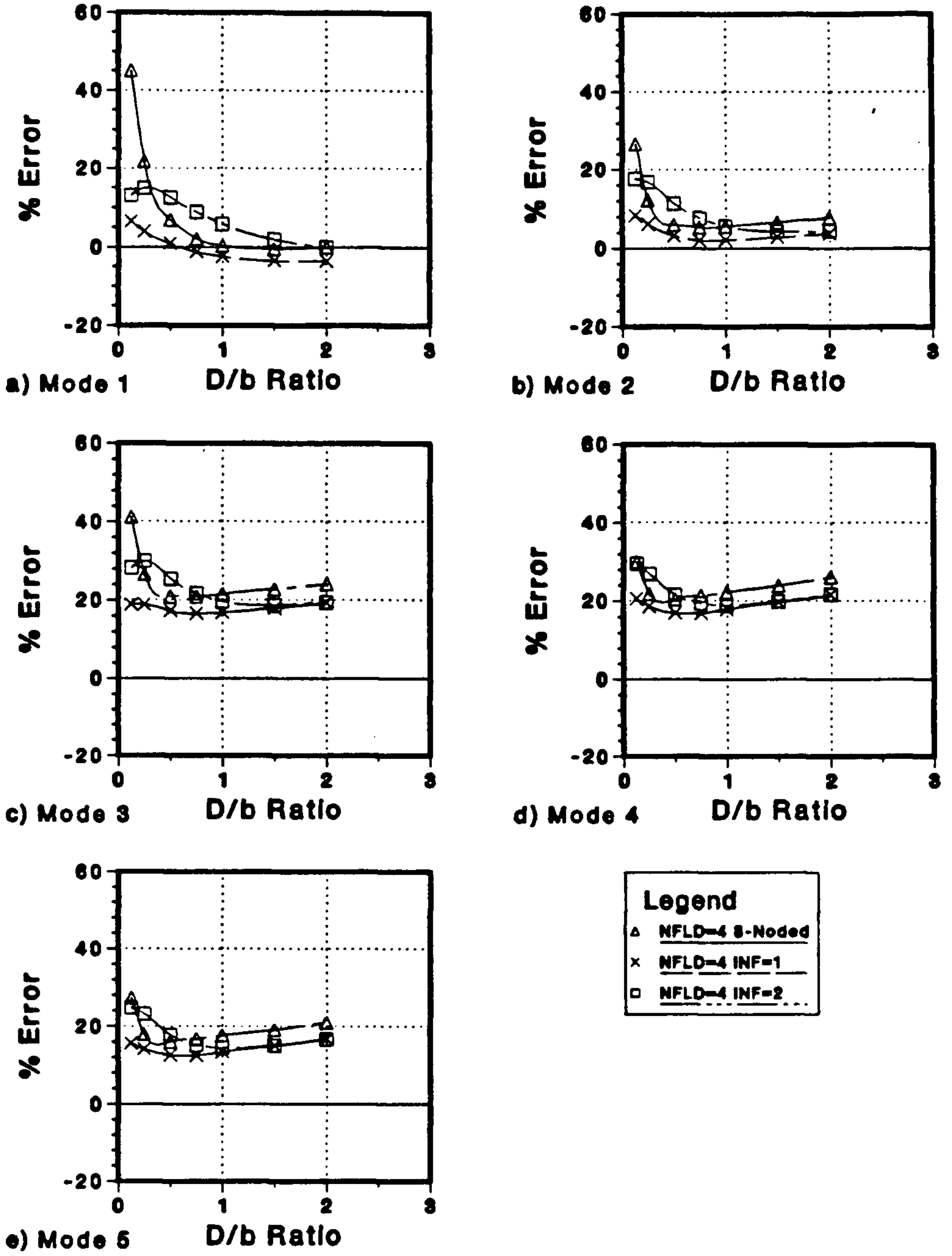

Figure 3.18 - Comparison of the Three Different Fluid Meshes
NFLD = 4 with 8-Noded Fluid Element
NFLD = 4 INF = 1 Infinite Element
NFLD = 4 INF = 2 Infinite Element

3.3 Imposition of an Artificial Bandwidth

In the normal finite element formulation, the structural mass matrix $[M_S]$ and structural stiffness matrix $[K]$ were symmetric and banded, which greatly improved the numerical efficiency. While the added mass matrix $[M_A]$ given by

$$[M_A] = \rho[F]^T[H^*]^{-1}[F] \qquad (2.62)$$

was a symmetric matrix; unfortunately, it was also fully populated. The added mass matrix coupled all the nodes together in contact with the fluid and had 3*NIN columns and 3*NIN rows, where NIN was the number of nodes in the structure that were in contact with the fluid. When the added mass matrix was combined with the structural mass matrix, the banding was lost. The extent that the bandwidth of this new mass matrix

$$[M] = [M_S] + [M_A]$$

was increased over that of the structural mass matrix depended on the number of interface nodes and their location in the structure. The increase in the bandwidth adversely affected the solution time and memory requirements of the eigenvalue problem.

(The finite element representation that VAST uses to determine the added mass matrix $[M_A]$ is not the only method. Others include the Boundary Element Method and the Source

Distribution Method. However, both of these suffer the same fate, as they produce an added mass matrix $[M_A]$ which is very similar to that produced by VAST's current representation of the fluid. The only improvement may be the CPU time taken to calculate the added mass matrix.)

To try to reduce the CPU time and the memory requirements, an artificial bandwidth was imposed on the added mass matrix $[M_A]$. It was felt that the mass coupling between nodes i and j would not be too strong at the fluid-structure interface, especially when the nodes were very far apart (i.e. at a large bandwidth). If this was the case, the imposition of an artificial bandwidth on the added mass matrix $[M_A]$ would not affect the results too much. The implementation required some modifications to the source code of the subroutine MASSM in VAST. This procedure was tested on the plate problem with an aspect ratio $a/b = 1.0$. A bandwidth of 20 corresponded to the full added mass matrix $[M_A]$ being used, while a bandwidth of 1 corresponded to just the diagonal terms of the added mass matrix $[M_A]$. No attempt was made to conserve kinetic energy; terms outside of the imposed bandwidth were truncated.

The results are plotted (in Figures 3.19 and 3.20) as percentage error (between results with the imposed bandwidth and results when the full added mass matrix was used) versus percentage of bandwidth. The suspicion that the mass coupling was not that strong at large bandwidths was confirmed by the results (shown in Figures 3.19 and 3.20). The imposition of a 70 percent bandwidth only increased the error at most by 7 percent. It should be noted that imposing a bandwidth of 40 percent produced a local minimum, giving errors of only 10 percent for all but modes 2 and 3. With a bandwidth of one, the frequencies predicted were all above those when the full added mass matrix was used. This result indicated that the added mass matrix $[M_A]$ was being underestimated. However, as the bandwidth was increased, the convergence was not monotonic. In fact, in some of the modes, as the bandwidth was increased, the frequency went below that predicted when the full added mass matrix was used. This finding indicated that at some points, the added mass matrix $[M_A]$ was overestimated.

This method did not save any time in the formation of the added mass matrix, but it reduced solution times in : 1) the formation of the new global mass matrix MASSM; 2) the decomposition of the global matrices DECOM; and 3) the eigenvalue problem EIGEN, since all of these were very dependent on the bandwidth of the matrices involved. (The percentage reduction in the CPU times for a few of the bandwidths imposed are tabulated in

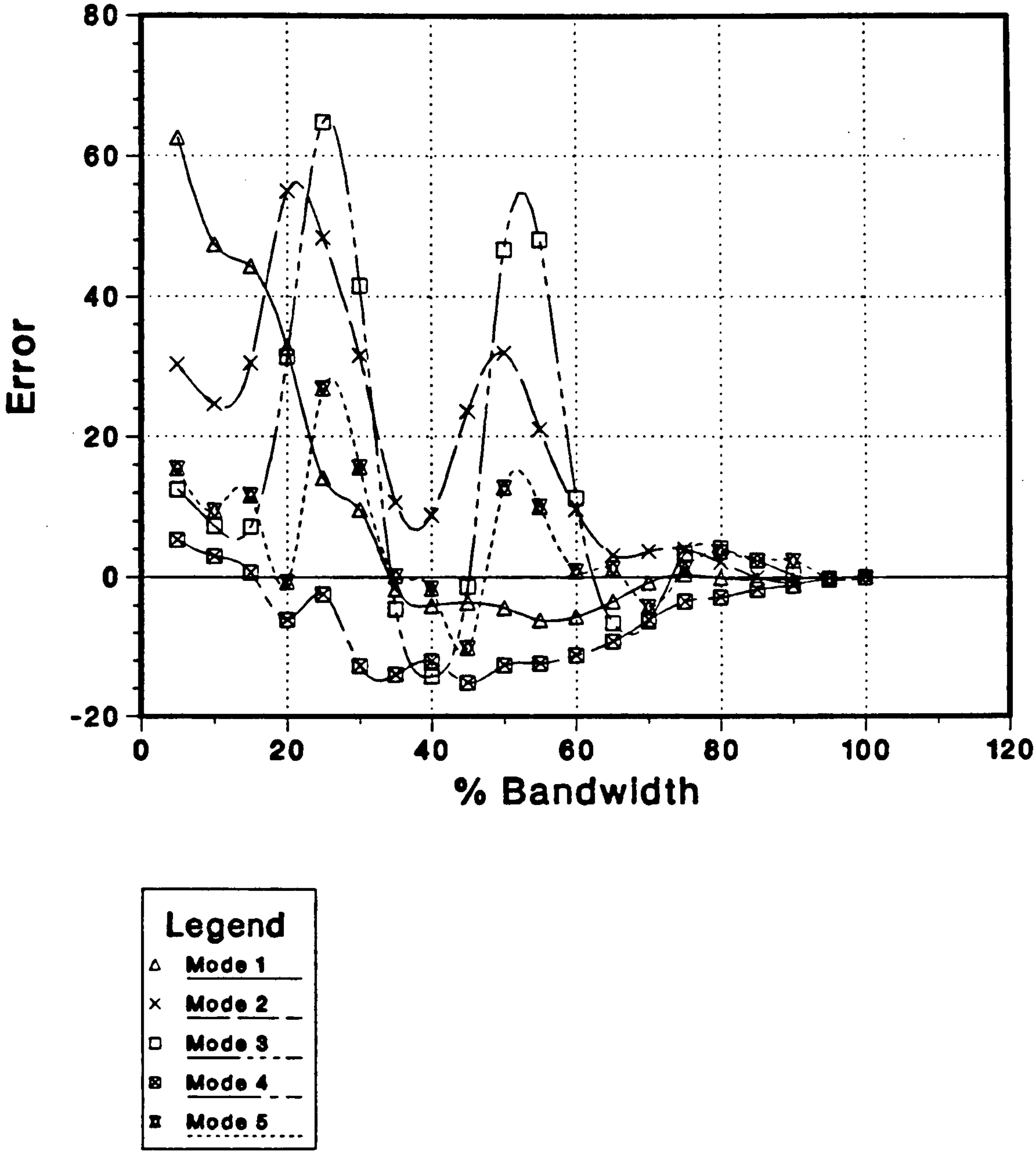

Figure 3.19 - Error Produced by Imposing an Artifical Bandwidth Using 8-Noded Fluid Elements with Plate Aspect Ratio a/b = 1.0

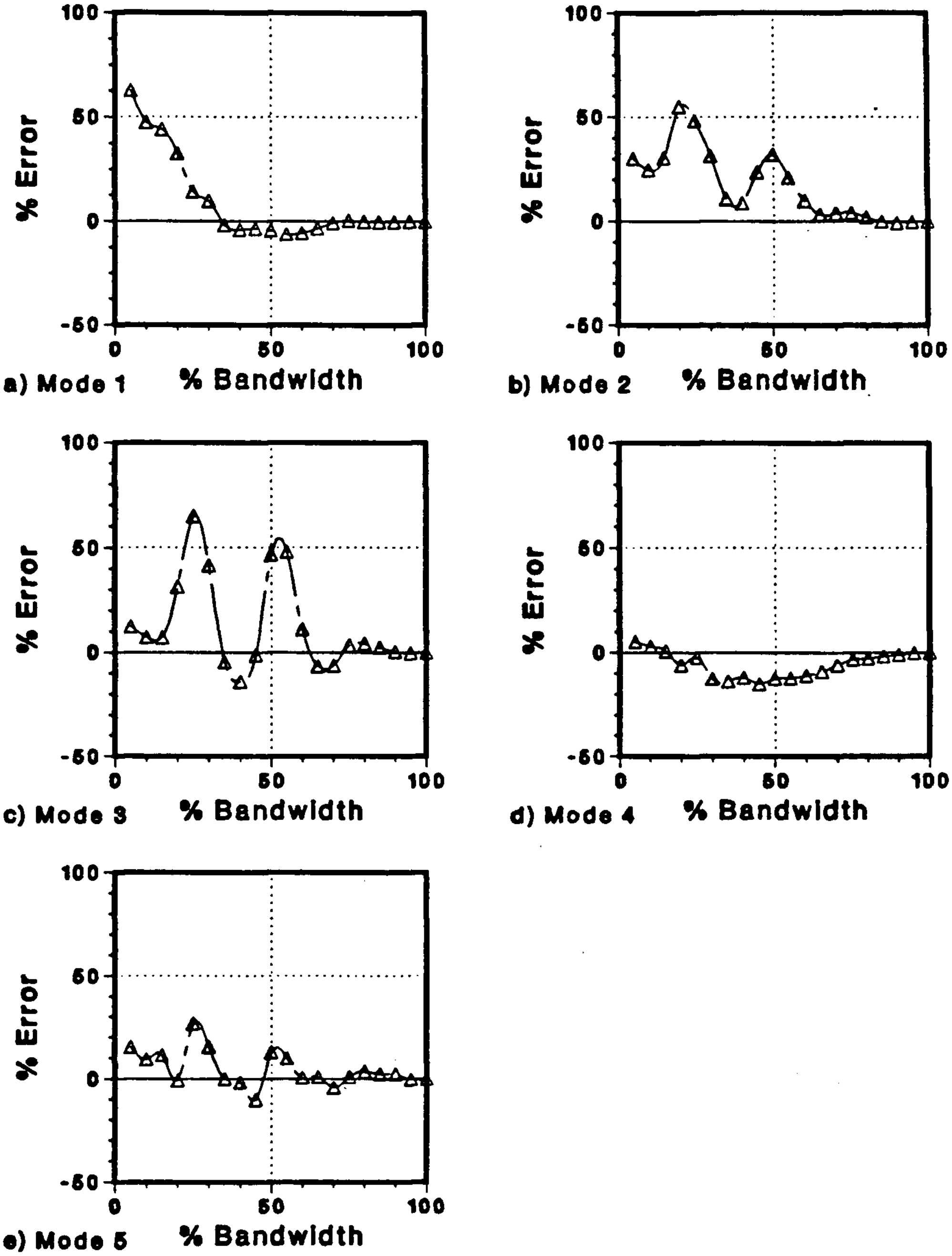

Figure 3.20 - Error Produced by Imposing an Artifical Bandwidth Using 8-Noded Fluid Elements with Plate Aspect Ratio a/b = 1.0 for Individual Modes 1 - 5

Table 3.8.) In the test problem the reduction in CPU times was not that significant, since the bandwidth of the structural matrices was eleven, which was comparable to that of the added mass matrix. The bandwidth of the structural matrices corresponded to a bandwidth reduction of 55 percent for the added mass matrix. Thus, there was no decrease in the CPU times after the bandwidth of the added mass matrix $[M_A]$ went below 55 percent.

	% Reduction in		
Bandwidth	MASSM	DECOM	EIGEN
5 %	33	2	21
25 %	25	2	19
50 %	17	2	12
75 %	8	1	3
100 %	0	0	0

Table 3.8 - Solution Times in Various Routines for Bandwidth Reduction

4. EXPERIMENTAL DETERMINATION OF THE VIBRATION RESPONSE OF A SHIP MODEL IN AIR AND WATER

This chapter will describe the experimental work that was performed for comparison with numerical results. A model of a ship-like structure was designed, built, and studied for its dynamic behaviour under various load conditions in air and water.

4.1 Model Construction

In order to construct a model of a ship, many variables had to considered. Of prime importance was the model's ability to reproduce the dynamic behaviour of the full size ship. Other issues were important too, and, as is often the case in model scaling, not all of these issues could be satisfied by the same model. In order to determine which properties were important and what material should be used, a dimensional analysis of the relations that govern the vibration of a ship structure was conducted. (The details of the dimensional analysis of the model are discussed in Appendix D.)

From the considerations of dimensional analysis, material constraints, and ease of construction, the dimensions of the model were determined (as shown in Figure 4.1). The material of construction chosen was acrylic. The length of the model was determined as 8 feet, since the acrylic sheet was 8′ x 4′ and the construction of a two piece hull would have been very difficult. The cross-sectional shape of the hull was chosen to be constant and semicircular over the length of the model, as this made it easy to form. Furthermore, the semicircular shape was a convenient shape for which the added mass could be calculated using Strip Theory.

The main hull was formed by heating the acrylic to just below its critical temperature and then bending it over a mold of the correct form, to produce the desired semicircular shape of the hull. This work was contracted out, since the University of British Columbia's Department of Mechanical Engineering did not have the facilities that would allow the sheet of acrylic to be heated uniformly to the correct temperature.

The bulkheads were semicircular, to match the shape of the hull. They were cut from a 6 mm sheet of acrylic on the

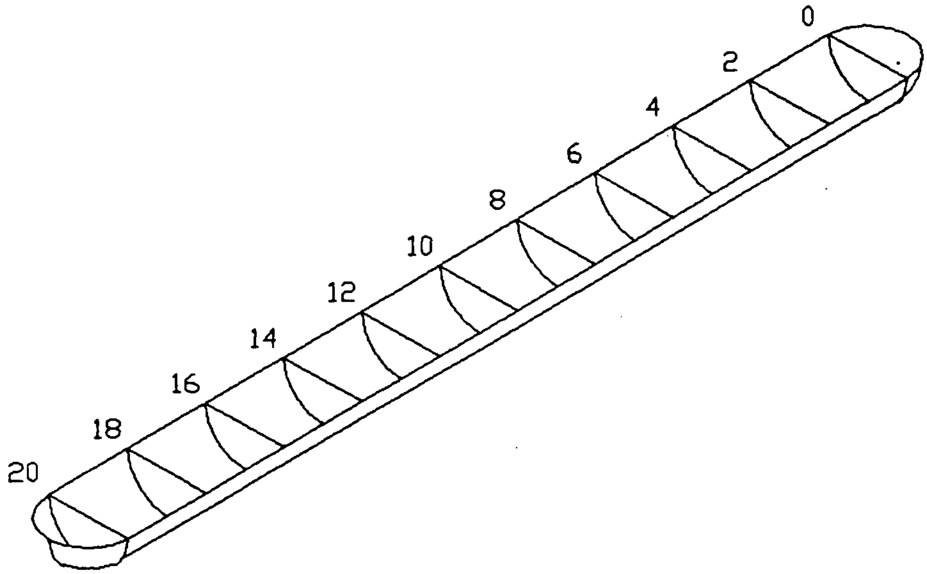

Length (between end bulkheads) 96" (2438mm)

Beam 8.391" (213mm)

Hull Thickness 0.079" (2mm)

Bulkhead - Thickness 0.236" (6mm)

- Diameter 8.3125" (211mm)

Endcaps - Thickness 0.079" (2mm)

- Radius 4.196" (107mm)

Unloaded Weight 5.56 lb (2530 grams)

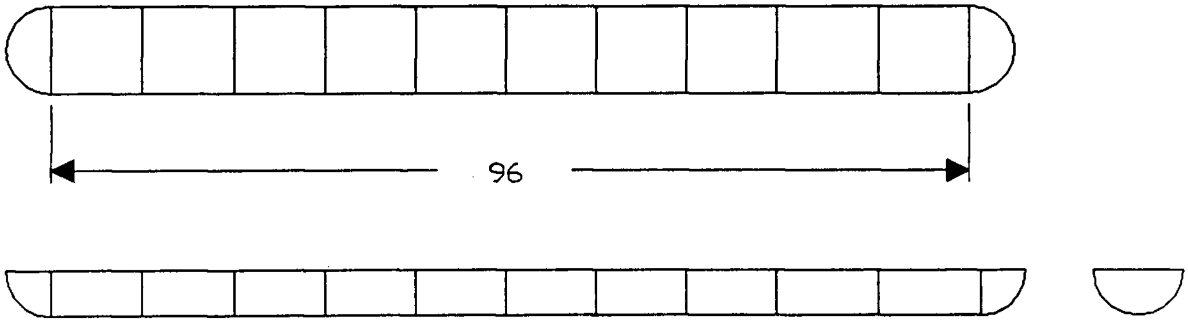

Figure 4.1 - Ship Model

Department of Mechanical Engineering's XLO numerically controlled vertical milling machine. This machine was used so that all of the bulkheads would be exactly the same. Eleven bulkheads were used in the construction of the model (as shown in Figure 4.1). They were cemented in place by an acetate solvent.

Endcaps of a semispherical design were attached to the ends of the hull to reduce any discontinuities in the fluid flow in these areas when the model was vibrating in water. If the model ended abruptly, the discontinuities would cause vortex shedding which could not be accounted for in the numerical models. The semispherical endcaps would allow for a smooth transition, reducing the effect of the discontinuities. However, the semispherical shape proved difficult to form since a sphere is an undevelopable surface. This problem was overcome by breaking the endcaps into eight sections and approximating each section as a wedge. (This procedure is illustrated in Figure 4.2.) The wedges were then bent over a circular form, and the eight wedges were cemented together using an acetate solvent, thus forming the semispherical endcaps. Finally, the endcaps were cemented to the main semicircular part of the hull, completing the construction of the model. As with the bulkheads, the wedges were cut on the numerically controlled vertical milling machine.

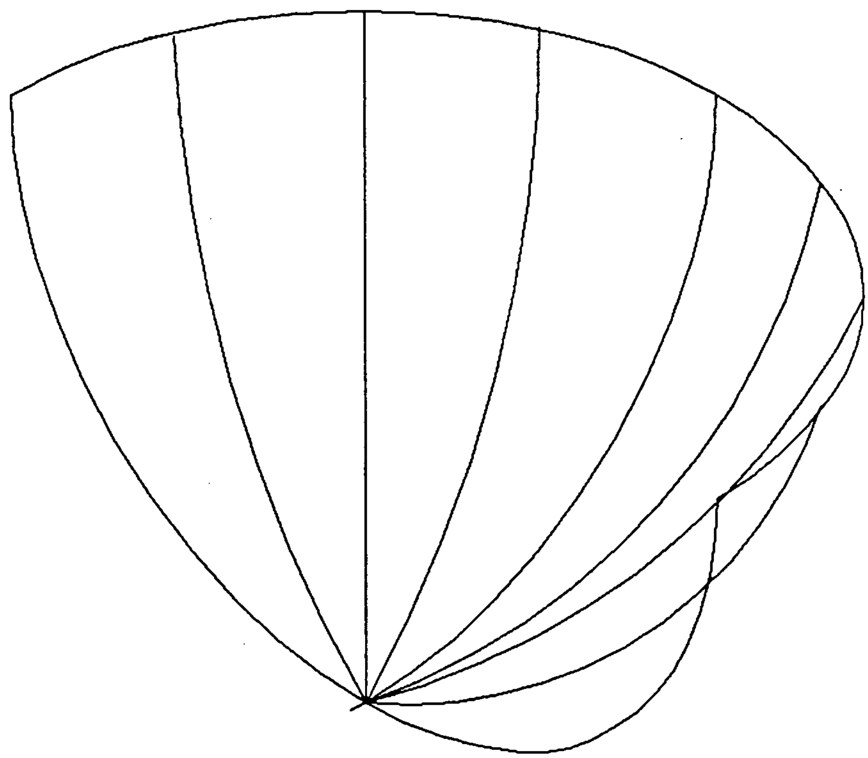

a) Assembled Endcap

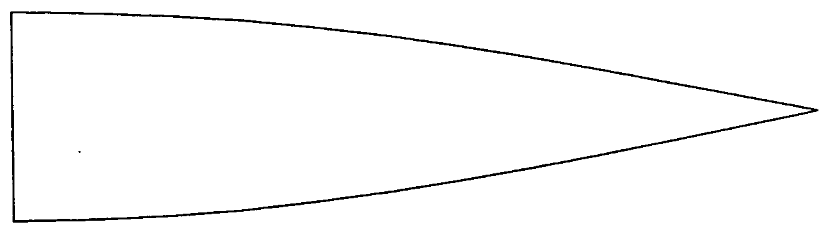

b) Wedge Shape

Figure 4.2 - Endcap and Wedge

4.2. INSTRUMENTATION

The instrumentation used to measure the frequencies and mode shapes of the ship model is described in this section. (For a complete list of the instrumentation and equipment used, see Appendix E. Figure 4.3 shows a schematic diagram of the instrument chain.)

Two Brüel & Kjær accelerometers, type 4332 and 4370, were used. These were piezoelectric type accelerometers whose electrical output was directly proportional to the acceleration they were experiencing.

The nominal specifications of the two accelerometers (given in Table 4.1) needed to be confirmed before any measurements were taken. (See Section 4.3.)

	Type 4332	Type 4370
Weight (grams)	35	54
Voltage Sensitivity mV/ms^{-2}	—	10
Charge Sensitivity pC/ms^{-2}	6.4	10
Frequency Range Hz	0.5 - 2000	0.2 - 3500

Table 4.1 - Nominal Accelerometer Specifications

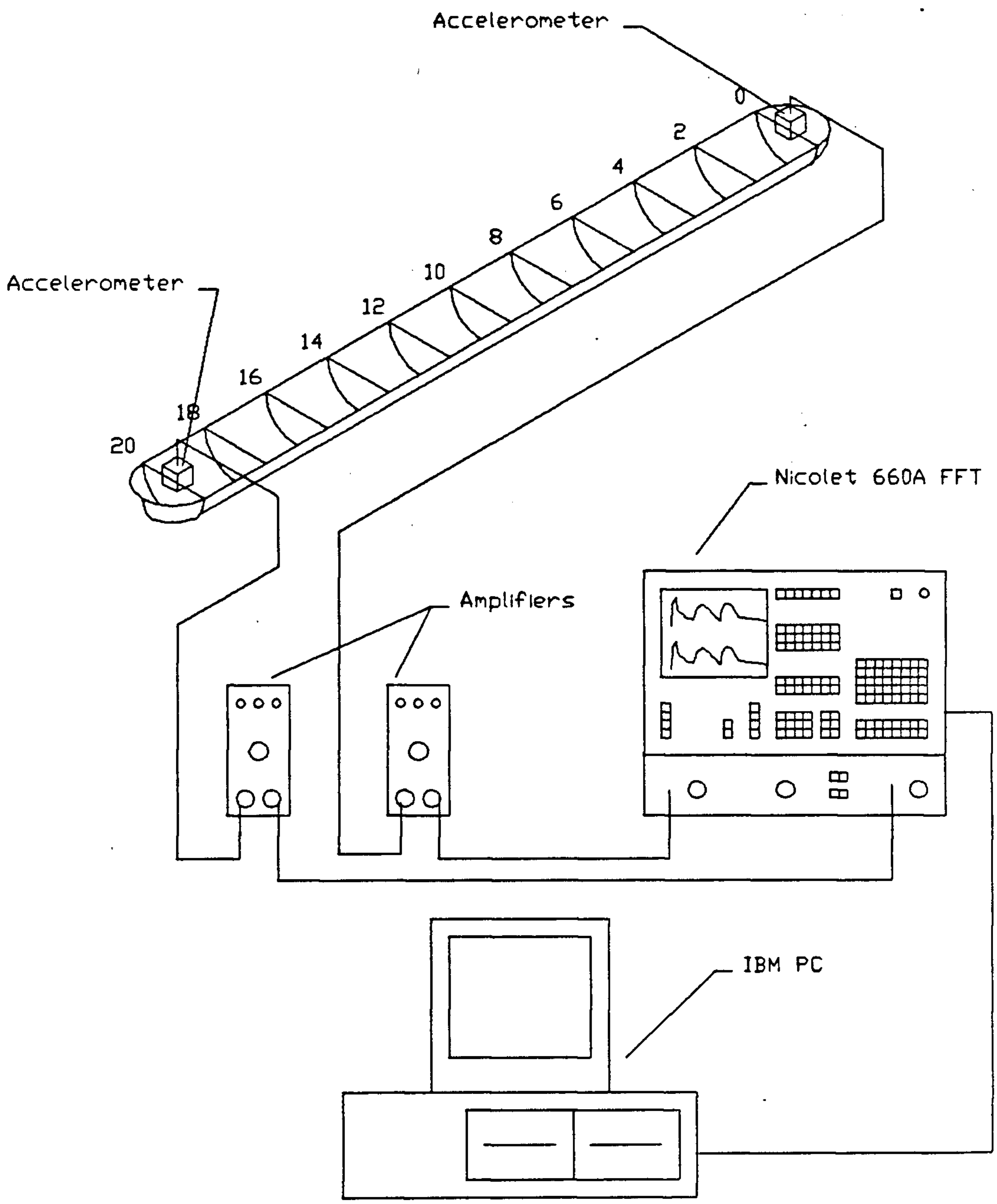

Figure 4.3 - Instrument Chain Schematic

The electrical signals from the piezoelectric accelerometers were amplified by two Brüel & Kjær type 2635 charge preamplifiers. The 2635 was only sensitive to variations in charge produced by the accelerometer when it was in motion. Thus, any length of cable might have been used without influencing the system's charge sensitivity.

The 2635 charge amplifier offered comprehensive signal conditioning for measurement of acceleration, velocity, and displacement. The front panel of the 2635 allowed the charge sensitivities of the accelerometers to be set between 0.1 and 11 pC/ms^{-2}. As well, the sensitivity of the amplifier allowed outputs of 0.1 to 1000 mV per m/s^{-2} for measurements of vibrational accelerations. Also included were high and low pass filters which were used to prevent the influence of noise and accelerometer resonance when the measurements were made. The high pass filters were 0.2 and 2 Hz, while the low pass filters were 0.1, 1, 3, 10, 30, and >100 kHz.

A Nicolet 660A Dual Channel Fast Fourier Transformer (FFT) analyser was used to analyse the accelerometer's signals. The Nicolet allowed the time domain voltage signals A(t) from two accelerometer/charge amplifier sets to be transformed into the frequency domain by performing a fast Fourier transformation on the incoming signals. The instantaneous FFT was calculated from the incoming time signal as

$$S_A = \mathcal{F}\{A(t)\}$$

$$S_A = |S_A|\cos(\varphi_A) + j|S_A|\sin(\varphi_A)$$

where the subscript indicated the channel, A(t) was the time signal, $\mathcal{F}\{\ \}$ the direct Fourier transform, S_A the complex spectrum, and φ_A the phase angle. The RMS Spectrum of channel A was given as

$$\text{RMS Spectrum} = \sqrt{S_A \cdot S_A^*}$$

where S_A^* was the complex conjugate of S_A. The Transfer Function was given as

$$H_{AB} = \frac{G_{AB}}{G_{AA}}$$

where

$$G_{AA} = S_A \cdot S_A^*$$

and

$$G_{AB} = S_B \cdot S_A^*$$

Finally, the Coherence was given by

$$\gamma_{AB}^2 = \frac{G_{AB} \cdot G_{AB}^*}{G_{AA} \cdot G_{BB}}$$

A PCB Piezotronics 208 A03 impact hammer was used to excite the ship model. The tip of the impact hammer was removable, allowing different tips to be used. This impact hammer had three different tips : a rubber tip, a plastic tip, and a steel tip. The different tips allowed the energy content of the impulse to be adjusted.

4.3 Experimental Procedure

The experimental procedure followed for the model testing was developed over a number of tests. The final procedure that was adopted will be presented here.

4.3.1. Calibration of Instrumentation

The two accelerometers were calibrated using a Brüel & Kjær type 4291 accelerometer calibrator. The 4291 was a small portable vibration exciter producing a reference acceleration of 10 ms^{-2} (1.02g) with its peak at 79.6 Hz. The nominal charge sensitivity (listed in Table 4.1) was set on the 2635, and then the voltage output of the 2635 was adjusted until a reasonable voltage signal was registered on the oscilloscope, in the order of 2 volts peak to peak. The charge sensitivity was then fine-tuned until the voltage output from the 2635 matched with the readings on the oscilloscope. (Figure 4.4 shows the oscilloscope trace of the calibration for the two accelerometers.)

The charge sensitivity of the two accelerometers was found to be :

Brüel & Kjær Type 4332 Accelerometer 6.50 pC/ms^{-2}

Brüel & Kjær Type 4370 Accelerometer 10.08 pC/ms^{-2}

These results were quite close to the nominal specifications listed in Table 4.1.

Piezoelectric accelerometers are very high impedance devices and are susceptible to noise generated by the connecting cables. Any motion of the connecting cables would cause the capacitance of the cables to change. This change in capacitance would affect the charge in the system, causing erroneous readings. To keep this effect to a minimum, the cables were clamped to prevent or limit their relative motion. This procedure was followed for all the tests that were carried out on the model.

The criterion for choosing a tip for the impact hammer was that the power level of the signal produced through the range of frequencies of interest should be fairly level. The frequency range of interest for the model tests was 0 - 100 Hz.

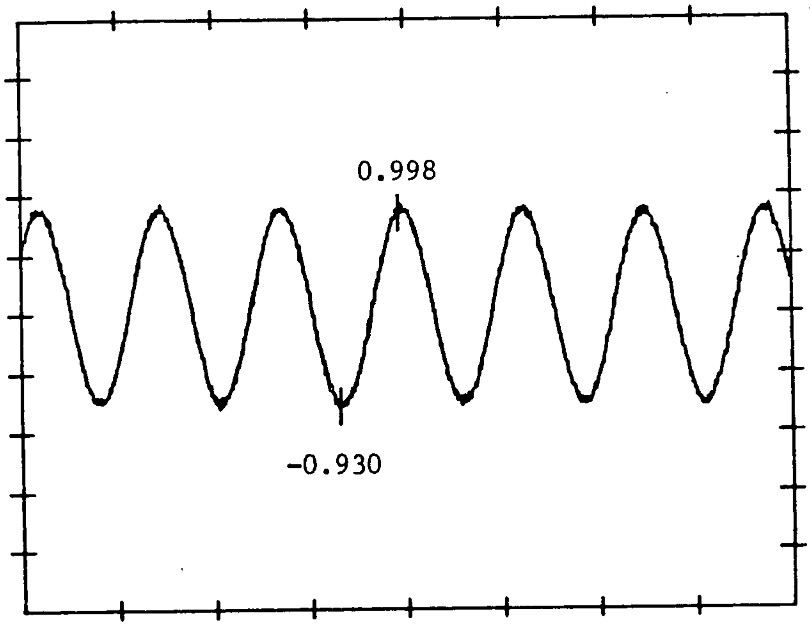

a) Accelerometer Type 4332

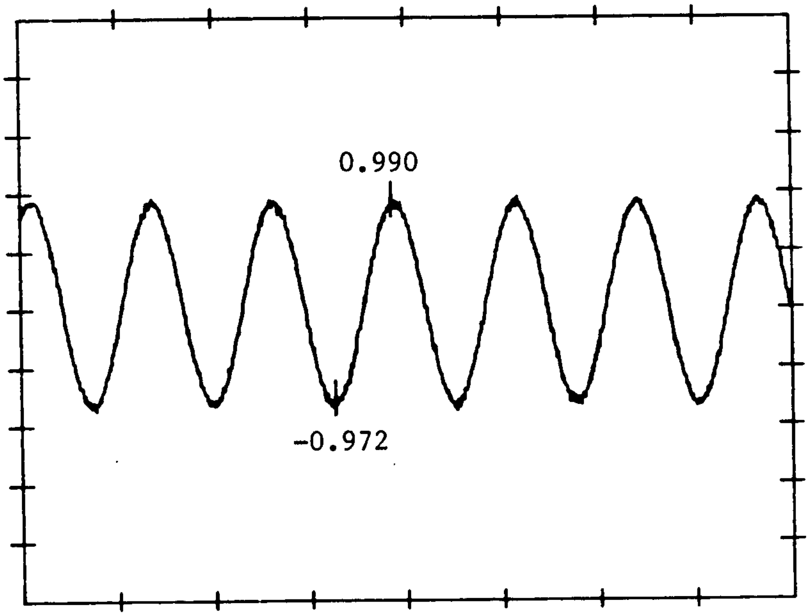

b) Accelerometer Type 4370

Figure 4.4 - Calibration of Accelerometers

Thus, with the Nicolet 660A FFT set to display the power spectrum of the impulse, a few tests were carried out with each tip. It was found that the plastic tip gave the best results (as shown in Figure 4.5). With the steel tip, it was easy to get a double hit.

4.3.2. Experimental Set Up For Air and Water Tests

The free-free frequencies and mode shapes of vibration for the model in air and water needed to be determined and compared. The water tests presented no problem, since the water supported the ship; but, the air tests presented a problem, since it is difficult if not impossible to perform free-free tests in air. For the air tests, the model needed to be supported without affecting the frequencies or the mode shapes of vibration. Clearly, this was a difficult task.

A frame was constructed that would allow the model to be supported by elastic cords. (The frame and model set up for the air tests is shown in Figure 4.6.) To determine if this set up had any effect on the vibration characteristics of the model, the tension of the elastic cords and their placement was varied, and vibration tests were performed. From these tests it was determined that : the placement of the elastic cords had little

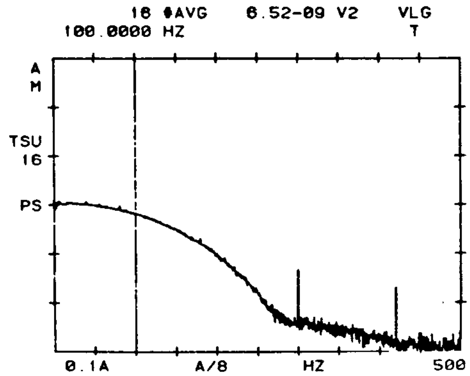

a) Rubber Tip

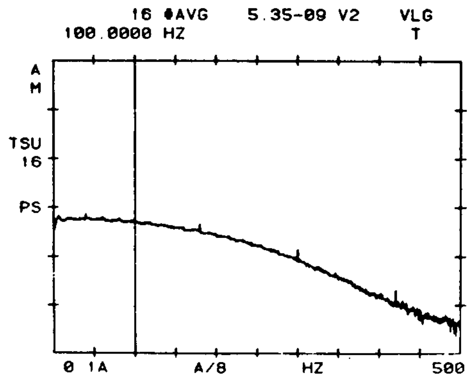

b) Plastic Tip

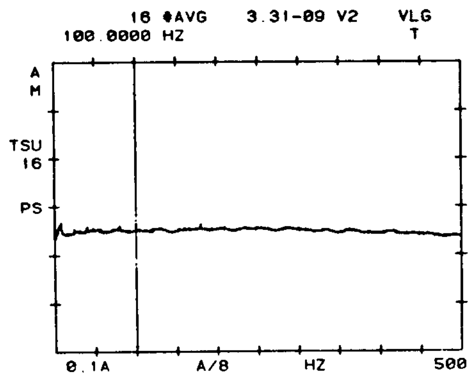

c) Steel Tip

Figure 4.5 - Power Spectrum for the Various Tips of the Impact Hammer

effect on the frequencies and mode shapes of vibration; and; the tension had no effect on the vibration characteristics, except for the rigid body modes (which were of no concern in these tests). However, only the vertical modes were checked since the horizontal and torsional modes had not been identifed yet. Subsequently a finite element model that modelled the stiffness of the elastic cords was examined. (These finite element results are displayed in Table 4.2.) These results show that the elastic cords had some effect on the frequencies of vibration.

Mode	EXP	OLD FE	NEW FE
2NDV/2NDH	12.5	12.11	13.17
3NDH/3NDT	23.5	49.23	51.23
3NDV	33.25	32.34	34.23
4NDH/4NDT	40.75	59.94	56.96
4NDV	60.75	60.88	62.24
5NDV	92.0	95.31	93.81

Table 4.2 - Comparison of Experimental and Finite Element Results for 30 lb Load Condition

The water tests were carried out in the towing tank of The Ocean Engineering Center of B.C. Research. The towing tank was 220 feet in length and 12 feet wide, with a water depth of 8 feet. At one end of the tank, there was a preparation dock. This

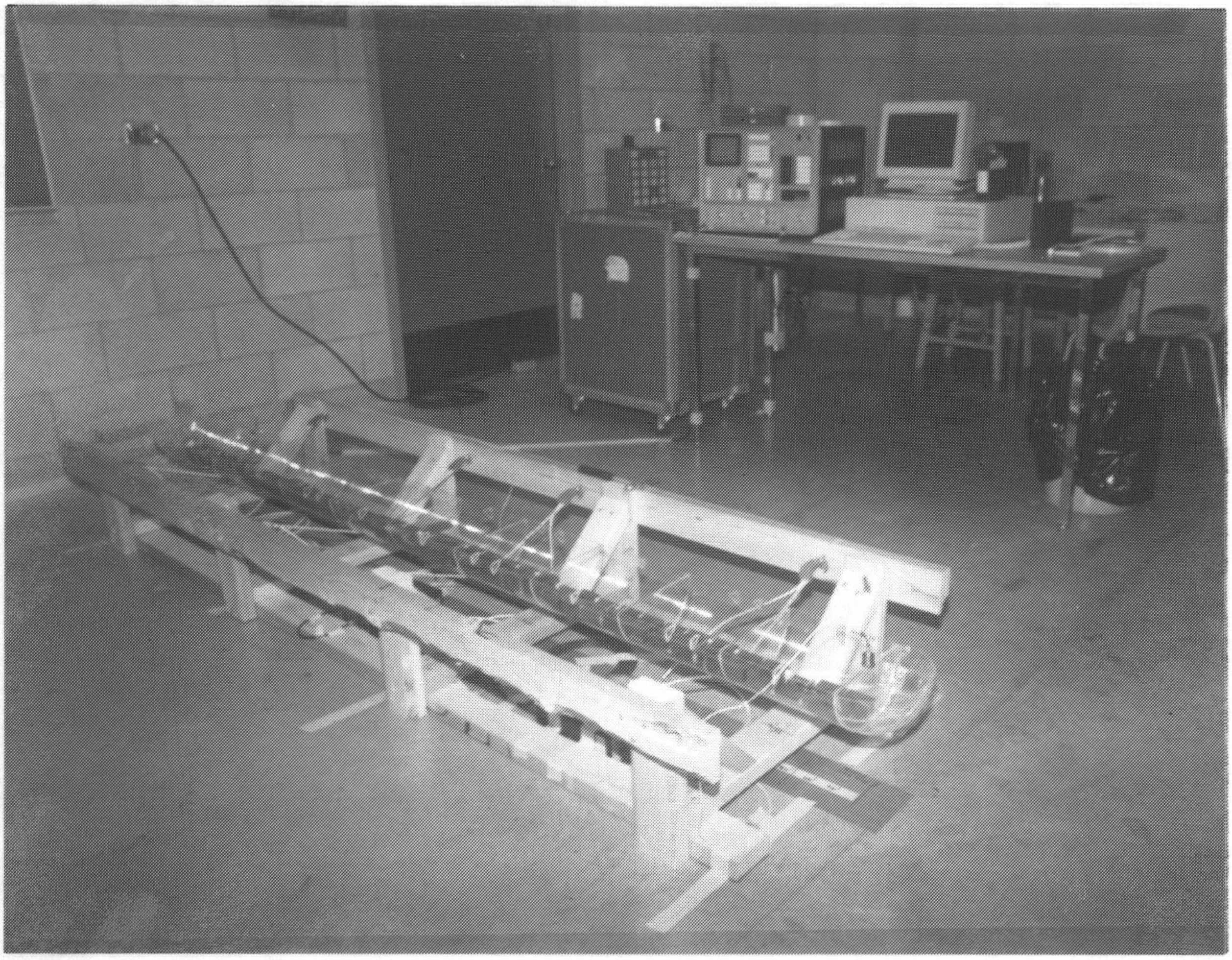

Figure 4.6 - Experimental Set Up for Air Tests

dock area could be isolated from the main towing tank and was 12 feet long, 3 feet wide, and 4 feet deep, with a water depth of 37 inches. A vibration test was first performed with the model in the middle of the towing tank and then with the model in the middle of the preparation dock, and the results were compared. It was found that there was no difference between the results, so the remaining tests were performed in the preparation dock, as it was easier to test there. (Figure 4.7 shows the experimental set up for the water tests.)

4.3.3. Different Load Conditions

The tests were conducted with six different load conditions. These load conditions were obtained by placing discrete lead weights in 40 positions along the length of the model. Each weight was 2.5" x 2" x 0.125" and had a nominal value of 0.25 lbs. Thus, placing 40 weights along the length of the model produced a load of 10 lbs. Five of the load conditions were uniform loads, with the load being varied from 30 lbs to 70 lbs in 10 lbs increments. These load conditions produced different drafts (as shown in Table 4.3). The sixth load case was a non-uniform load condition with a total weight of 70 lbs. The individual weights were distributed to model an actual mass

Figure 4.7 - Experimental Set Up for Water Tests

distribution in a real ship; however, the model had to remain on an even keel since the free board with 70 lbs was very small. (Figure 4.8 shows this distribution.)

Load Cond. lbs	30	40	50	60	70
Drafts Inches	3.511	3.720	3.877	3.995	4.083

Table 4.3 - Load Conditions and Drafts of the Model

4.3.4. Natural Frequency and Mode Shape Determination

The accelerometers were mounted at various stations on the model using bee's wax. The accelerometer type 4370 was always at station zero (the bow), while the accelerometer type 4332 was moved from station to station. The RMS Spectrum, Transfer Function, and the Coherence were measured at each of the twenty-one stations along the length of the model to determine the mode shapes of the model. With the two accelerometers at their respective stations, an impulse was applied to the model with the impact hammer and the results recorded. Sixteen measurements were taken and averaged to reduce the error at each of the twenty-one stations numbered 0 - 20 along the length of the ship. After the Nicolet had processed and averaged the sixteen signals, the information was transferred to floppy disks, using the program MAP

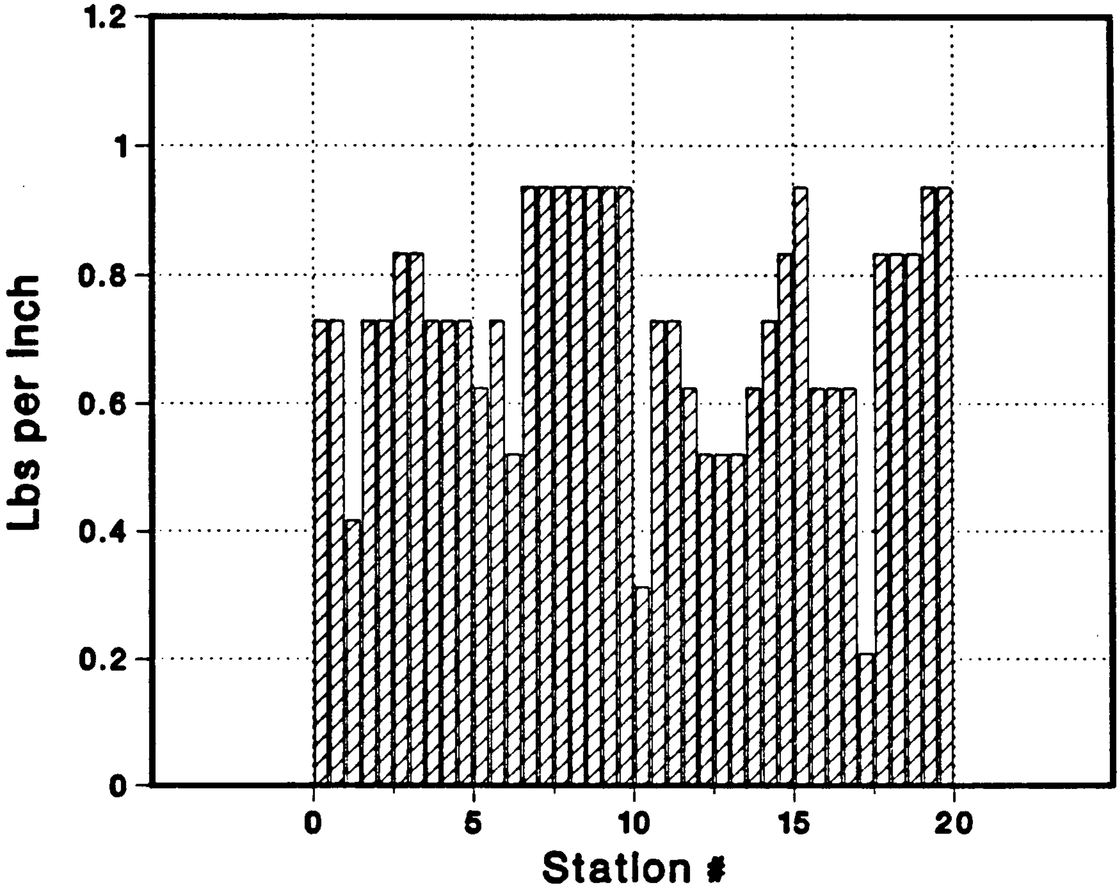

Figure 4.8 - Non-Uniform Load Condition

(discussed below in Section 4.3.5). The accelerometer type 4332 was then moved to the next station, and the procedure described above was repeated for all twenty-one stations.

For each load condition, three separate tests were conducted. Each of these tests was performed to excite a different type of mode of vibration. To excite the vertical bending modes, the ship was hit vertically on the centerline at station 8 or 12, with the two accelerometers mounted vertically on the centerline. To excite the horizontal bending modes, the ship was hit horizontally along the starboard gunnel at station 8 or 12, with the two accelerometers mounted horizontally along the port gunnel. To excite the torsional modes, the ship was hit vertically along the starboard gunnel at station 20, with the two accelerometers mounted vertically along the port gunnel.

The natural frequencies of the ship were identified as those frequencies at which peaks occurred in the RMS Spectrum of the Nicolet. (This method of determining the natural frequencies of a structure is known as the Peak Amplitude Method.)

To determine the mode shape of vibration, two pieces of information were needed at each of the stations along the length of the ship : the magnitude of the Transfer Function and the phase angle at the natural frequencies of interest. . The magnitude of the Transfer Function at each station gave the relative value of mode shape at that point, while the phase angle φ indicated if the two accelerometers were moving in the same direction, indicated by $\varphi = 0^{\circ}$, or in opposite directions, indicated by $\varphi = 180^{\circ}$. By plotting the magnitude and noting the phase angle, the mode shape was obtained.

4.3.5. Data Acquisition Program

To help with the acquisition and processing of the experimental data, a computer program called MAP (Modal Analysis Program) was written. This program allowed the information on the Nicolet 660A from one station to be down-loaded onto floppy disks for storage and further processing. With this information stored on floppy disks, three functions could be performed by the PC. The program could mimic the Nicolet by displaying the RMS Spectrum, Transfer Function, or Coherence of one station. It could also be used to send the information back to the Nicolet for further processing. And finally, it could be used to determine the mode shapes of vibration for the model in its various load conditions. This program (given in Appendix F) was written in Turbo Pascal on an IBM Personal Computer. The PC was utilized because of its portability.

4.4. Experimental Results

Using the experimental procedure (described above in Section 4.3), the natural frequencies and mode shapes for the ship model were found. The first four modes of vertical bending, the first four modes of horizontal bending, and the first four modes of torsion for the ship model were identified both in air and water for each of the five uniform load conditions and the one non-uniform load condition.

4.4.1. Frequencies

The frequencies of vibration for the various modes and load conditions were examined (and are shown in Tables 4.4 - 4.6). There were a few modes that could not be identified in certain load conditions and thus they have been left blank.

	2-Node		3-Node		4-Node		5-Node	
Load cond.	Air	H_2O	Air	H_2O	Air	H_2O	Air	H_2O
30 lb	12.5	7.75	33.25	21.25	61.75	40.75	92.0	65.75
40 lb	11.25	7.25	29.5	19.75	55.25	38.0	82.0	61.0
50 lb	10.5	7.0	27.25	18.5	50.5	35.5	74.5	56.75
60 lb	10.0	6.5	25.25	17.75	46.75	33.75	67.75	53.25
70 lb	9.5	6.25	23.5	16.75	43.0	32.5	63.0	50.5
Non-Uniform	9.25	6.25	23.5	16.75	42.25	32.0	61.25	50.75

Table 4.4 - Frequencies for the Vertical Bending Modes

	2-Node		3-Node		4-Node		5-Node	
Load cond.	Air	H_2O	Air	H_2O	Air	H_2O	Air	H_2O
30 lb	12.0	7.75	23.5	16.0	40.75	27.75	62.75	43.75
40 lb	11.5	7.0	22.0	14.25	37.75	25.0	57.75	39.25
50 lb	10.75	6.5	20.5	13.0	35.25	22.75	52.25	35.5
60 lb	10.25	6.75	18.75	12.0	33.0	20.5	48.25	32.25
70 lb	9.5	5.75	17.75	11.0	30.25	18.75	44.0	29.75
Non-Uniform	9.25	-	17.5	11.0	29.5	18.75	-	29.5

Table 4.5 - Frequencies for the Horizontal Bending Modes

	1-Node		2-Node		3-Node		4-Node.	
Load cond.	Air	H_2O	Air	H_2O	Air	H_2O	Air	H_2O
30 lb	11.25	5.5	45.5	41.5	23.5	16.0	40.5	28.0
40 lb	12.25	5.25	43.25	37.5	22.0	14.5	37.5	25.0
50 lb	12.75	5.25	-	-	20.75	13.0	34.75	22.5
60 lb	13.5	6.0	-	-	19.5	12.0	32.75	20.75
70 lb	13.5	4.5	39.25	31.5	18.25	11.0	-	-
Non-Uniform	13.5	4.75	-	31.25	18.0	11.0	-	18.75

Table 4.6 - Frequencies for the Torsional Modes

By examining the frequencies of vibration for the various modes, it was determined that some of the modes were coupled together. The 2-node vertical mode was coupled to the 2-node horizontal mode. (Table 4.7 displays the center of shear and the center of mass for the various load conditions. The values given in Table 4.7 are distances below the top of the bulkheads.) Since the center of shear and the center of mass for this model did not correspond, the horizontal and torsional modes of vibration were coupled, as discussed by Bishop and Price [9-13]. The 3-node horizontal and the 3-node torsional modes were coupled, while the 4-node horizontal and 4-node torsional modes were also coupled.

Load Cond.	Center of Mass	Center of Shear
30 lb	3.694 inches	5.343 inches
40 lb	3.626 inches	5.343 inches
50 lb	3.537 inches	5.343 inches
60 lb	3.437 inches	5.343 inches
70 lb	3.331 inches	5.343 inches

Table 4.7 - Center of Mass and Shear for Various Load Conditions

The experimental results provided no information about which modes were dominate in the coupled modes, but by examining the finite element results it was possible to determine this. In the 2-node vertical-horizontal mode, the 2-node vertical mode was the dominate mode. However, in the 3-node horizontal-torsional and the 4-node horizontal-torsional modes neither mode was dominate instead both were equal in their energy contribution to the mode.

The frequencies of the 70 lb and the non-uniform load condition were very similar. The difference between the two load conditions was the distribution of the mass. The frequencies of the 70 lb and the non-uniform load condition were closer for the water tests. This similarity was due in part to the distribution of the added mass, which was uniform and on the order of the structural mass of the ship; thus, the effect of the water made the total mass distribution more uniform.

The results of the frequency of vibration in air and water for the various load conditions were examined. (See Figure 4.9 - 4.11.) It was seen that for vertical and horizontal motion in any mode, the frequencies decreased as the load condition increased. This was expected, since the stiffness of the structure was not affected by the load condition. Only the mass of the structure was affected, which lowered the frequency of vibration. As the mode number was increased, the slope of the lines increased as well, and the slope of the air results were larger than the slope of the water results. The torsional modes were not as well behaved. In fact, the 1-node torsional mode in air increased in frequency as the load condition was increased.

By comparing the frequencies in water with those in air, and by assuming that Beam Theory held, it was possible to calculate the apparent added mass in the vertical modes caused by the water. This was a reasonable assumption if the complexity of the modes were low, such that shear displacement and rotary inertia effects were not important. By comparing the experimental results with Beam Theory it was seen that the frequencies compared quite well, especially for the lower modes (as shown in

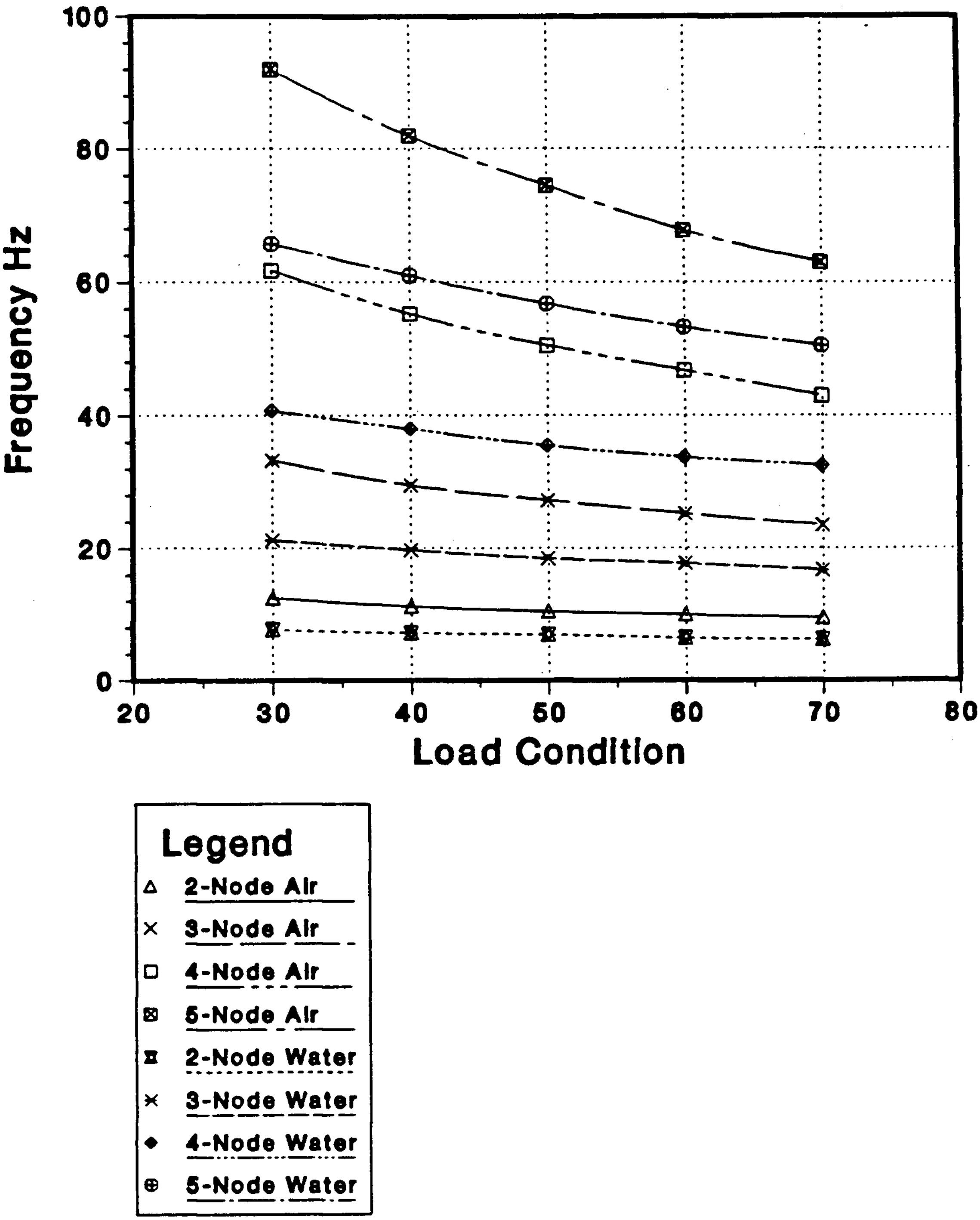

Figure 4.9 - Vertical Modes of Vibration for the Ship Model

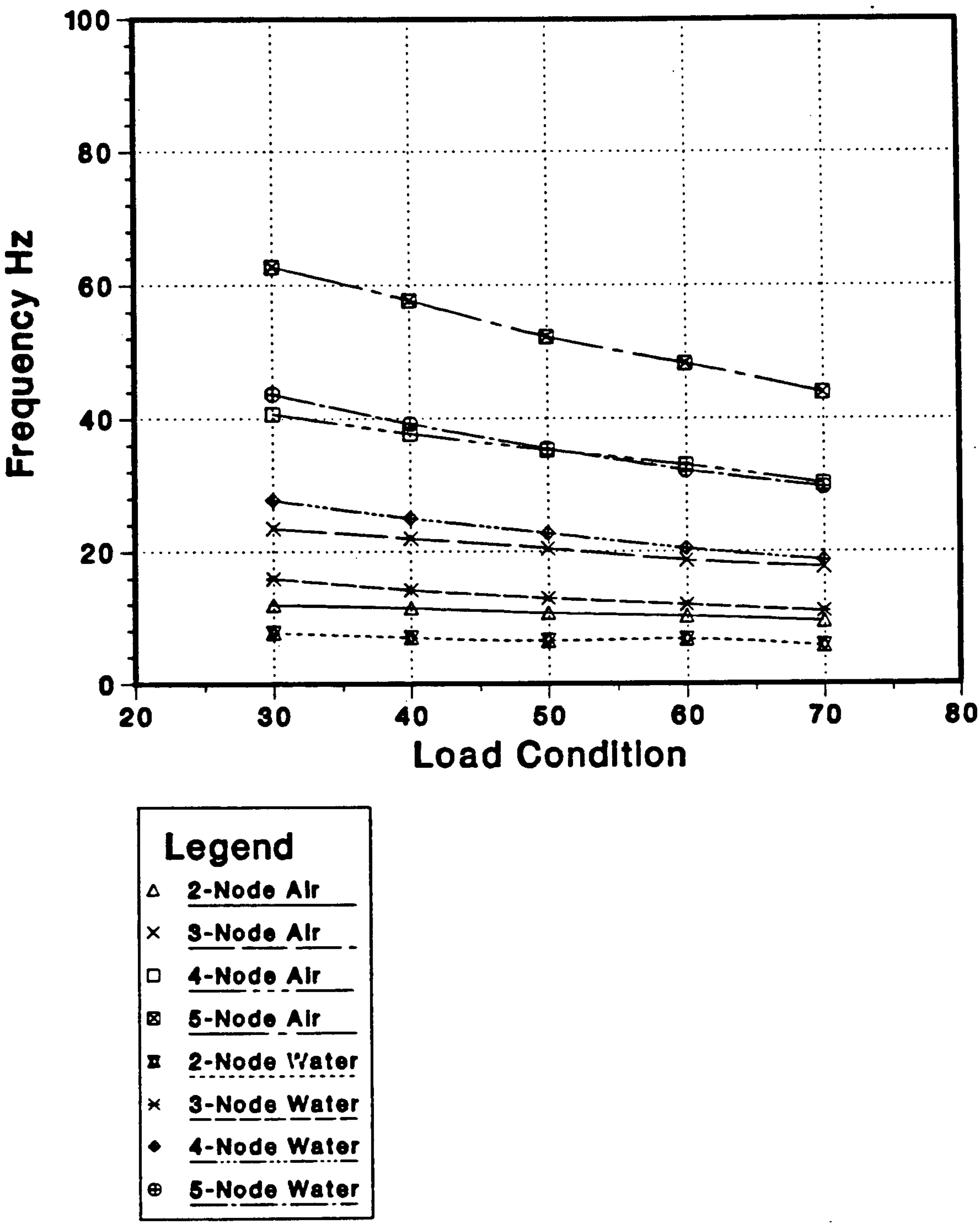

Figure 4.10 - Horizontal Modes of Vibration for the Ship Model

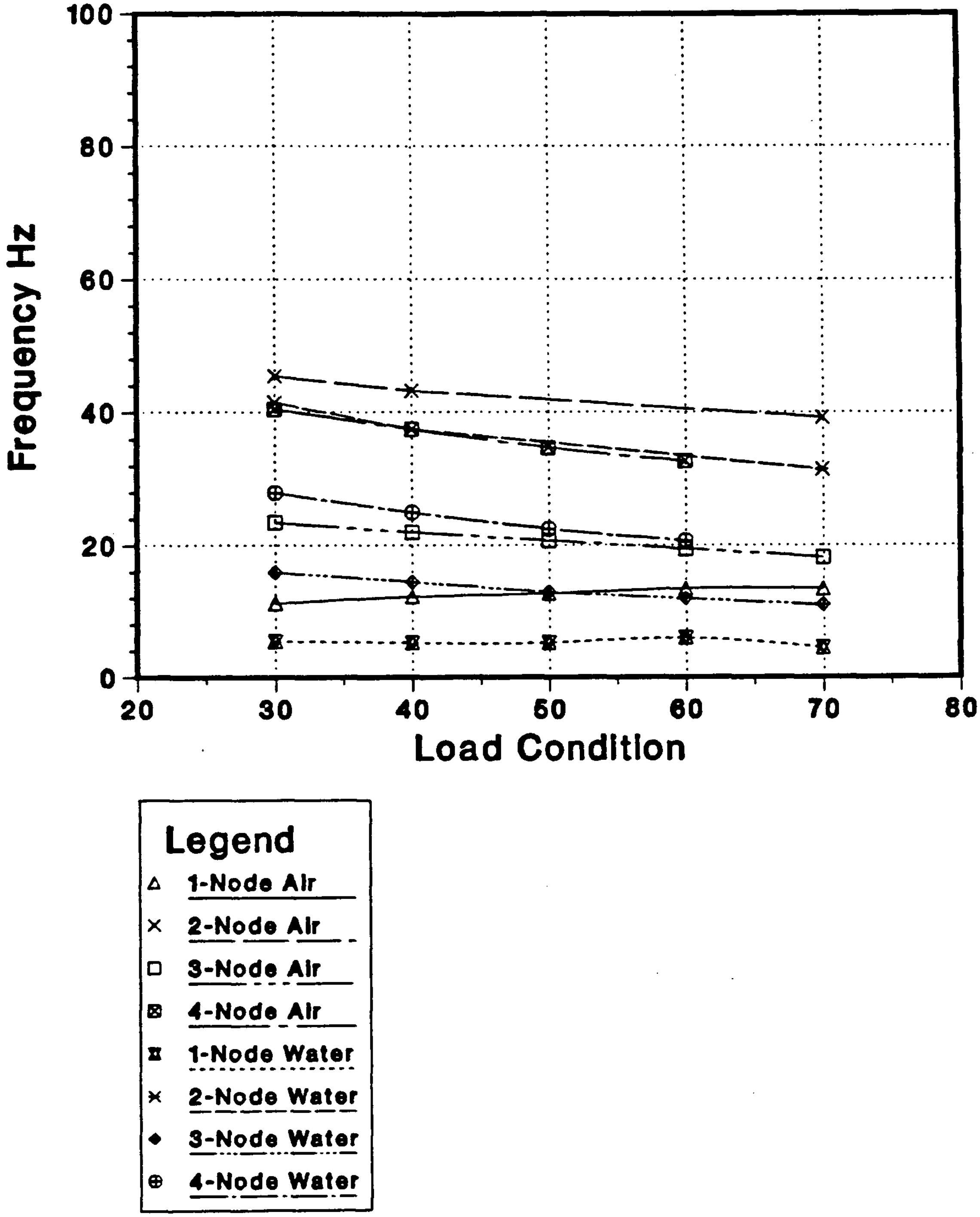

Figure 4.11 - Torsional Modes of Vibration for the Ship Model

Table 4.8). The frequency of a beam was given as

$$\omega_i = \frac{1}{2\pi}\left(\frac{\beta_i l}{l}\right)^2 \sqrt{\frac{EI}{m}} \text{ Hz} \qquad (4.1)$$

where $\beta_i l$ was a constant that depended on the end conditions of the beam and the mode of interest, l was the length of the beam, E was Young's modulus, I was the moment of inertia of the cross-section, and m was the mass per unit length of the beam.

	2-Node		3-Node		4-Node		5-Node	
Load cond.	EXP	TH	EXP	TH	EXP	TH	EXP	TH
30 lb	12.5	12.98	33.25	35.78	61.75	70.15	92.0	115.9
40 lb	11.25	11.47	29.5	31.61	55.25	61.97	82.0	102.4
50 lb	10.5	10.39	27.25	28.63	50.5	56.12	74.5	92.77
60 lb	10.0	9.56	25.25	26.35	46.75	51.66	67.75	85.40
70 lb	9.5	8.91	23.5	24.55	43.0	48.12	63.0	79.55

Table 4.8 - Experimental and Beam Theory Results in Air For Vertical Modes of Vibration

To determine the equivalent added mass, the ratio of the frequency in air to the frequency in water was needed. This was determined using the relations for a beam and noting that the frequency was inversely proportional to the mass of the structure; thus

$$\frac{\omega_A}{\omega_W} = \sqrt{\frac{m_W}{m_S}} \qquad (4.2)$$

where m_W was the combined mass in water given by $m_W = m_S + m_A$, with m_S equal to the mass of the structure and m_A equal to the added mass due to the effect of the water. After substituting the combined mass in water, equation 4.2 became

$$R_W = \frac{\omega_A}{\omega_W} = \sqrt{\frac{m_S + m_A}{m_S}} = \sqrt{1 + \frac{m_A}{m_S}} \tag{4.3}$$

Solving for the ratio of the added mass m_W to the structural mass m_S gave

$$R_M = \frac{m_A}{m_S} = \left[\left(\frac{\omega_A}{\omega_W} \right)^2 - 1 \right] \tag{4.4}$$

where m_S was equal to the mass of the structure per unit length plus the mass of the load condition per unit length.

The weight of the unloaded structure was 5.56 lbs.

	2-Node		3-Node		4-Node		5-Node	
Load cond.	ω_A/ω_W	m_A/m_S	ω_A/ω_W	m_A/m_S	ω_A/ω_W	m_A/m_S	ω_A/ω_W	m_A/m_S
30 lb	1.61	1.60	1.57	1.45	1.52	1.30	1.40	0.96
40 lb	1.55	1.41	1.49	1.23	1.45	1.11	1.34	0.81
50 lb	1.50	1.25	1.47	1.17	1.42	1.02	1.32	0.72
60 lb	1.54	1.37	1.42	1.02	1.39	0.92	1.27	0.62
70 lb	1.52	1.31	1.40	0.97	1.32	0.75	1.25	0.56

Table 4.9 - Ratios of Added Mass to Structural Mass

For Vertical Bending Modes

Upon examining the results for the vertical modes of vibration (as presented in Table 4.9), a few general trends were determined. While in a specific mode, if the load condition of the model was increased, the ratio of the added mass to the structural mass was seen to decrease. Thus, the added mass effect depended on the draft of the model, and its contribution to the total mass of the model was not a constant proportion of the model's mass. In fact, at shallower drafts the added mass effect was more significant than at deeper drafts. It was also seen that in a specific load condition, if the mode number increased, the ratio of added mass to structural mass decreased. Thus, the added mass effect decreased as the complexity of the mode increased.

Another method was also used to try to determine the added mass due to the fluid. This method used the finite element model of the structure in air. The density of the twenty-one bulkheads was increased until there was agreement between the experimental and finite element frequencies for a particular mode in the fluid. (These results are displayed in Table 4.10.)

	2-Node		3-Node		4-Node		5-Node.	
Load cond.	ω_A/ω_W	m_A/m_S	ω_A/ω_W	m_A/m_S	ω_A/ω_W	m_A/m_S	ω_A/ω_W	m_A/m_S
30 lb	1.58	1.50	1.52	1.33	1.50	1.33	1.48	1.17

Table 4.10 - Ratios of Structural Mass to Added Mass for Vertical Bending Modes Using Finite Elements

From these finite element results, it was seen that as the complexity of the modes increased, the ratio of the added mass to the structural mass decreased. This was the same conclusion found above using Beam Theory; however, the rate of decrease of the ratio of masses and frequencies was not as severe as with Beam Theory. Furthermore, (by examining the two tables) it was seen that the finite element results did not conform to equation 4.4. Thus, the effects of shear displacement and rotary inertia were present in the model.

4.4.2. Mode Shapes

With the Transfer Function data from the experiment, the mode shapes of the vibration were determined, as discussed (in Section 4.3.4) above. The resulting mode shapes in air and water were compared. This was accomplished by normalizing the two modes so that they had the same energy in air and water.

In equation form

$$a\int \Psi_A^2 \, dx = b\int \Psi_W^2 \, dx$$

where Ψ_A and Ψ_W were the mode shapes in air and water, respectively, with a = 1 and the value of b determined from

$$b = \sqrt{\frac{\int \Psi_A^2 \, dx}{\int \Psi_W^2 \, dx}}$$

The experimental mode shapes were in tabular form, after being processed by the MAP program, and, thus, needed to be numerically integrated. This was done using Simpson's rule

$$I = \frac{1}{3}\Delta\left[\Psi^2(x_0) + 4\Psi^2(x_1) + 2\Psi^2(x_2) + \ldots + 4\Psi^2(x_{2N-1}) + \Psi^2(x_{2N})\right]$$

where Δ was the distance between data points. (Figures 4.12 - 4.20 show the mode shapes of vibration of the ship in its 30, 40, and 70 lb load conditions.) In general, there was little difference between the mode shapes in air and water. However, the mode shape in water was generally smoother than the corresponding mode shape in air, indicating that the local bending effects were less in water. Local bending began to show up in the higher mode shapes.

In the model there were eleven bulkheads. These bulkheads were located at stations 0, 2, 4, 6, 8, 10, 12, 14, 16,

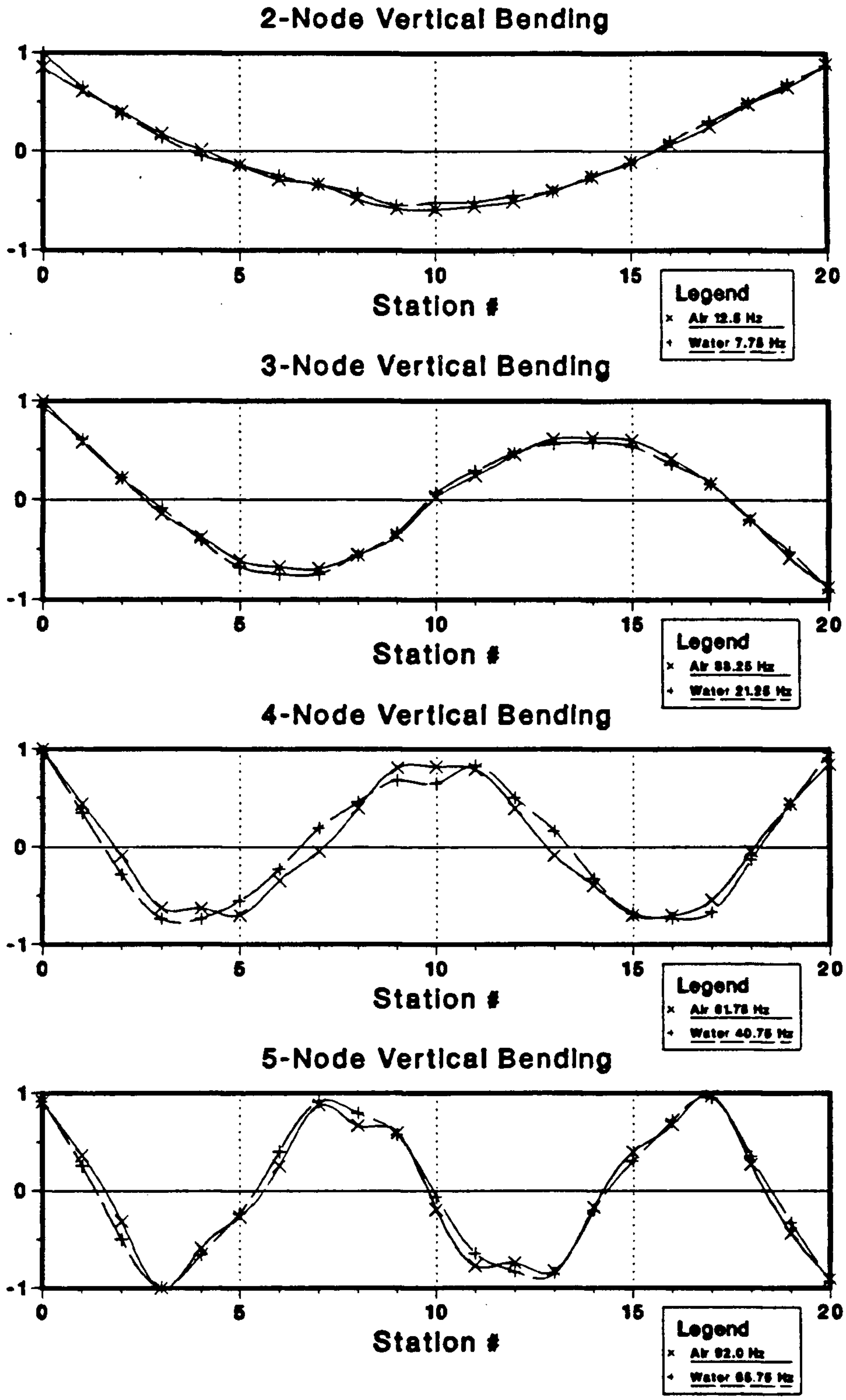

Figure 4.12 - Experimental Vertical Modes of the Ship Model in Air and Water for 30 lb Load Condition

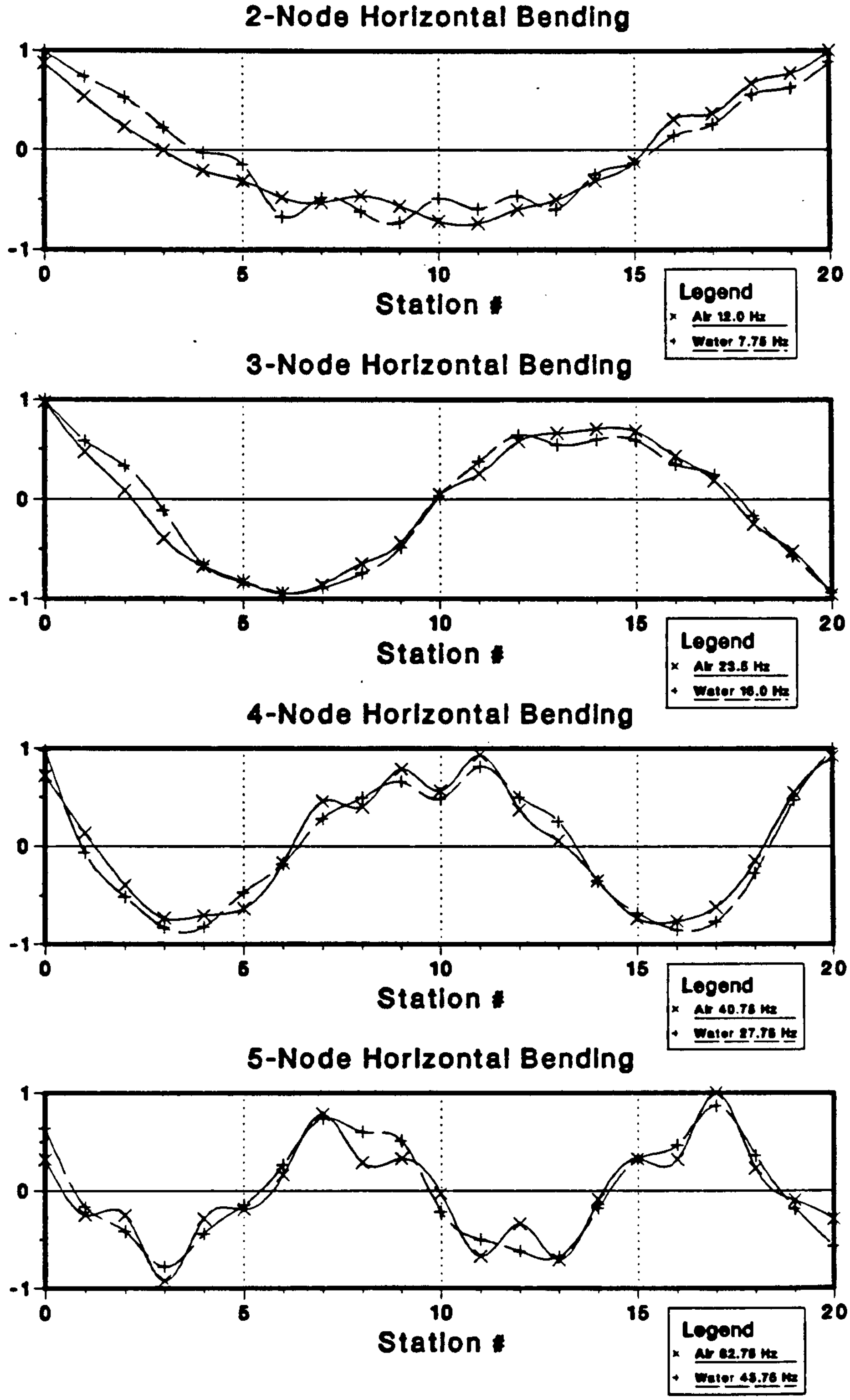

Figure 4.13 - Experimental Horizontal Modes of the Ship Model in Air and Water for 30 lb Load Condition

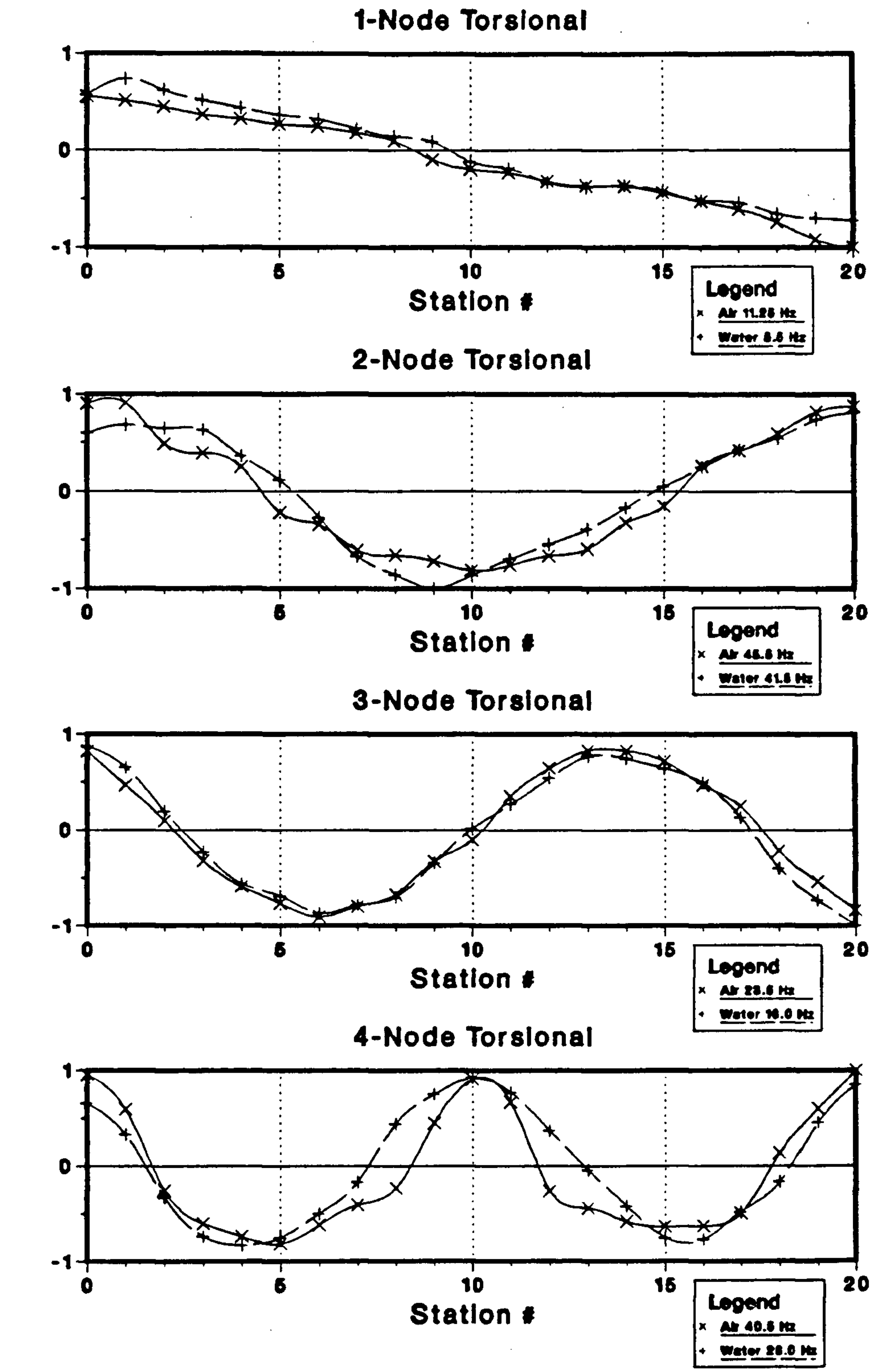

Figure 4.14 - Experimental Torsional Modes of the Ship Model in Air and Water for 30 lb Load Condition

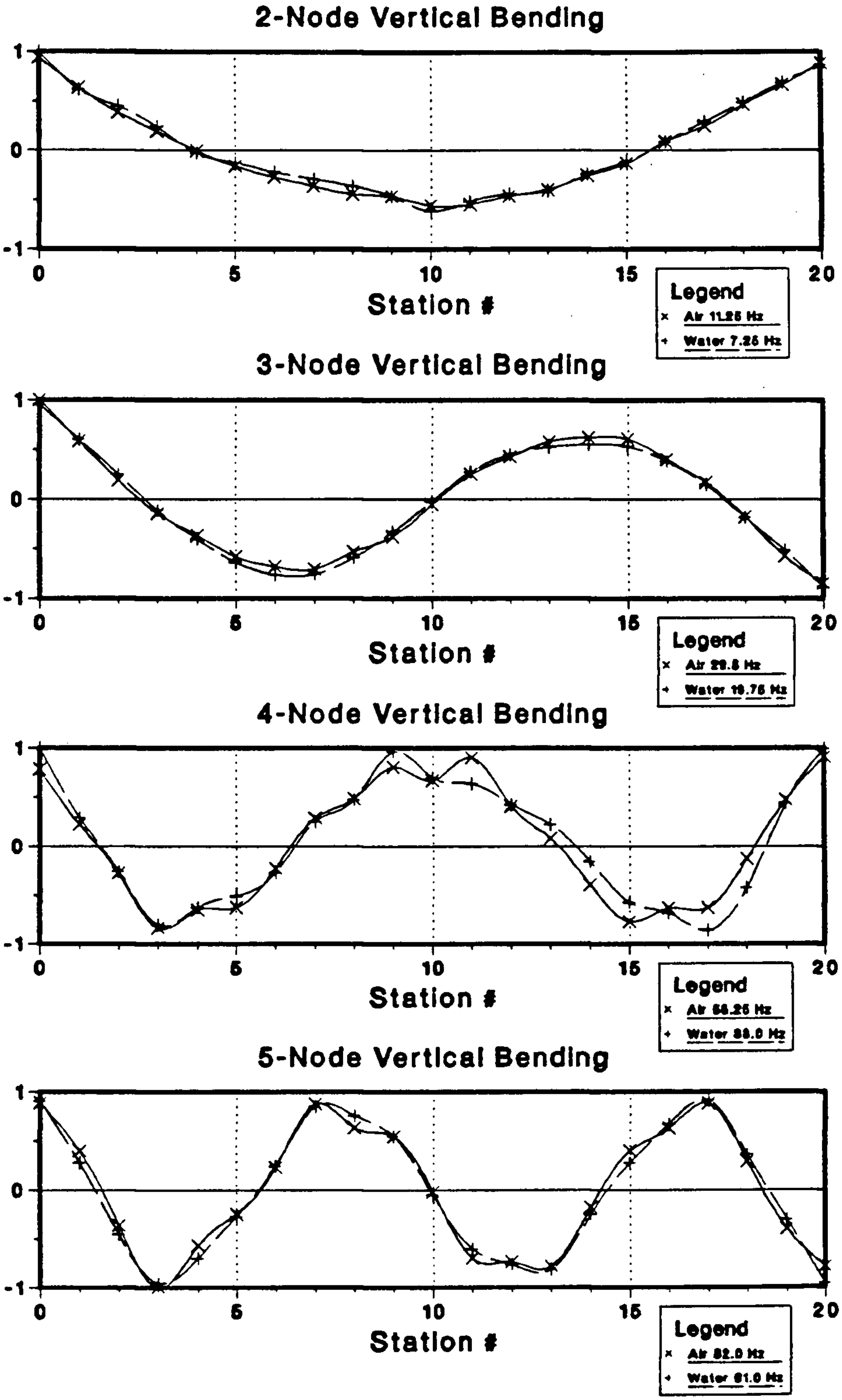

Figure 4.15 - Experimental Vertical Modes of the Ship Model in Air and Water for 40 lb Load Condition

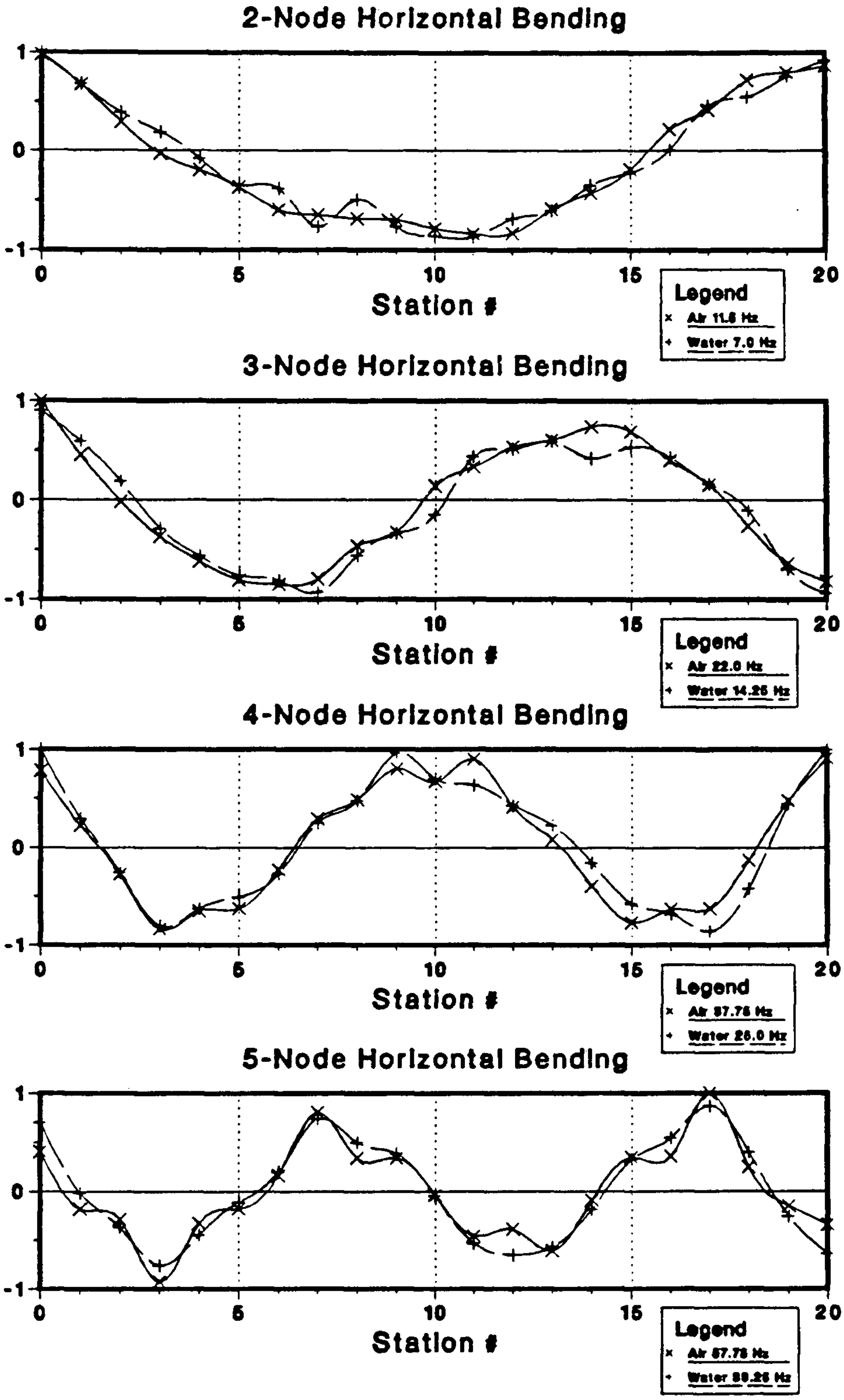

Figure 4.16 - Experimental Horizontal Modes of the Ship Model in Air and Water for 40 lb Load Condition

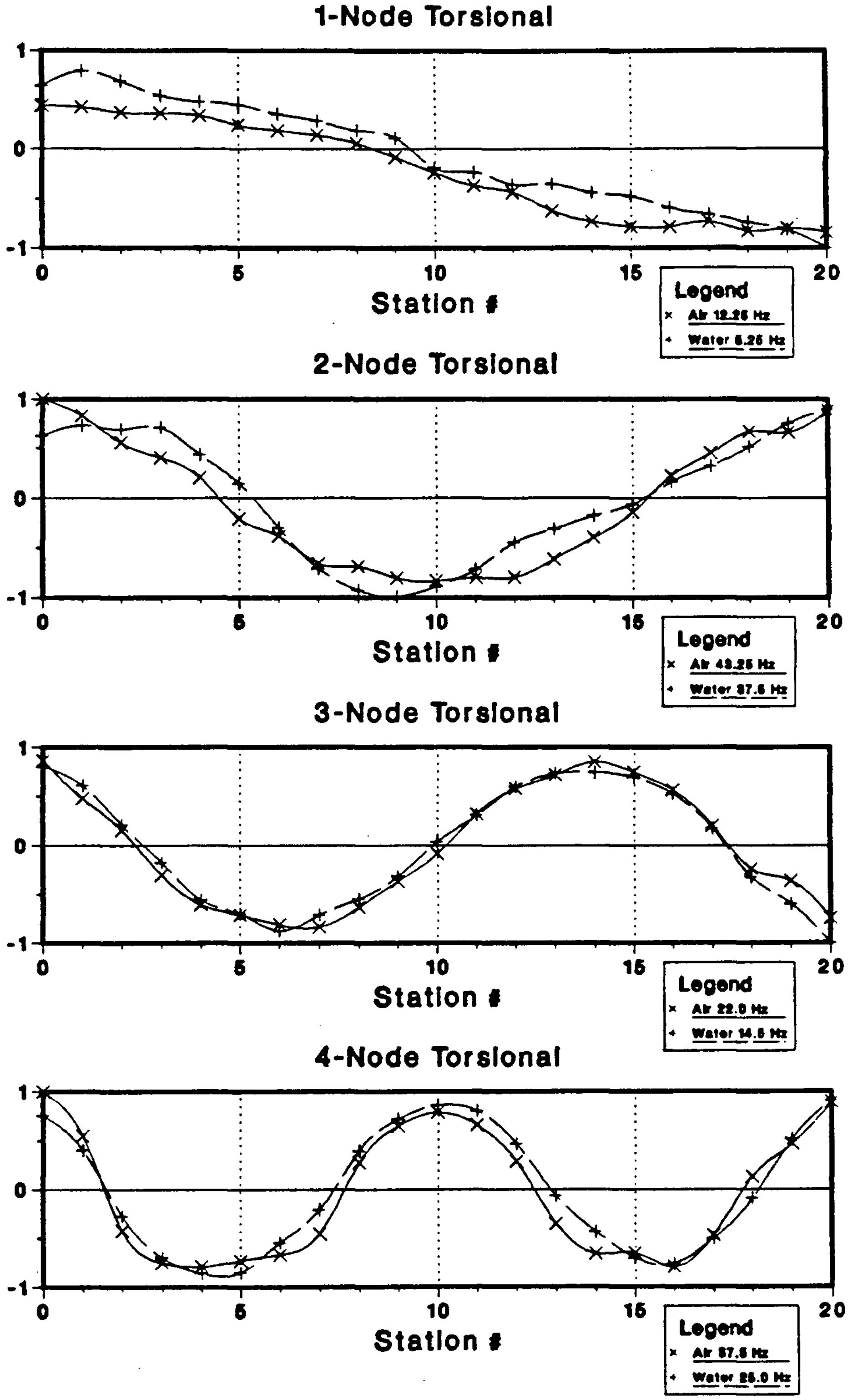

Figure 4.17 - Experimental Torsional Modes of the Ship Model in Air and Water for 40 lb Load Condition

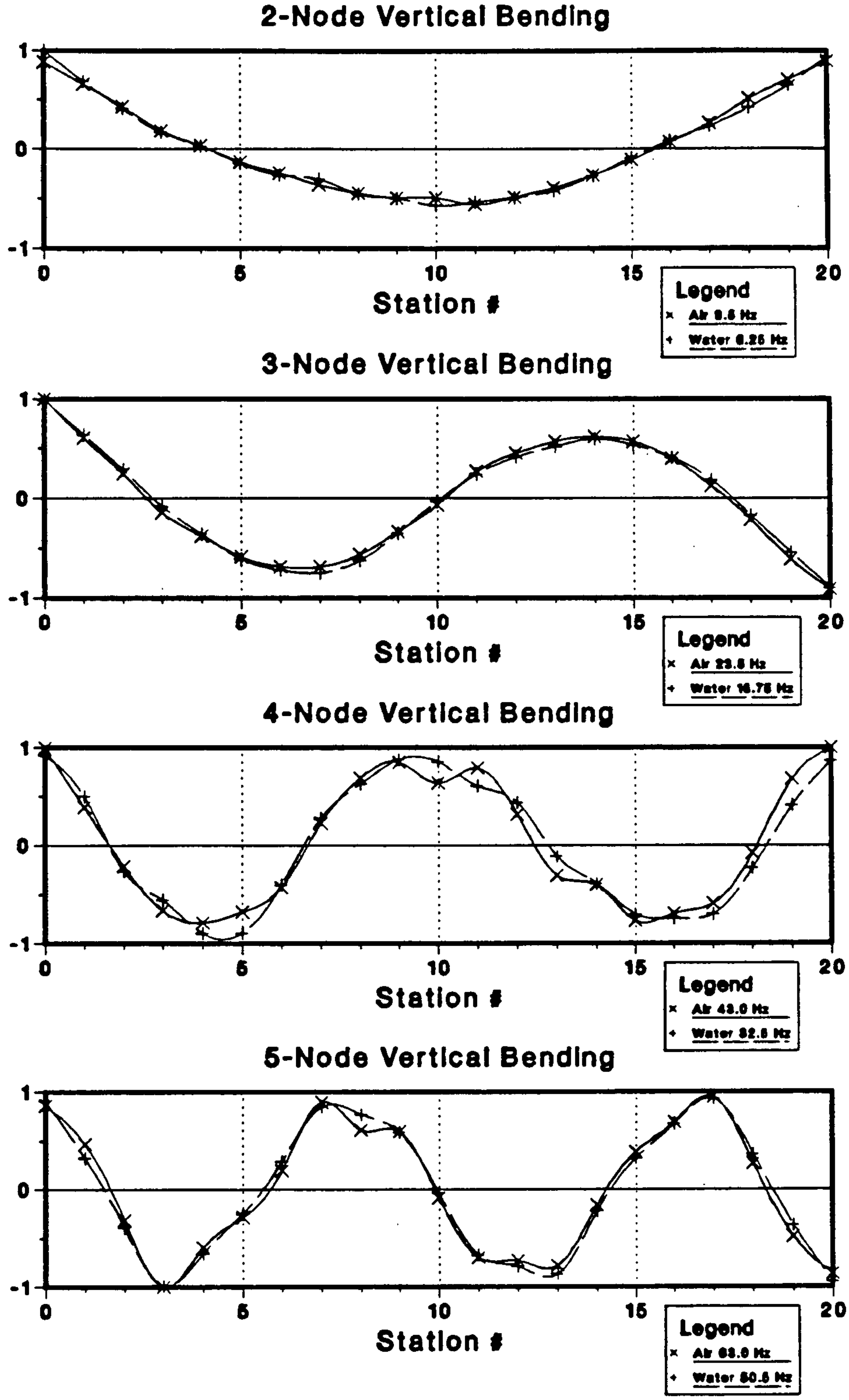

Figure 4.18 - Experimental Vertical Modes of the Ship Model in Air and Water for 70 lb Load Condition

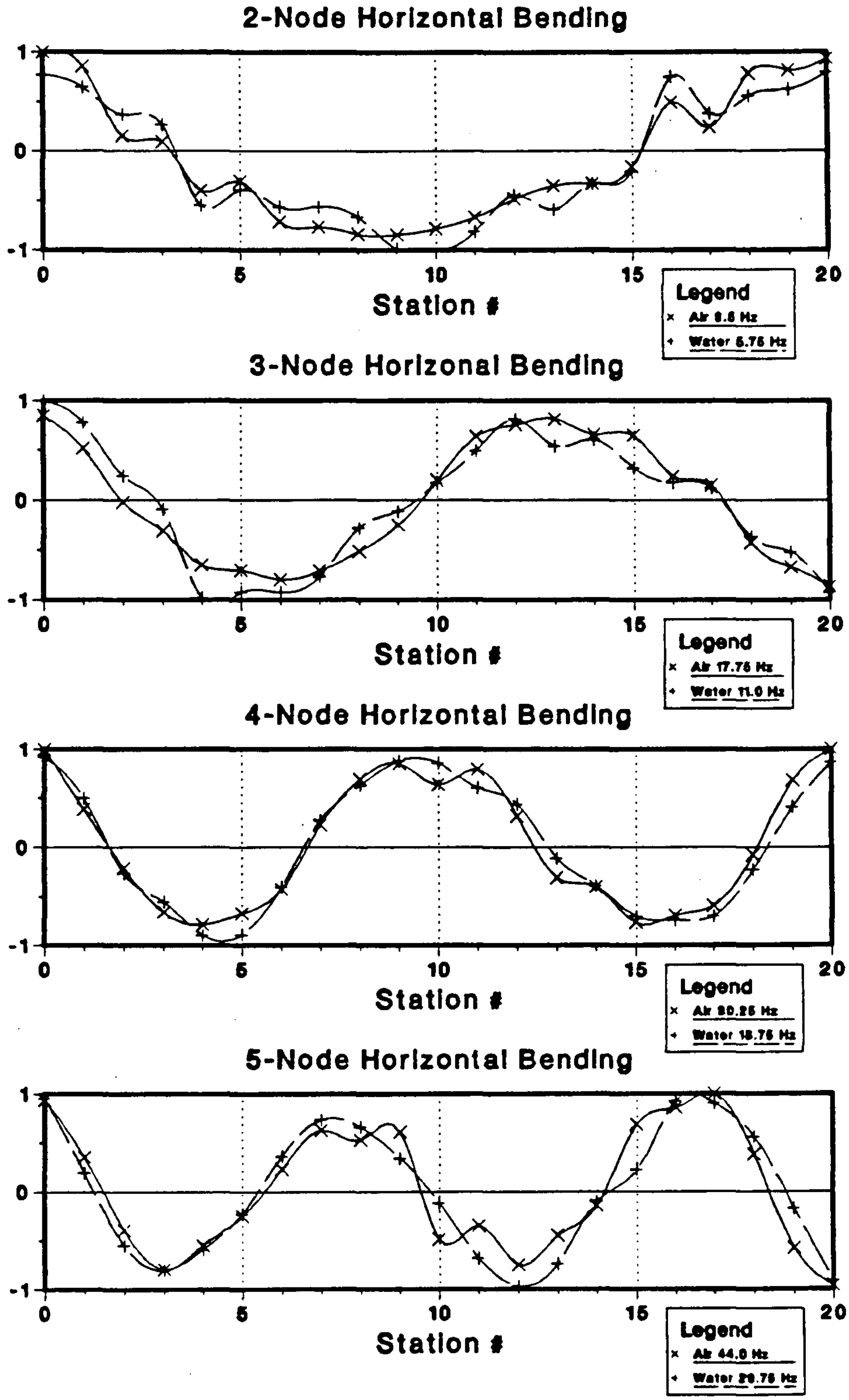

Figure 4.19 - Experimental Horizontal Modes of the Ship Model in Air and Water for 70 lb Load Condition

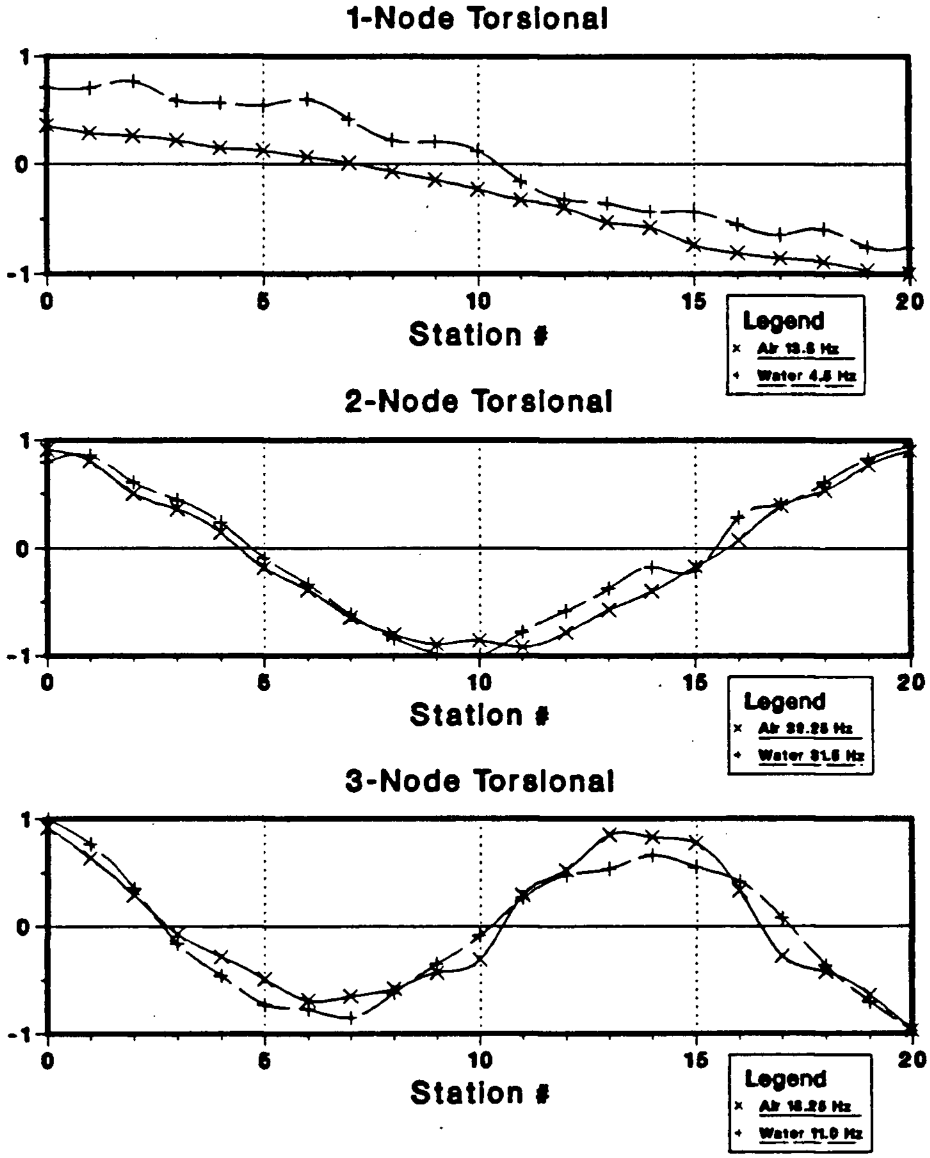

Figure 4.20 - Experimental Torsional Modes of the Ship Model in Air and Water for 70 lb Load Condition

18, and 20. By examining the modes that displayed local bending effects, it was seen that this local bending was occurring between these stations. Furthermore, as the load condition increased, the mode shapes became smoother and there were fewer local bending effects.

5. NUMERICAL RESULTS AND COMPARISON OF THE VIBRATION RESPONSE OF A SHIP MODEL IN AIR AND WATER

This chapter will describe the numerical work that was performed and will compare these results with the experimental results of the ship model. The numerical work included both structural modelling of the ship and fluid modelling of the surrounding water for the vibration characteristics of the ship model in air and water.

The ship finite element models were developed using a Mesh Generation Program that was written by the author. This program used the Thick/Thin Shell element (discussed in Appendix C) and allowed complex finite element meshes of the ship model to be created for use with VAST. These meshes were permitted to have any number of elements along the ship's length and around the ship's circumference, as long as the number of nodes in the structure did not exceed the maximum allowed by the VAST. The Mesh Generation Program required the load condition of the ship and then calculated the displacement of the ship from this information, proceeding to put only one element above the water line. The Mesh Generation Program also created the fluid mesh around the structure, using the 20-noded fluid elements (discussed in Appendix B), matching the structural and fluid meshes on the interface, and allowing the fluid domain to be extended radially out from the structure.

5.1 Material Properties

To use the Finite Element Program VAST, the properties of the material that was being modelled were required. These were determined through testing of the actual material of construction--acrylic--since the data supplied by the manufacturer only gave ranges for density ρ, Young's modulus E, and Poisson's ratio ν. (The intermediate results of these tests are presented in Appendix G.)

The density of the material was calculated by cutting a square section from the acrylic sheet that the model was made from, measuring it, and then weighing it accurately. The density of the acrylic was found to be $\rho = 0.000107\ \mathrm{lb.sec^2/in^4}$. (See Appendix G for details of the size and weight of the sample.)

Poisson's ratio was determined as $\upsilon = 0.368$. Young's modulus was a little more difficult to determine. Three different tests were performed. (They are summarized in Table 5.1.)

Test	Young's Modulus Psi
Strain Gauge	455,541
Finite Element	302,000
Dynamic	622,056

Table 5.1 - Results of Tests for Young's Modulus

The dynamic results for Young's modulus were used because these provided the best correlation with the experimental results.

5.2. Finite Element Models

The Finite Element Program VAST was used to determine the frequencies and mode shapes of vibration numerically. Finite element models of the structure and the fluid were made in order to compare the predicted vibration characteristics in air and water with the experimental results.

5.2.1. Structural Models

Trial meshes were generated using the Thick/Thin Shell element, and runs of VAST were executed to determine what degree of descretization was required in the structural model to obtain good results for the frequencies and mode shapes of vibration. It was found that 20 elements along the length, 8 elements around the circumference, and 21 bulkheads yielded good results. This mesh also corresponded well with the acrylic model of the ship, as there were twenty-one stations at which measurements were taken. This structural model had 3820 degrees of freedom and took an average of 3.5 hours of CPU time to solve for the first 20 modes of vibration, with 82 % of the time being spent in the eigenvalue solver. (Figure 5.1 shows the structural mesh that was used.)

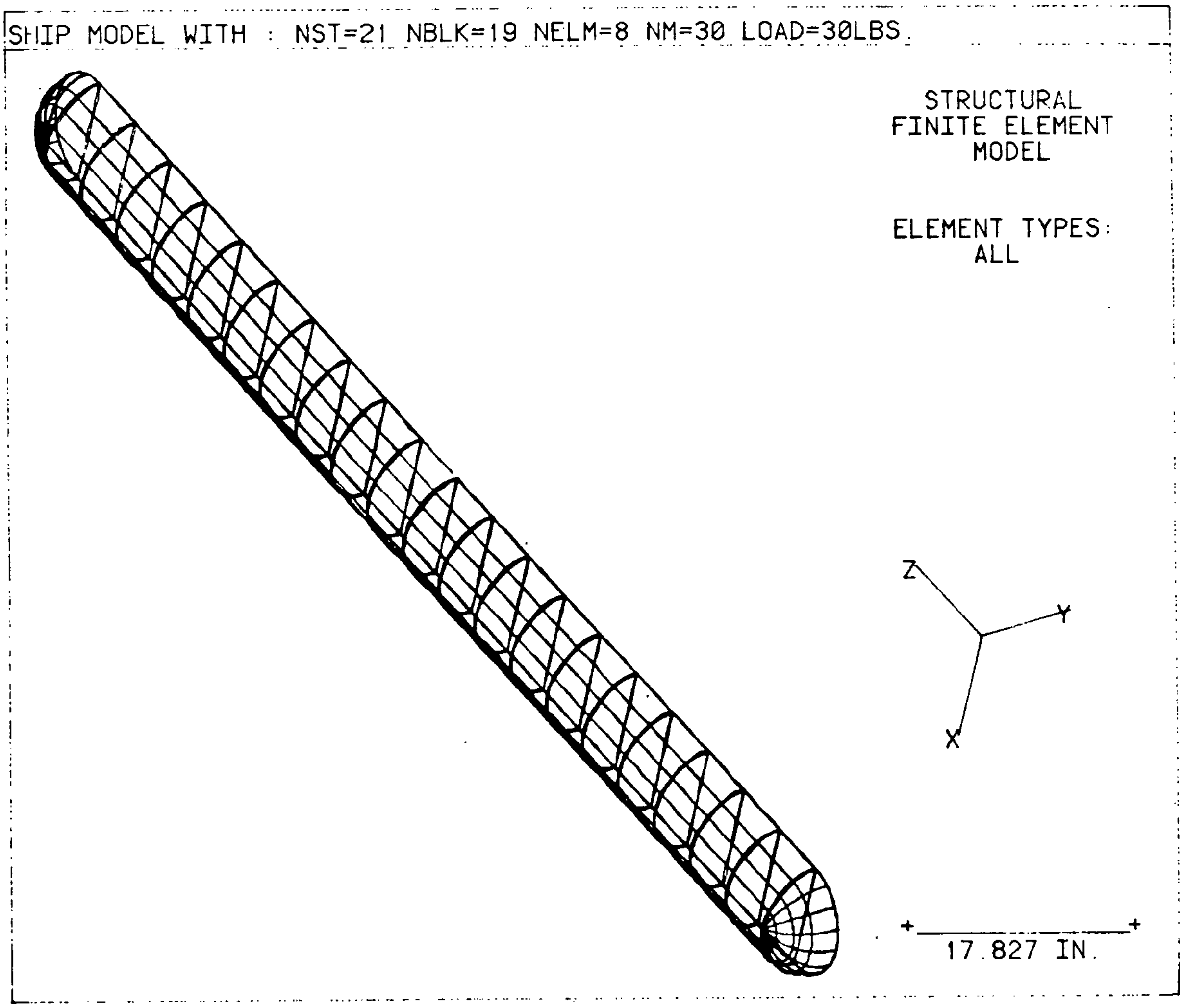

Figure 5.1 - Structural Finite Element Mesh of Ship Model

Elemental Matrix Formation	0.22hr	7%
Structural Matrix Assembly	0.14hr	4%
Matrix Decomposition	0.27hr	8%
Eigenvalue Analysis	2.63hr	81%
Fluid Matrix Formulation	–	–
Total CPU	3.27hr	

Table 5.2 - Average CPU Times for Structural Mesh

During the trial runs, it was noted that the results did not always improve with an increase in the number of degrees of freedom. It was very easy to create a model that had mainly local vibration modes and very few global modes; however, the local modes were not wanted. It was found that introducing bulkheads every few elements removed these local modes and had little effect on the global frequencies. If the numerical model had very few bulkheads, the only global mode that could be identified was the 2-node vertical mode; all the other modes were local or complex horizontal-torsional coupled modes. (See Figure 5.2.)

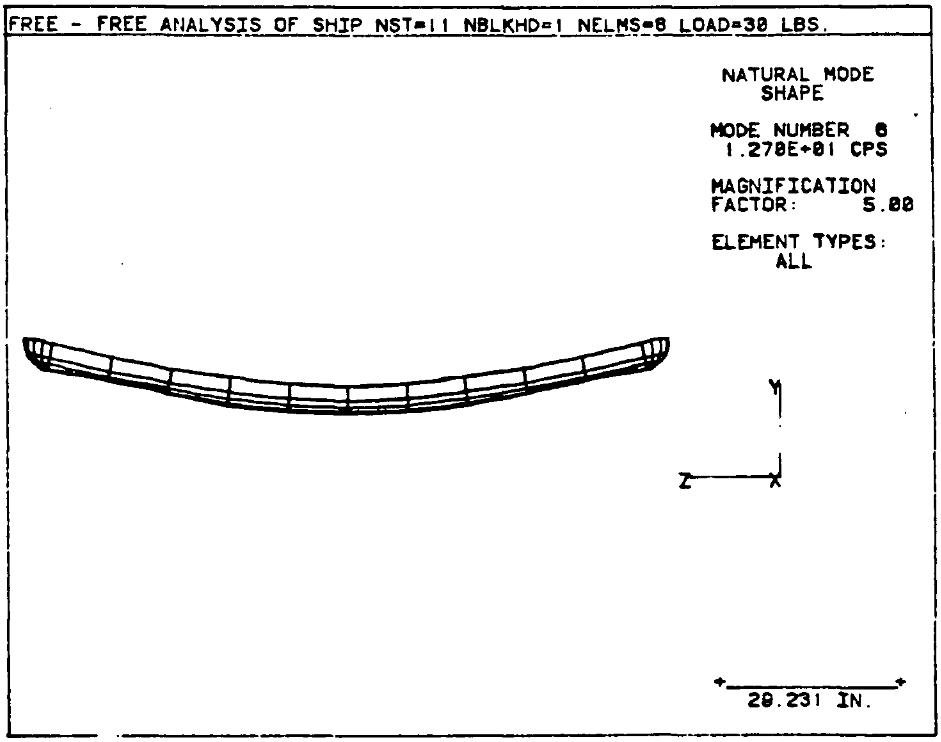

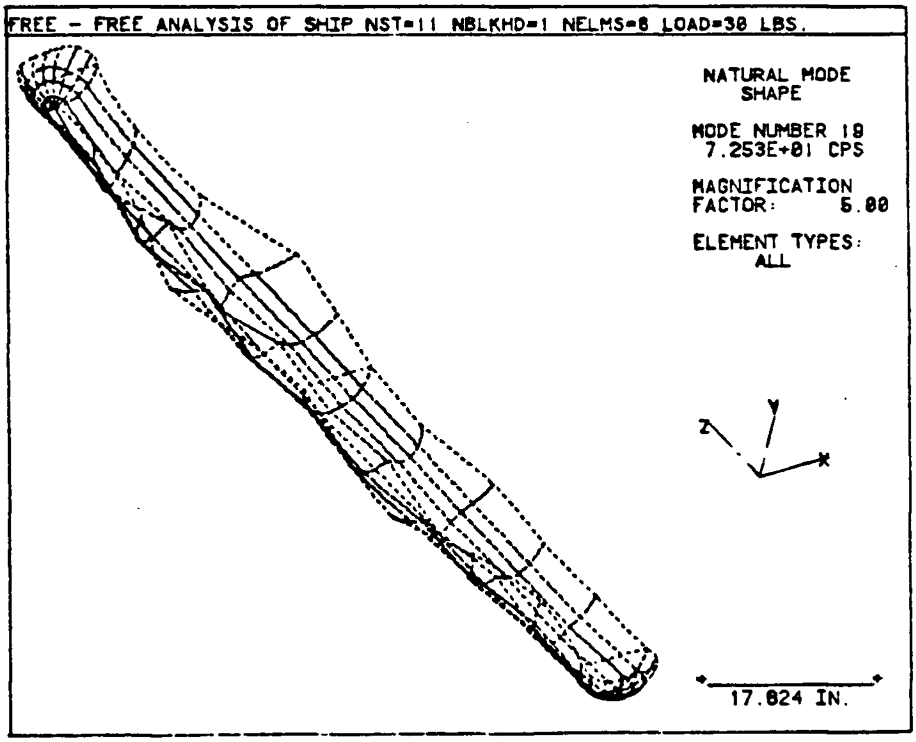

Figure 5.2 - Various Mode Shapes

5.2.2. Fluid Meshes

Two idealizations of the fluid were used. (See Figure 5.3.) The first mesh used two 20-noded fluid elements in the radial direction; the other used three 20-noded fluid elements. Both of these meshes gave very similar results and used about the same CPU time (as shown in Table 5.3), although the two element mesh had 1220 degrees of freedom and the three element mesh had 1830 degrees of freedom. However, there were modifications to some of the parameters of the computer between running the two element fluid mesh and the three element fluid mesh, and these modifications affected the CPU times.

The reason that the fluid-structure problem took so much more time than the structure alone was the fact that the added mass matrix was almost completely full. When this matrix was added to the structural mass matrix, which was nicely banded, the banding was lost and the program had to deal with a matrix that had a bandwidth on the order of the number of degrees of freedom in the fluid-structure interface. The size of the structural mass matrix $[M_S]$ was 3820, but it only had a bandwidth of 165; however, when the added mass matrix $[M_A]$ was added to the structural mass matrix $[M_S]$ the bandwidth was increased to 1389.

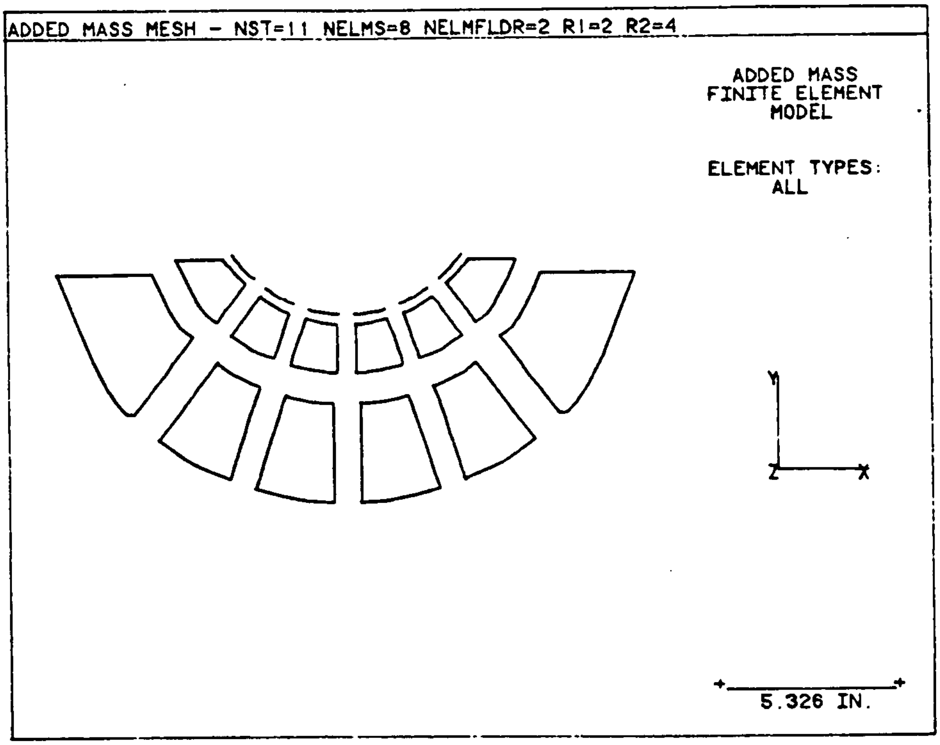

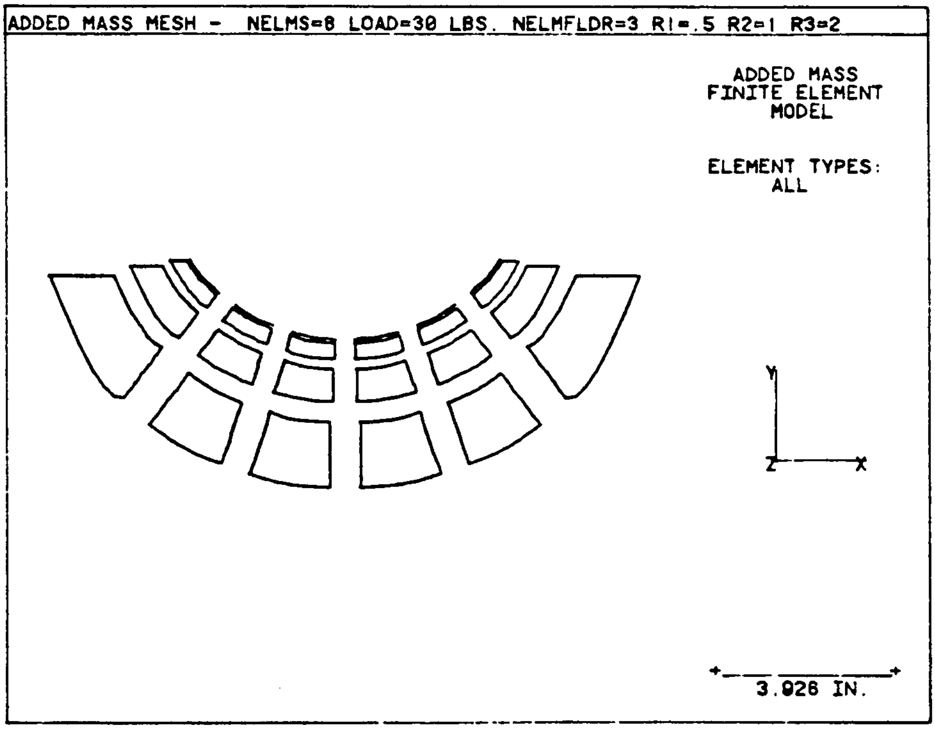

Figure 5.3 - Fluid Meshes

	2 Fluid		3 Fluid	
Elemental Matrix Formation	817	-	778	-
Structural Matrix Assembly	1741	1%	1324	1%
Matrix Decomposition	86551	34%	86411	38%
Eigenvalue Analysis	67129	27%	55604	25%
Fluid Matrix Formulation	94881	38%	81590	36%
Total CPU	69.7hr		62.7hr	

Table 5.3 - CPU Time for Fluid Meshes

The finite element models of the structure and the fluid consumed large amounts of computer resources. Each run took between 63 and 70 hours of CPU time and used 575,000 blocks of disk space on the Department of Mechanical Engineering's VAX 11/750 computer. The harddisk on the VAX was only a 700,000 block disk.

5.3. Results and Comparison With The Experimental Results

In this section, the frequencies and mode shapes predicted by the various numerical methods will be compared with the experimental results of the air and water tests. In general, there was good agreement with the vertical modes of vibration and varying degrees of success with the horizontal and torsional modes.

5.3.1. Frequencies

The results for the frequencies predicted by the various numerical methods were compared with the experimental results of vibration. Two different methods were used to model the effect of the fluid on the vibration characteristics of the model. The first used Strip and Beam Theory to calculate the frequencies of vibration, while the second used the Finite Element Program VAST to determine the frequencies and mode shapes.

5.3.1.1. Beam/Strip Theory and Experimental Results

The results for the vertical vibration characteristics of the model were easy to calculate using Beam Theory (and were presented in Chapter 4). The results from Strip Theory were also very simple to calculate, since the model had a constant cross-section over its length. However, only the results of the vertical modes could be determined using this method. (The results are presented in Table 5.4.) The lewis C factor for this hull shape was 1 and was approximately the same for the 5 draughts considered. The J-factors that corrected for the three-dimensional flow were : 0.836, 0.793, 0.771, and 0.756 for the 2, 3, 4, and 5-node vertical bending modes respectivily. Thus, it was seen by comparing these numbers with the ratios of added mass to structural mass for the veritcal bending modes (from Table 4.9 or 4.10) that this method was going to underestimate the added mass of the fluid.

		2-Node		3-Node		4-Node		5-Node	
Load cond.		Air	H_2O	Air	H_2O	Air	H_2O	Air	H_2O
30lb	EXP	12.5	7.75	33.25	21.25	61.75	40.75	92.0	65.75
	B/S	12.98	9.58	35.78	26.72	70.15	52.71	115.9	87.59
40lb	EXP	11.25	7.25	29.5	19.75	55.25	38.0	82.0	61.0
	B/S	11.47	8.46	31.61	23.61	61.97	46.57	102.4	77.39
50lb	EXP	10.5	7.0	27.25	18.5	50.5	35.5	74.5	56.75
	B/S	10.39	7.67	28.63	21.38	56.12	42.17	92.77	70.1
60lb	EXP	10.0	6.5	25.25	17.75	46.75	33.75	67.75	53.25
	B/S	9.56	7.06	26.35	19.68	51.66	38.82	85.4	64.54
70lb	EXP	9.5	6.25	23.5	16.75	43.0	32.5	63.0	50.5
	B/S	8.91	6.57	24.55	18.33	48.12	36.16	79.55	60.12

Table 5.4 - Frequencies for the Vertical Bending Modes from Beam and Strip Theory

Strip Theory and experimental results for the vertical modes of vibration (see Figure 5.4 and 5.5) were quite good for the 2-node vertical mode; but, as the complexity of the modes increased the results began to deteriorate. This deterioration occured because this method did not account for shear deflections and rotary inertia, although these items might have been included in the analysis discussed by Bishop and Price [9-13]. It should also be noted that Strip Theory was able to predict the added mass for pure horizontal modes, but said nothing when there was coupling with torsional modes.

5.3.1.2. Finite Element and Experimental Results

The frequencies determined in the experiment were compared with the finite element results. (Tables 5.5 - 5.7 list the frequencies predicted by VAST and found experimentally.) The finite element results were only run in water for the 30 and 40 lb load conditions. As well, the 5-node horizontal, the 1-node torsional, and the 2-node torsional could not be identified from the finite element results. Finite Element water runs were not performed for the 50, 60, and 70 lb load conditions. As well,

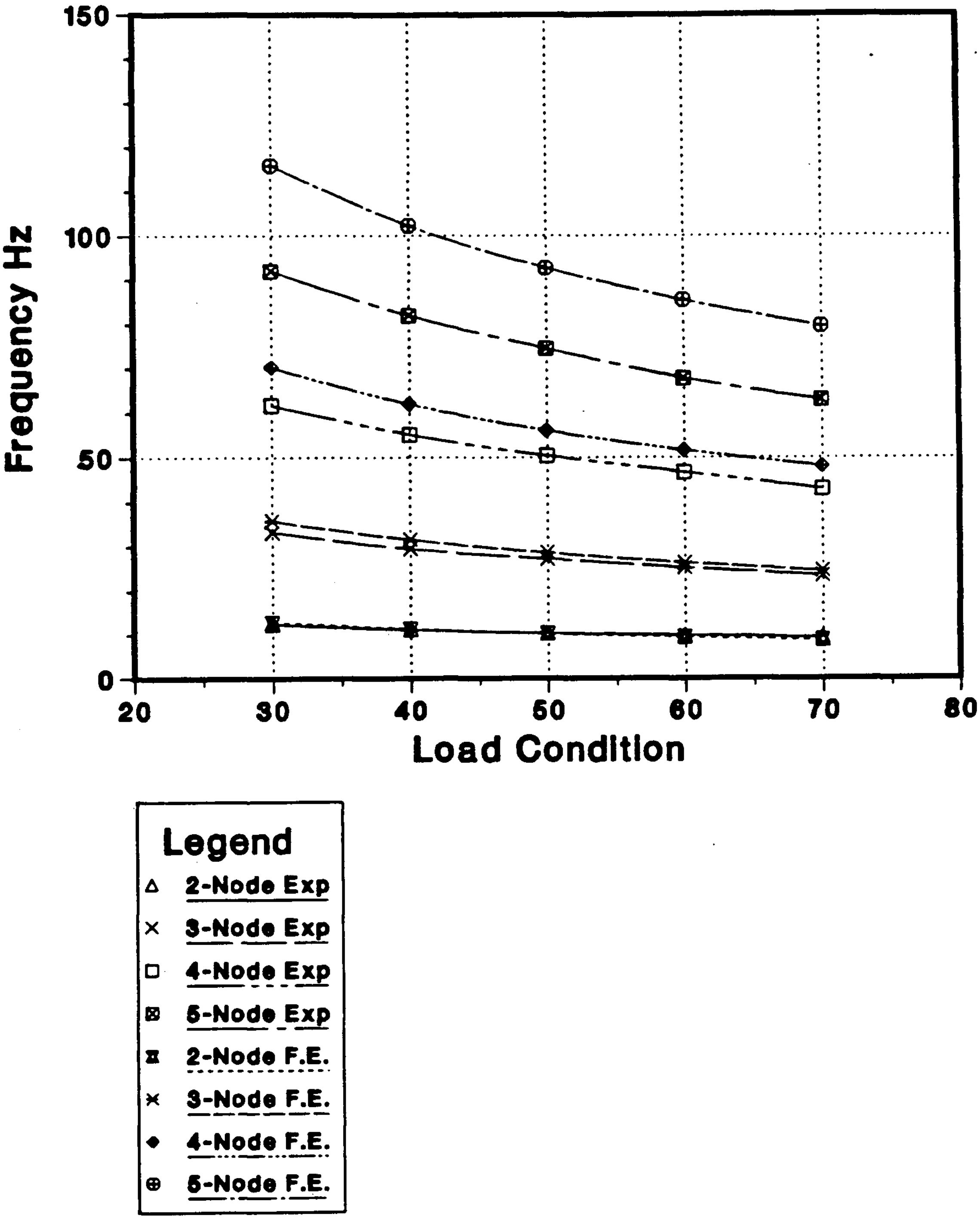

Figure 5.4 - Experimental and Beam Theory Results in Air

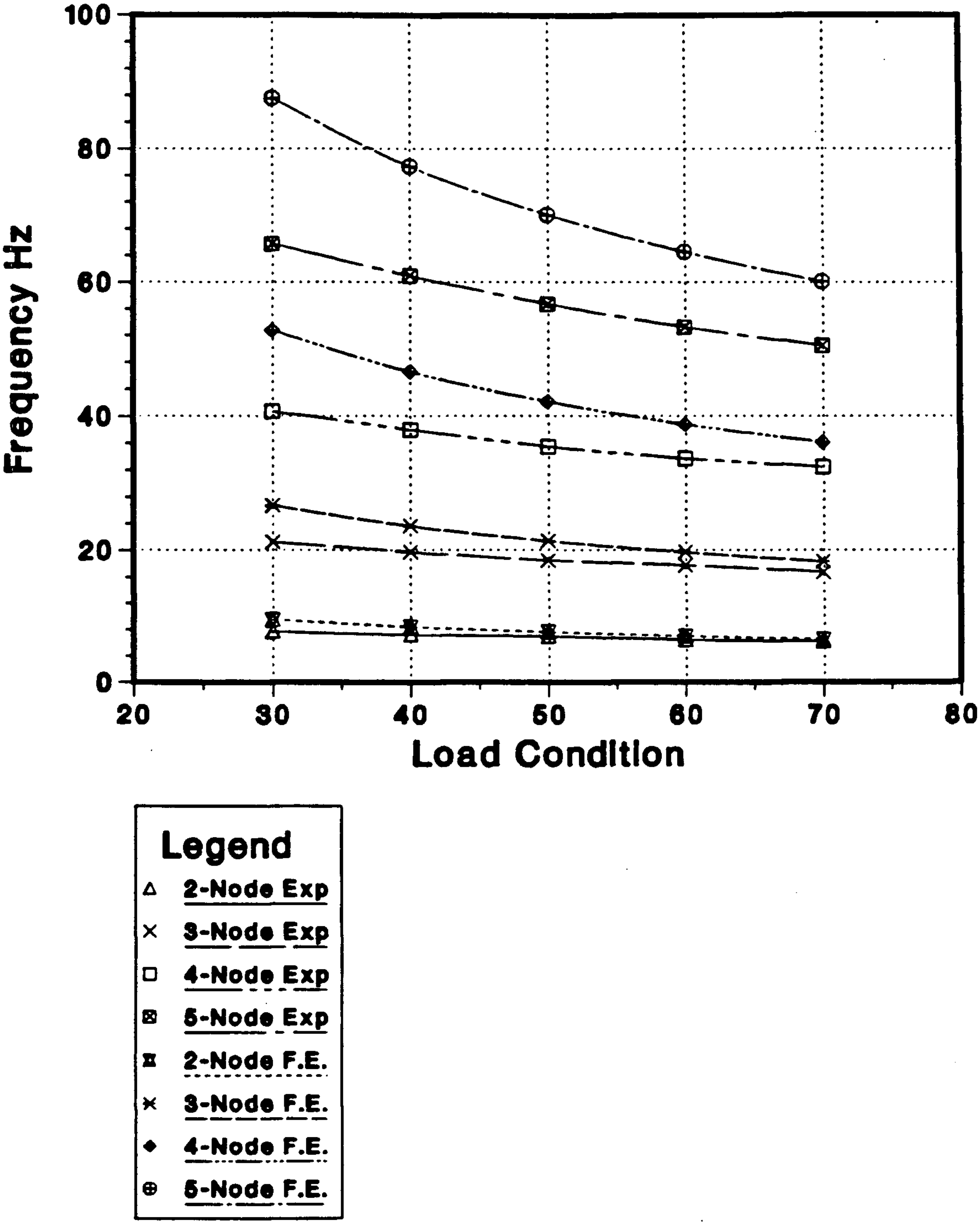

Figure 5.5 - Experimental and Strip Theory Results in Water

some modes that were identified in the experiment were not identified from the finite element results. Thus, some places were omitted.

		2-Node		3-Node		4-Node		5-Node	
Load cond.		Air	H_2O	Air	H_2O	Air	H_2O	Air	H_2O
30lb	EXP	12.5	7.75	33.25	21.25	61.75	40.75	92.0	65.75
	FE	12.11	7.78	32.34	21.03	60.88	40.25	95.31	64.89
40lb	EXP	11.25	7.25	29.5	19.75	55.25	38.0	82.0	61.0
	FE	10.93	7.25	29.24	19.61	55.03	37.51	86.03	60.18
50lb	EXP	10.5	7.0	27.25	18.5	50.5	35.5	74.5	56.75
	FE	10.04	-	26.90	-	50.69	-	79.36	-
60lb	EXP	10.0	6.5	25.25	17.75	46.75	33.75	67.75	53.25
	FE	9.34	-	25.03	-	47.21	-	74.06	-
70lb	EXP	9.5	6.25	23.5	16.75	43.0	32.5	63.0	50.5
	FE	8.84	-	23.63	-	44.52	-	69.56	-

Table 5.5 - Frequencies for the Vertical Bending Modes from Finite Element

		2-Node		3-Node		4-Node		5-Node	
Load cond.		Air	H_2O	Air	H_2O	Air	H_2O	Air	H_2O
30lb	EXP	12.0	7.75	23.5	16.0	40.75	27.75	62.75	43.75
	FE	12.11	7.78	49.23	34.41	59.94	42.63	-	-
40lb	EXP	11.5	7.0	22.0	14.25	37.75	25.0	57.75	39.25
	FE	10.93	7.25	49.22	32.0	59.98	39.47	-	-
50lb	EXP	10.75	6.5	20.5	13.0	35.25	22.75	52.25	35.5
	FE	10.04	-	49.28	-	60.29	-	-	-
60lb	EXP	10.25	6.75	18.75	12.0	33.0	20.5	48.25	32.25
	FE	9.34	-	49.45	-	60.85	-	-	-
70lb	EXP	9.5	5.75	17.75	11.0	30.25	18.75	44.0	29.75
	FE	8.84	-	50.21	-	63.87	-	-	-

Table 5.6 - Frequencies for the Horizontal Bending Modes from Finite Element

		1-Node		2-Node		3-Node		4-Node	
Load cond.		Air	H_2O	Air	H_2O	Air	H_2O	Air	H_2O
30lb	EXP	11.25	5.5	45.5	41.5	23.5	16.0	40.5	28.0
	FE	-	-	-	-	49.23	34.41	59.94	42.63
40lb	EXP	12.25	5.25	43.25	37.5	22.0	14.5	37.5	25.0
	FE	-	-	-	-	49.22	32.0	59.98	39.47
50lb	EXP	12.75	5.25	-	-	20.75	13.0	34.75	22.5
	FE	-	-	-	-	49.28	-	60.29	-
60lb	EXP	13.5	6.0	-	-	19.5	12.0	32.75	20.75
	FE	-	-	-	-	49.45	-	60.85	-
70lb	EXP	13.5	4.5	39.25	31.5	18.25	11.0	-	-
	FE	-	-	-	-	50.21	-	63.87	-

Table 5.7 - Frequencies for the Torsional Modes from Finite Element

There was very good agreement between the experimental and finite element model for the vertical vibration modes of the structures both in air and water. However, there was no agreement between the experimental and finite element results for the frequencies of the coupled horizontal-torsional modes.

One reason that the frequencies were different for the horizontal-torsional coupled modes was that in the finite element model the weights were modelled as lumped masses, and they were located on the centerline of the structure. Thus, the center of mass for the finite element model and the actual structure did not correspond. As well, this modelling did not account for the distribution of the mass that occurred in the real model. These effects only showed up in the horizontal and torsional modes of vibration.

It was seen (in Tables 5.6 and 5.7) that the frequencies for the 3 and 4-node horizontal-torsional coupled modes in air did not change as the load condition increased; however, they did change in water. From these results it was concluded that the mass modelling of the load conditions was not adequate.

In order to produce better agreement between the horizontal and torsional modes, the finite element representation of the weights was improved. In this new model the weights were represented using a Thick/Thin Shell element that had no stiffness but was the correct height and weight to model the 30 lb load condition. (This model is shown in Figure 5.6 and the results are tabulated in Table 5.8.) Unfortunately, this new modelling did not improve the frequency predictions of VAST substantially.

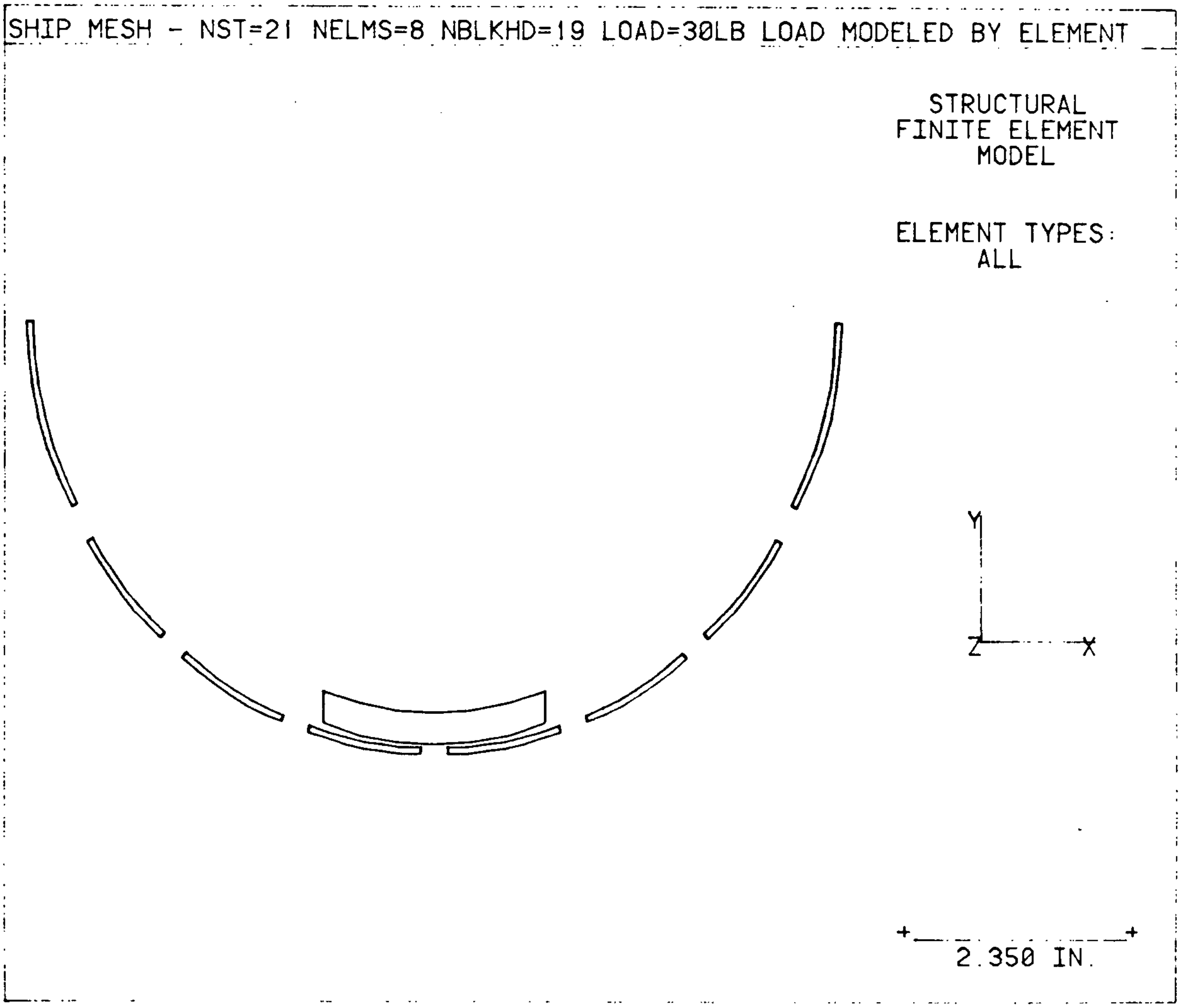

Figure 5.6 - Finite Element Weight Modelling

Mode	EXP	OLD FE	NEW FE
2NDV/2NDH	12.5	12.11	11.56
3NDH/3NDT	23.5	49.23	40.27
3NDV	33.25	32.34	30.84
4NDH/4NDT	40.75	59.94	57.34
4NDV	60.75	60.88	58.01
5NDV	92.0	95.31	-

Table 5.8 - Frequencies Predicted by Both Finite Element Models of the Weights for 30 lb Load Condition

This poor prediction of the horizontal-torsional coupled modes seemed to be a deficiency in the finite element's representation of the structure. The effects that are present in the real structure are : shear deflection, shear flow, rotary inertia, and warping. This finite element accounted for the shear deflection and the rotary inertia effects, but it was unable to model the shear flow and warping effects that occur in the real structure.

5.3.2. Mode Shapes

The Finite Element Method was able to predict the mode shapes of vibration for the ship model. First, the mode shapes in air and water from the finite element results were compared for their similarity; then, the finite element mode shapes were compared with the experimental mode shapes for the air and water results.

The mode shapes in air and water for the 30 and 40 lb load conditions predicted by the Finite Element Method (see Figure 5.7 - 5.12) were examined. As with the experimental mode shapes, there was little difference between the mode shapes in air and those in water for the vertical modes. However, the horizontal and torsional modes were affected by the water, and their shape was changed considerably. This effect can be explained. Since the added mass matrix was added to the structural mass matrix, the nodes on the fluid-structure interface acquired mass, which affected the distribution of mass in the finite element model. This addition changed the distribution of mass in the structure, thus changing the mode shape. The mode shape of the horizontal and torsional modes was closer to the experimental mode shape, since the mass distribution was closer to the actual.

Local bending did not come into play in the finite element mode shapes, since the model was developed to limit this effect. If more degrees of freedom had been used in the regions

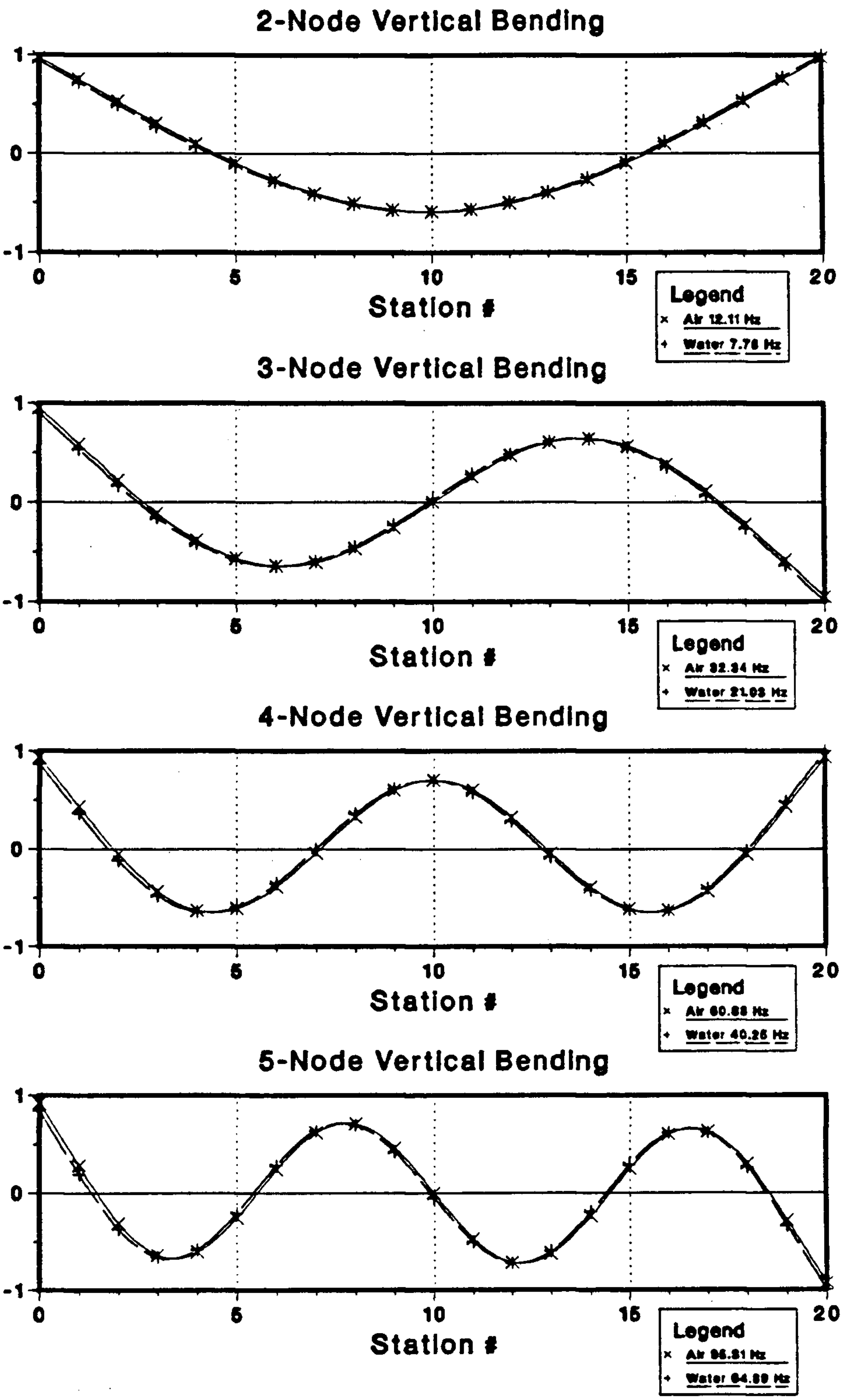

Figure 5.7 - Finite Element Vertical Modes of the Ship Model in Vacuum and Water for 30 lb Load Condition

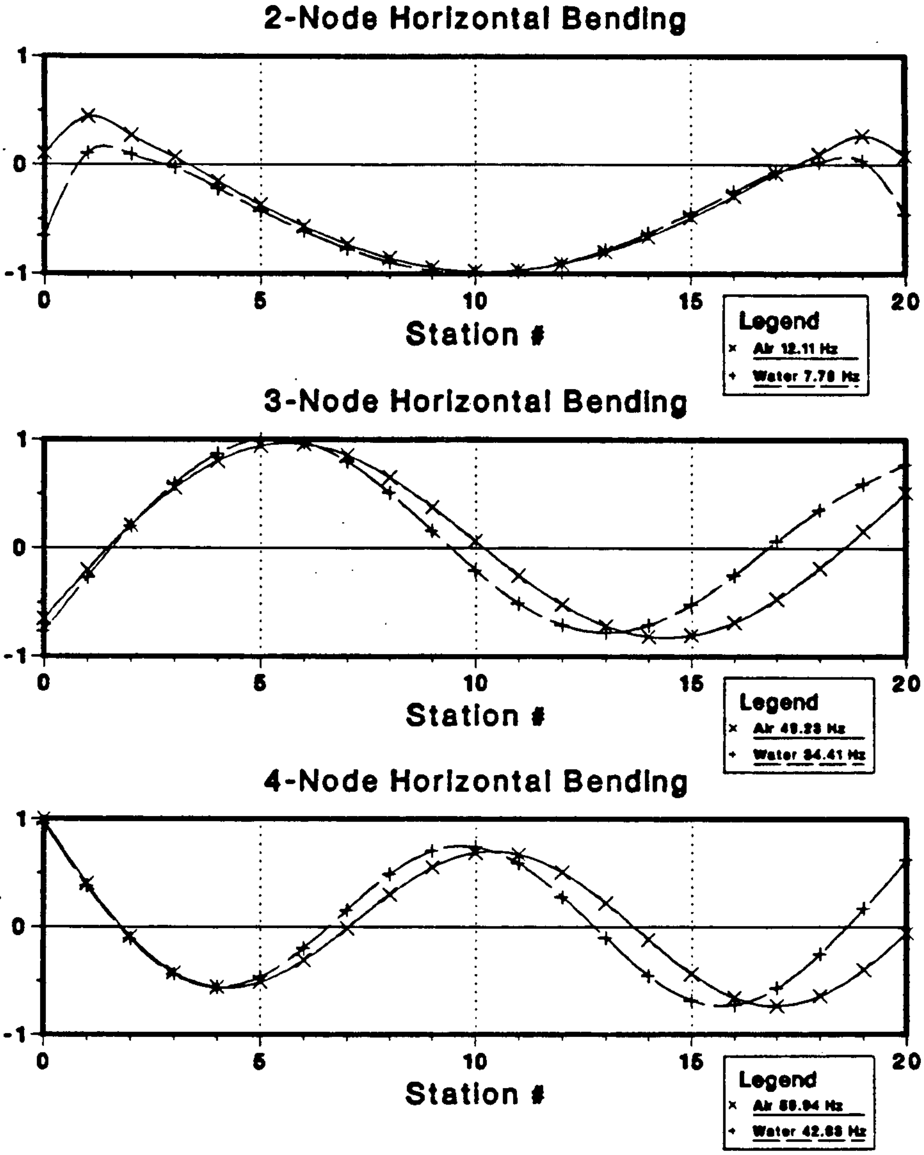

Figure 5.8 - Finite Element Horizontal Modes of the Ship Model in Vacuum and Water for 30 lb Load Condition

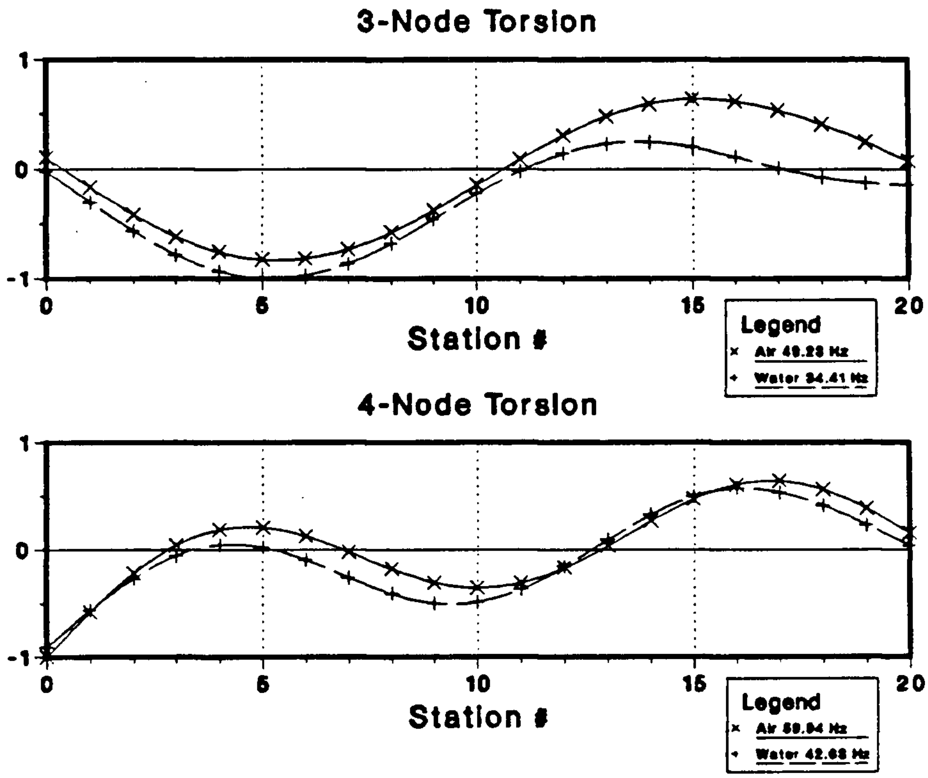

Figure 5.9 - Finite Element Torsional Modes
of the Ship Model in Vacuum and
Water for 30 lb Load Condition

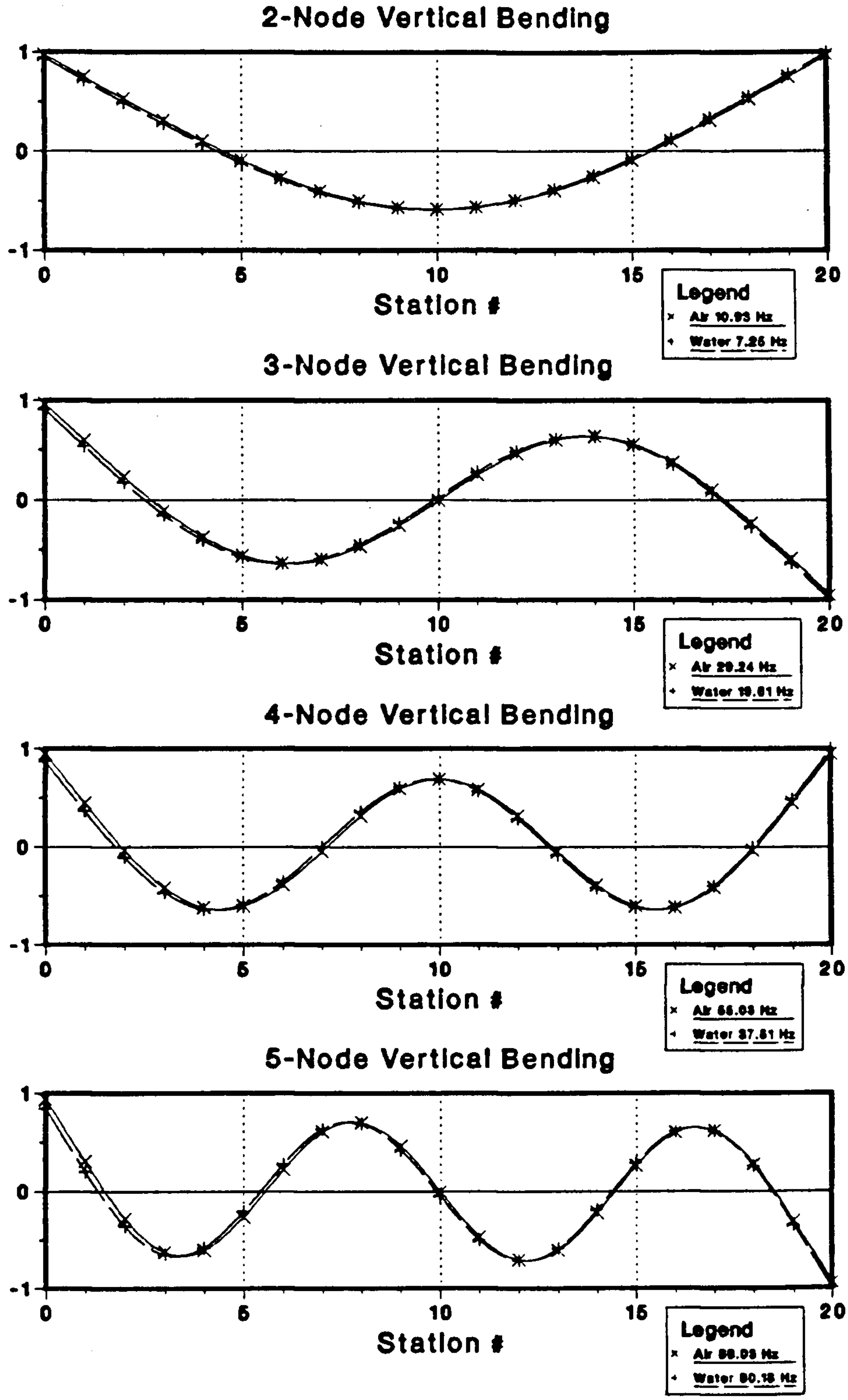

Figure 5.10 - Finite Element Vertical Modes of the Ship Model in Vacuum and Water for 40 lb Load Condition

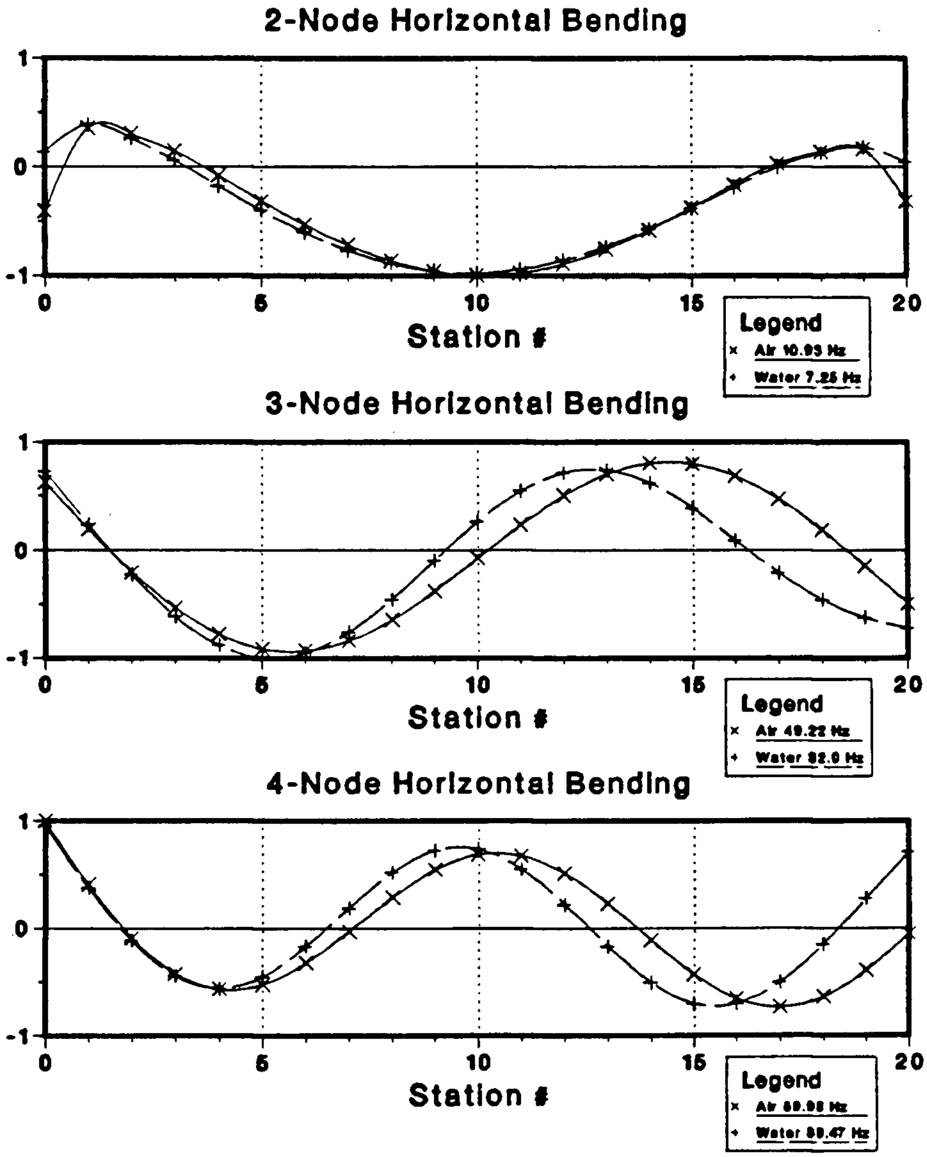

Figure 5.11 - Finite Element Horizontal Modes of the Ship Model in Vacuum and Water for 40 lb Load Condition

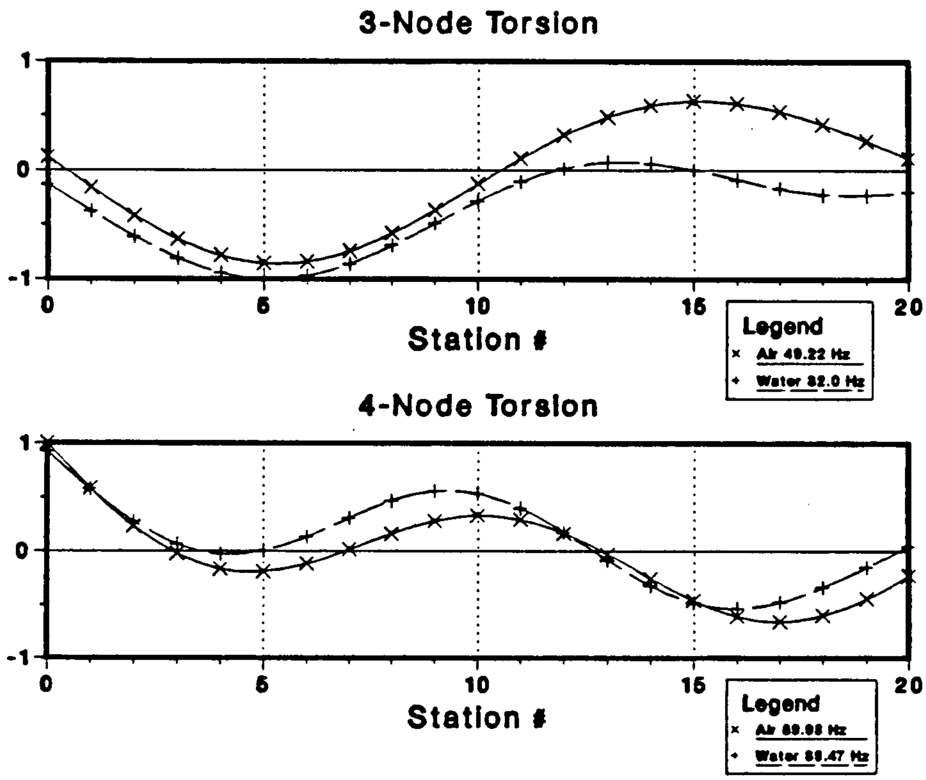

Figure 5.12 - Finite Element Torsional Modes of the Ship Model in Vacuum and Water for 40 lb Load Condition

between the bulkheads, local bending would also have been present in the finite element model.

The mode shapes in air for the 30, 40 and 70 lb load conditions predicted by VAST were compared with the experimental mode shapes. (See Figure 5.13 - 5.21.) In general, there was good agreement between the mode shapes for the vertical modes of vibration. However, as with the frequencies, there was poor agreement with the horizontal and torsional mode shapes. This was due in part to reasons explained above.

The mode shapes in water for the 30 and 40 lb load condtions predicted by VAST were compared with the experimental mode shapes. (See Figures 5.22 - 5.27.) The vertical mode shapes were very similar, but the horizontal and torsional modes shapes were not. However, the horizontal and torsional mode shapes were closer in water than they were in air.

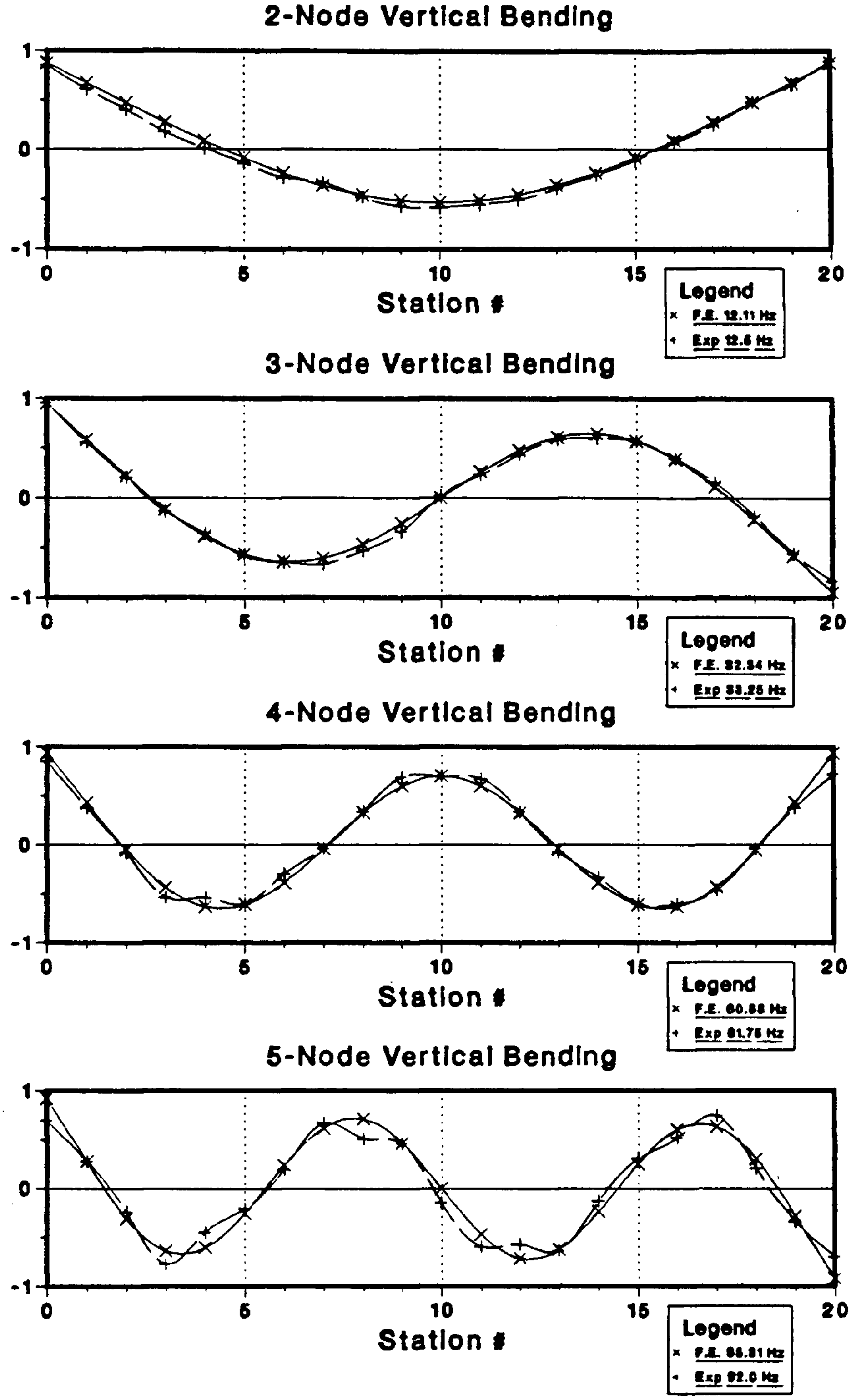

Figure 5.13 - Finite Element and Experimental Vertical Modes of the Ship Model Air for 30 lb Load Condition

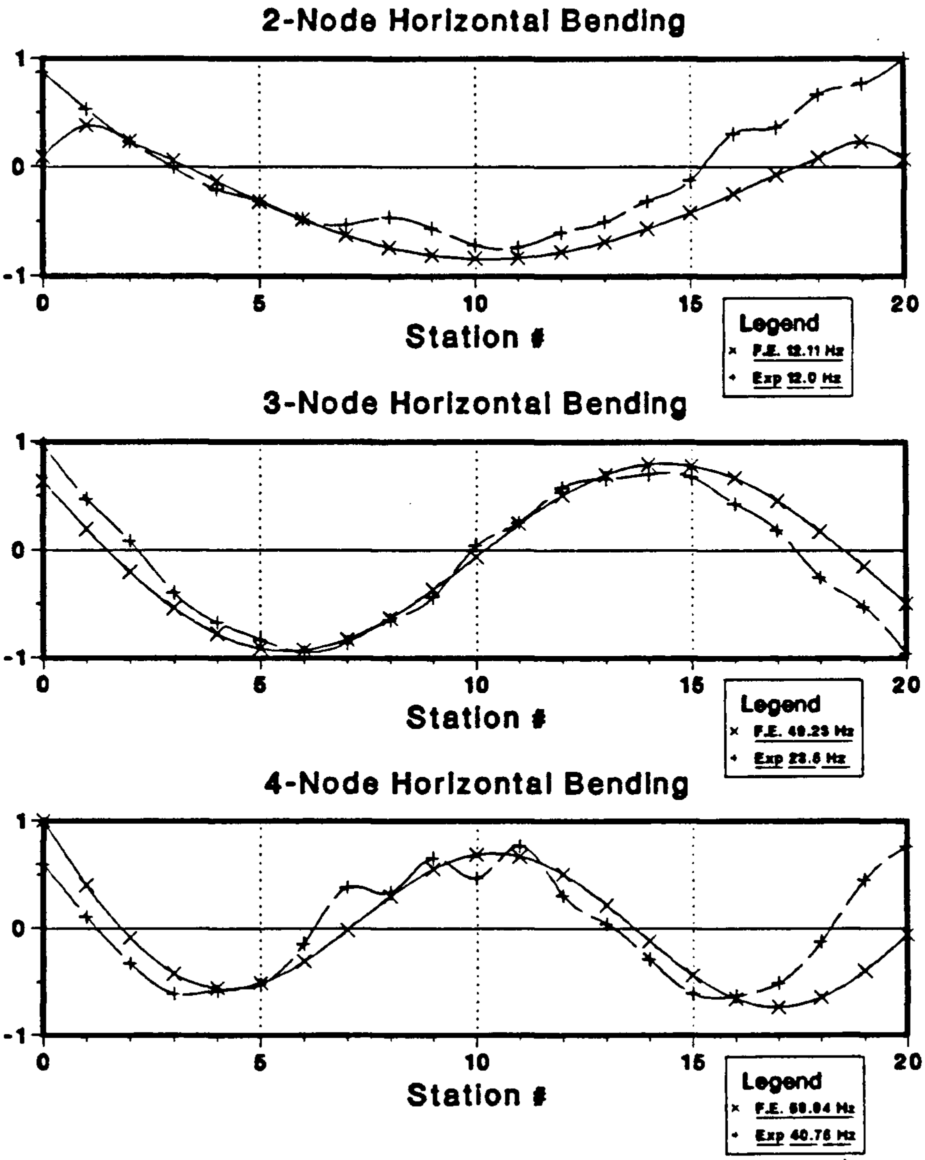

Figure 5.14 - Finite Element and Experimental
Horizontal Modes of the Ship Model
Air for 30 lb Load Condition

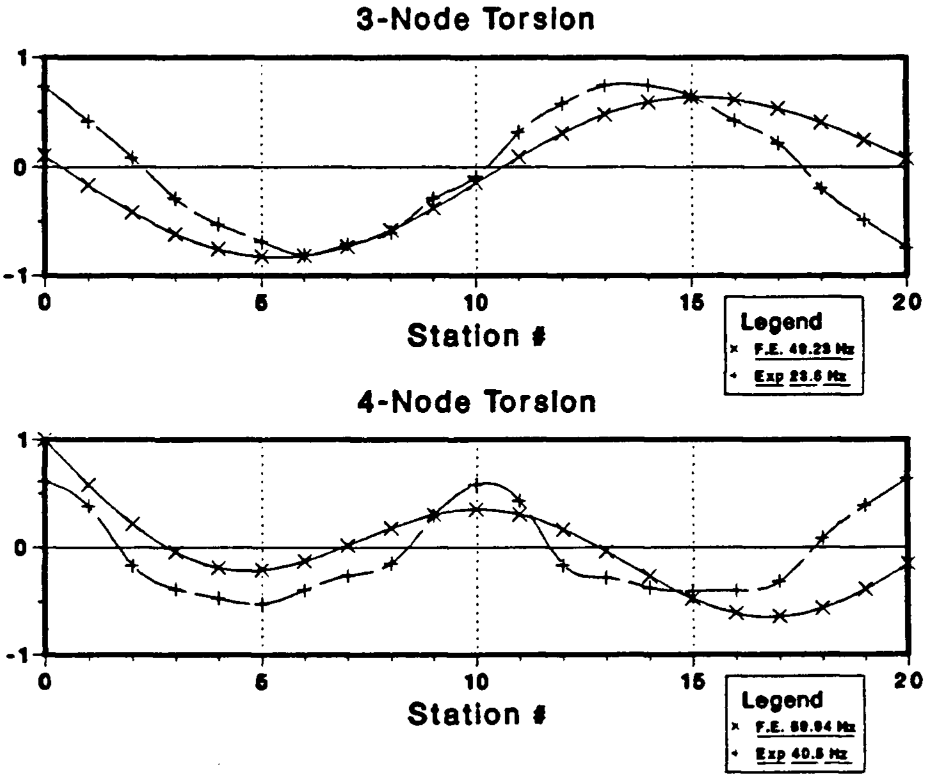

Figure 5.15 - Finite Element and Experimental Torsional Modes of the Ship Model Air for 30 lb Load Condition

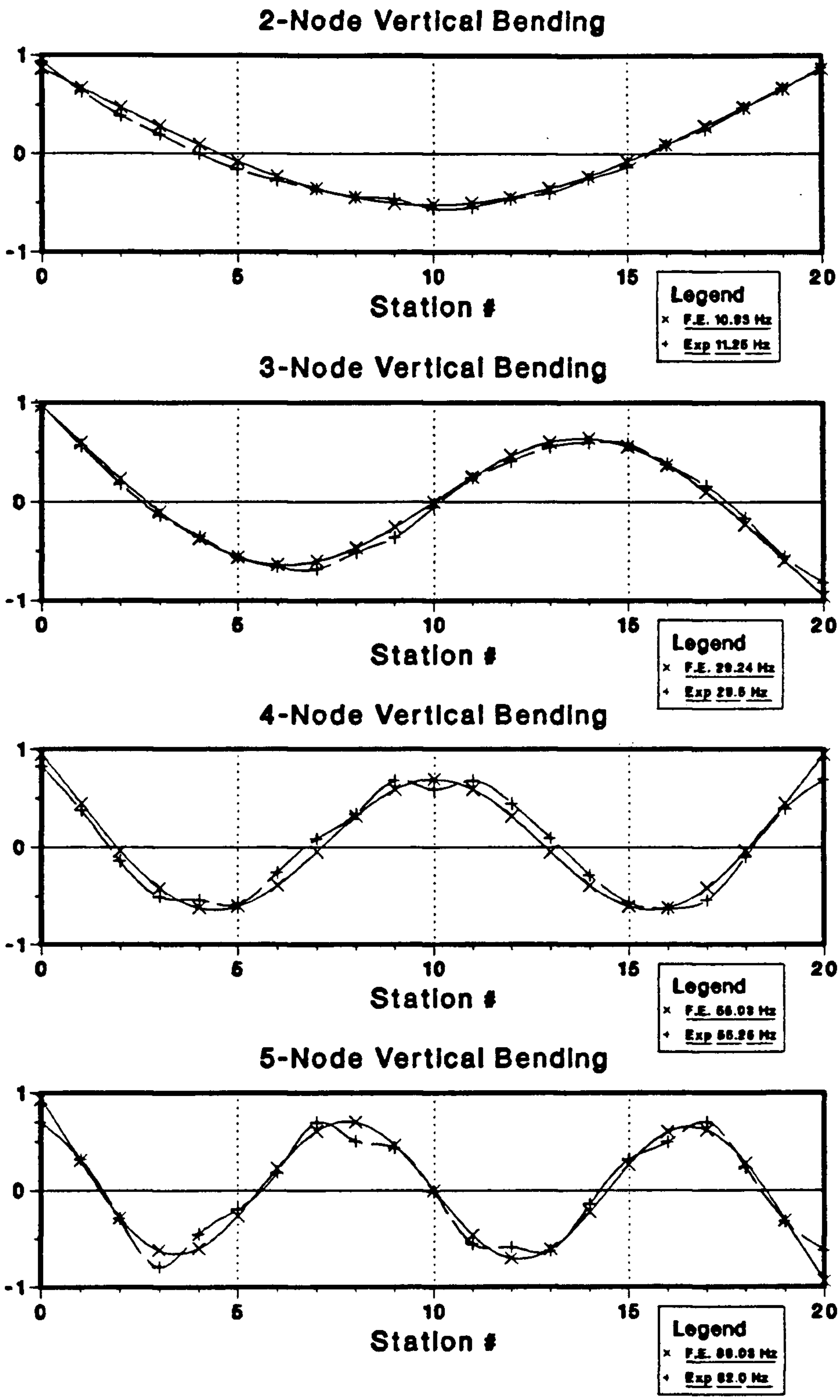

Figure 5.16 - Finite Element and Experimental Vertical Modes of the Ship Model Air for 40 lb Load Condition

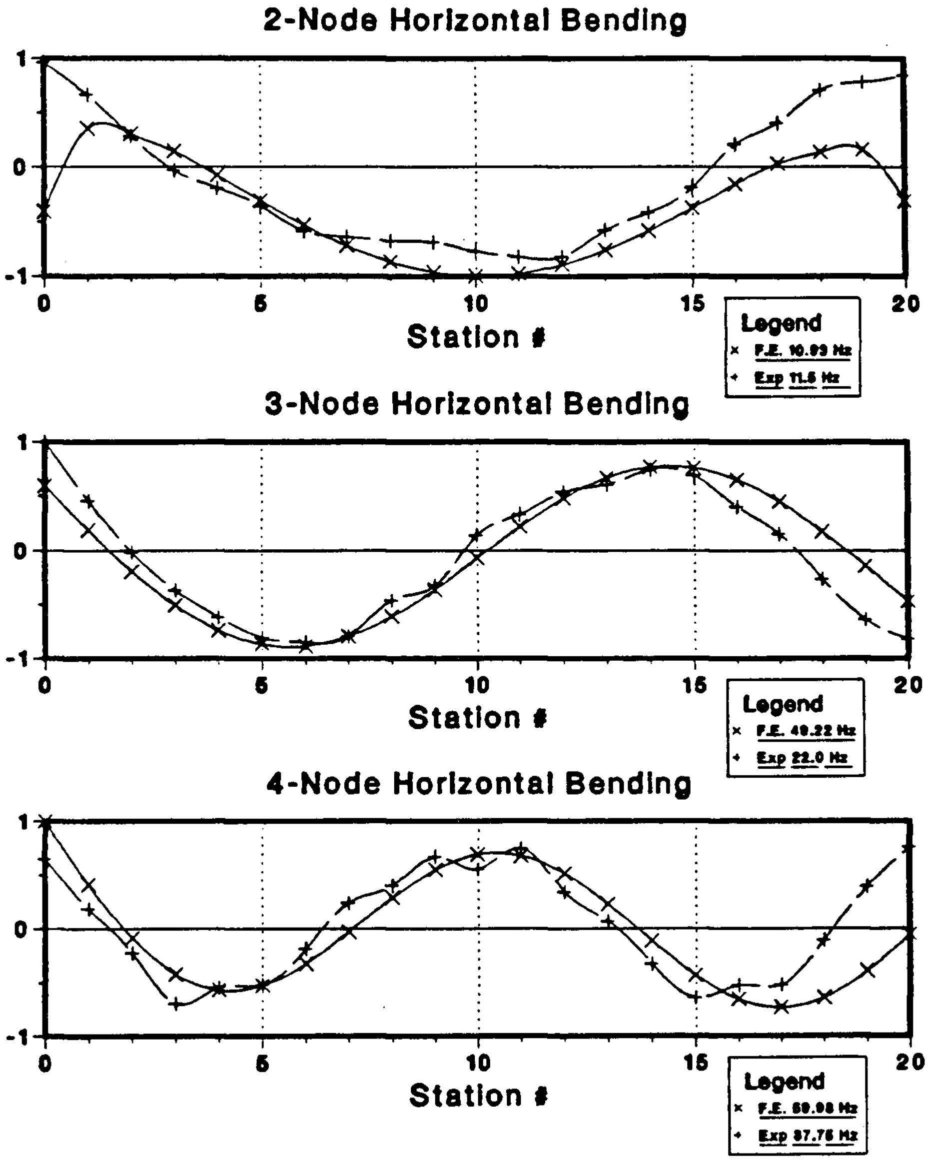

Figure 5.17 - Finite Element and Experimental
Horizontal Modes of the Ship Model
Air for 40 lb Load Condition

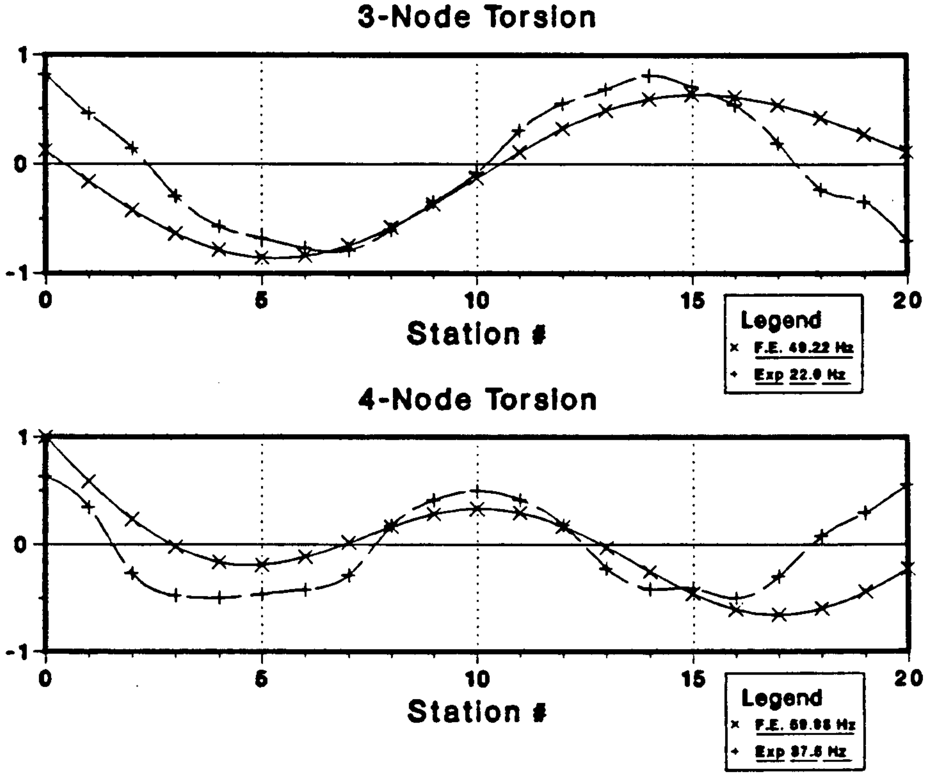

Figure 5.18 - Finite Element and Experimental Torsional Modes of the Ship Model Air for 40 lb Load Condition

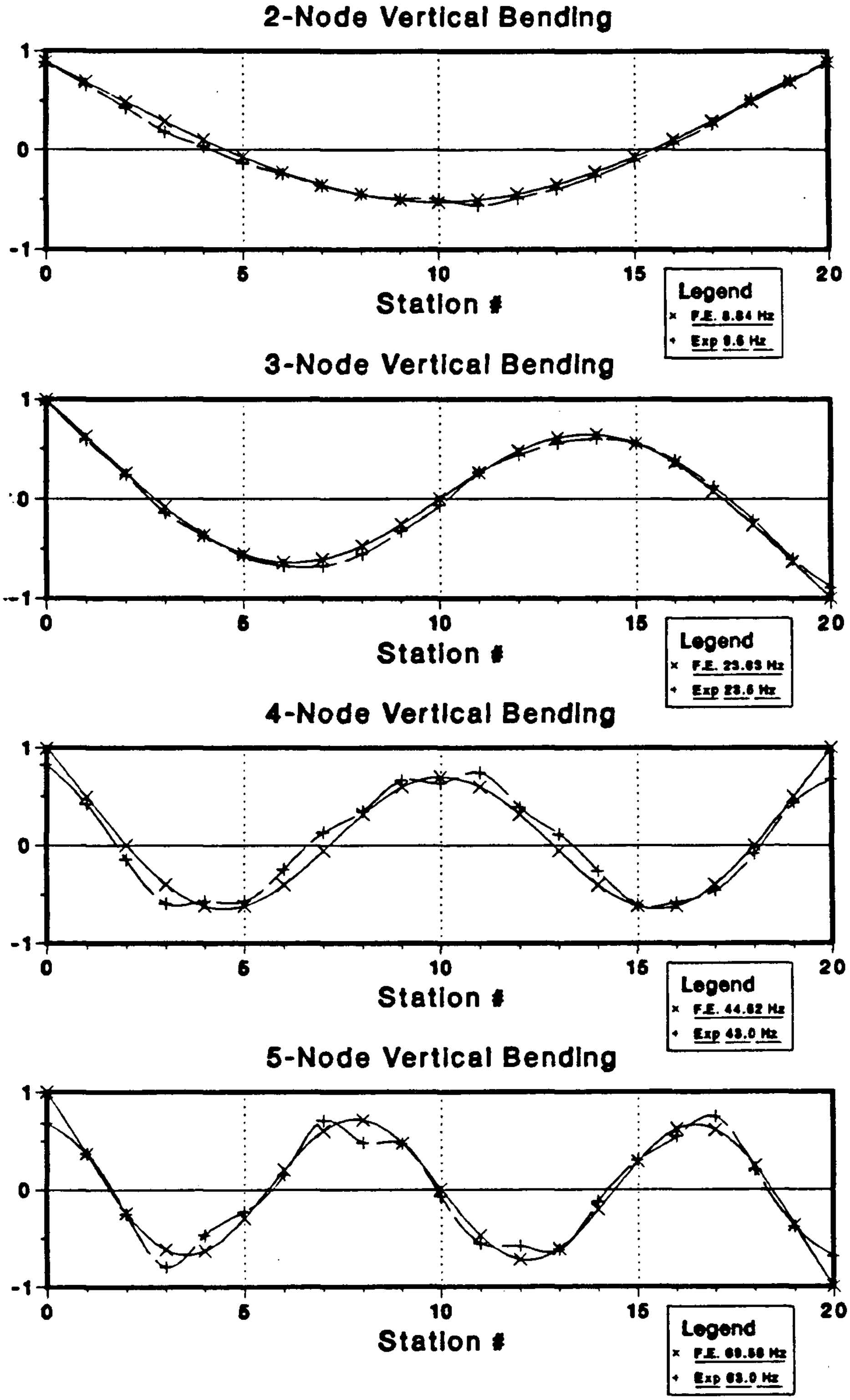

Figure 5.19 - Finite Element and Experimental Vertical Modes of the Ship Model Air for 70 lb Load Condition

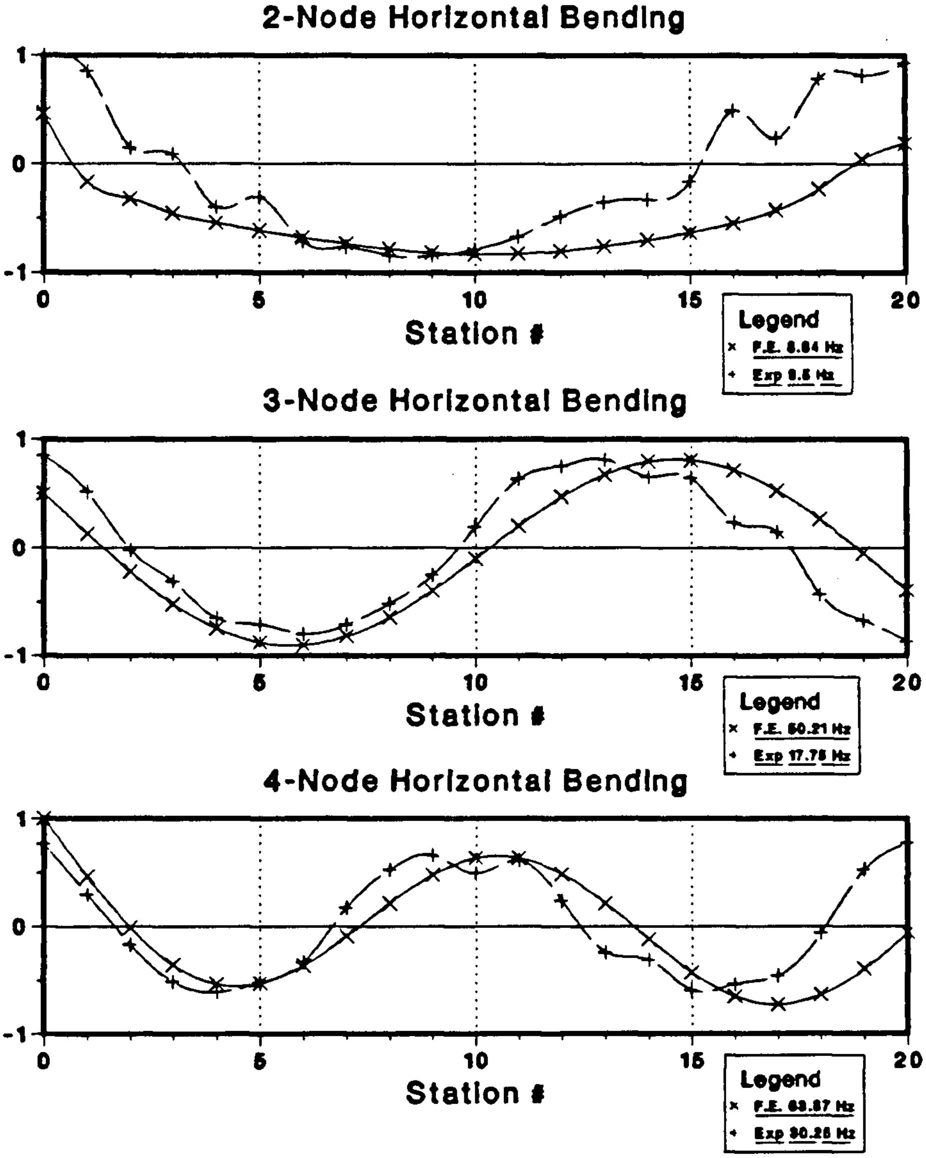

Figure 5.20 - Finite Element and Experimental Horizontal Modes of the Ship Model Air for 70 lb Load Condition

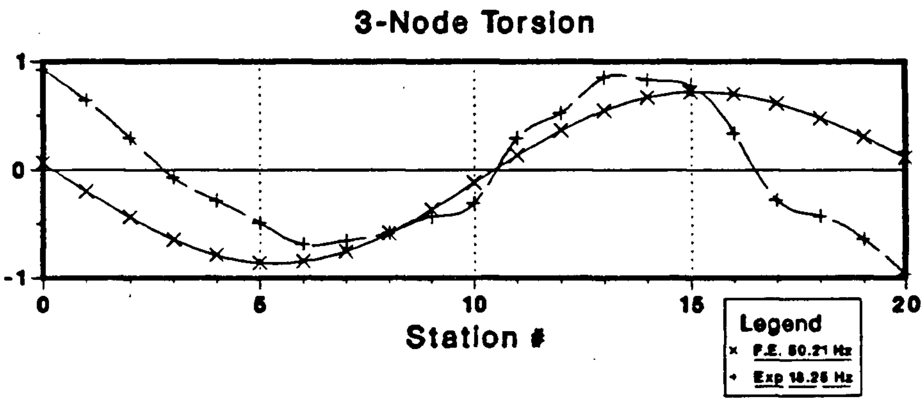

Figure 5.21 - Finite Element and Experimental
Torsional Modes of the Ship Model
Air for 70 lb Load Condition

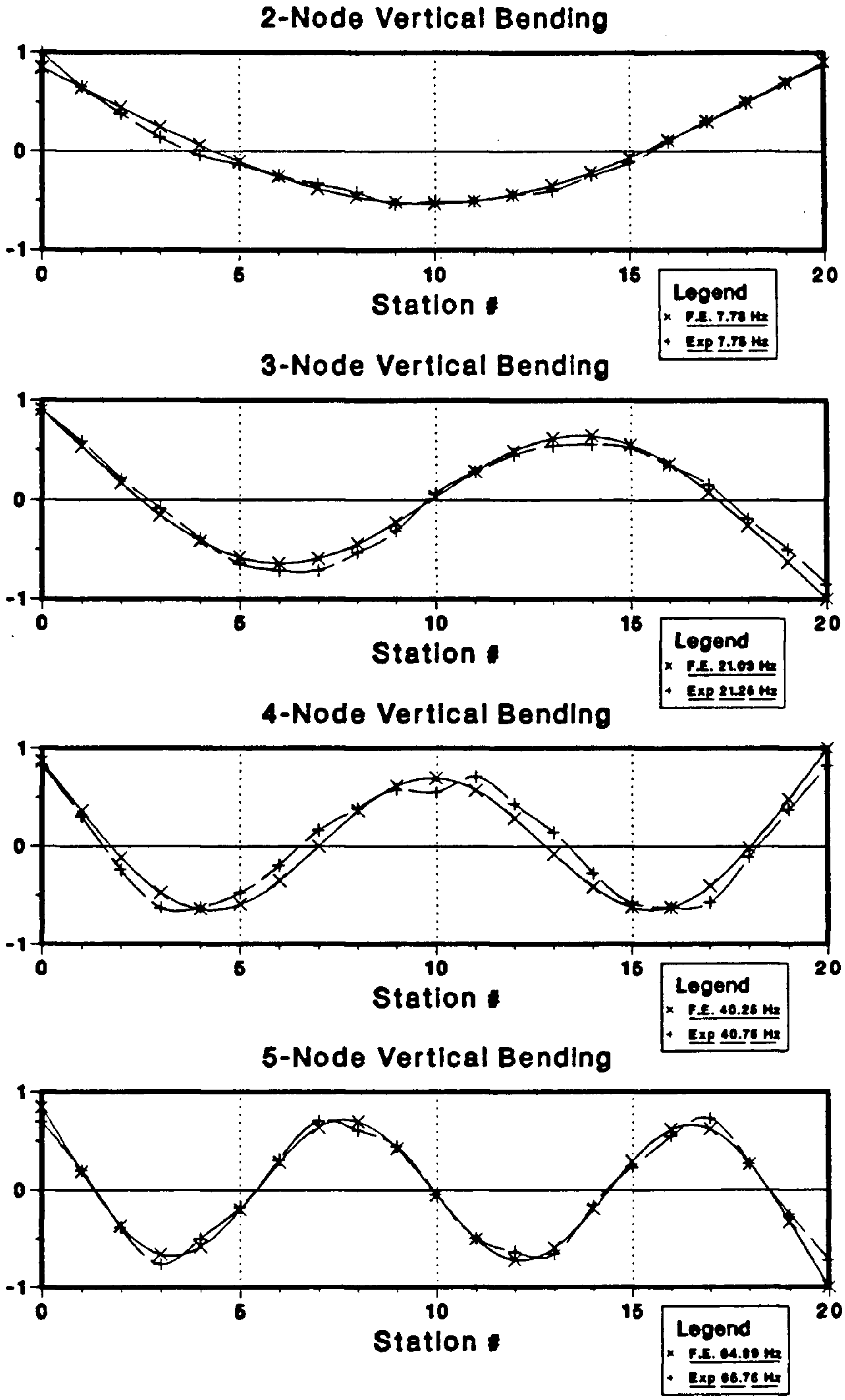

Figure 5.22 - Finite Element and Experimental Vertical Modes of the Ship Model Water for 30 lb Load Condition

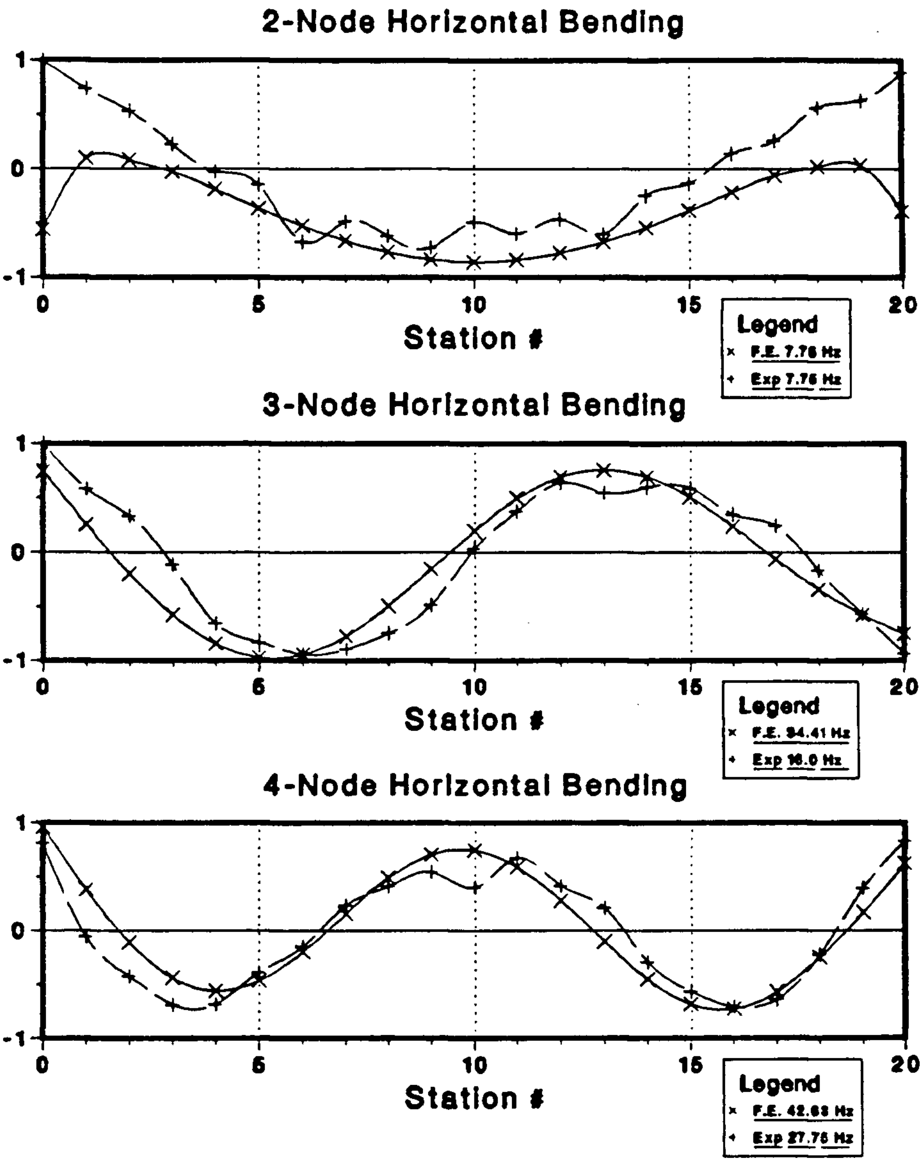

Figure 5.23 - Finite Element and Experimental Horizontal Modes of the Ship Model Water for 30 lb Load Condition

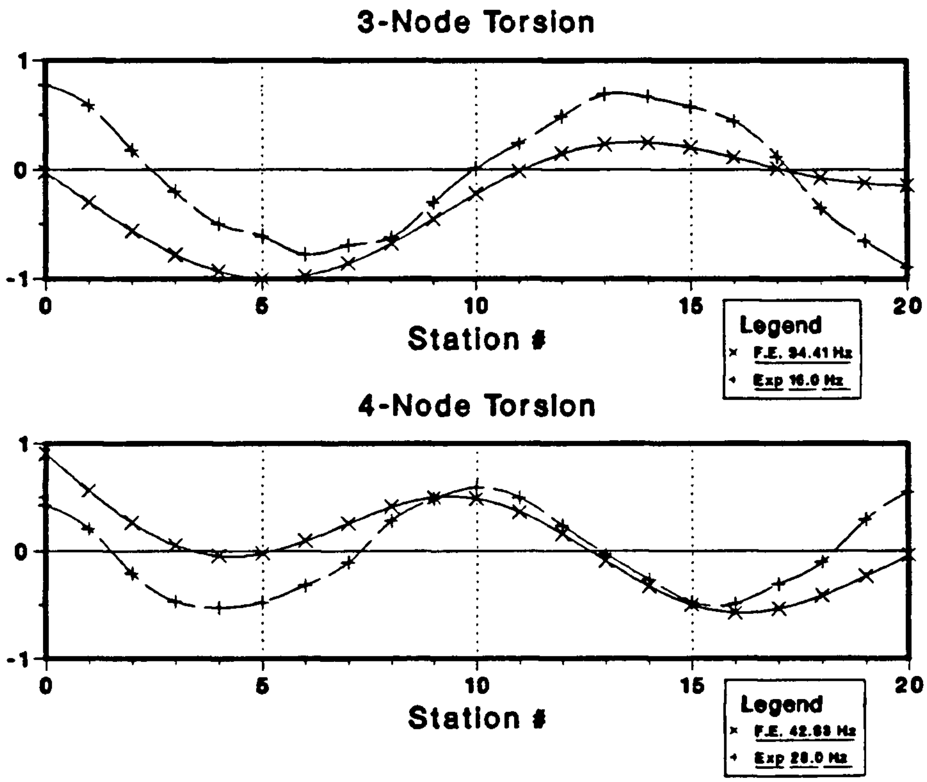

Figure 5.24 - Finite Element and Experimental
Torsional Modes of the Ship Model
Water for 30 lb Load Condition

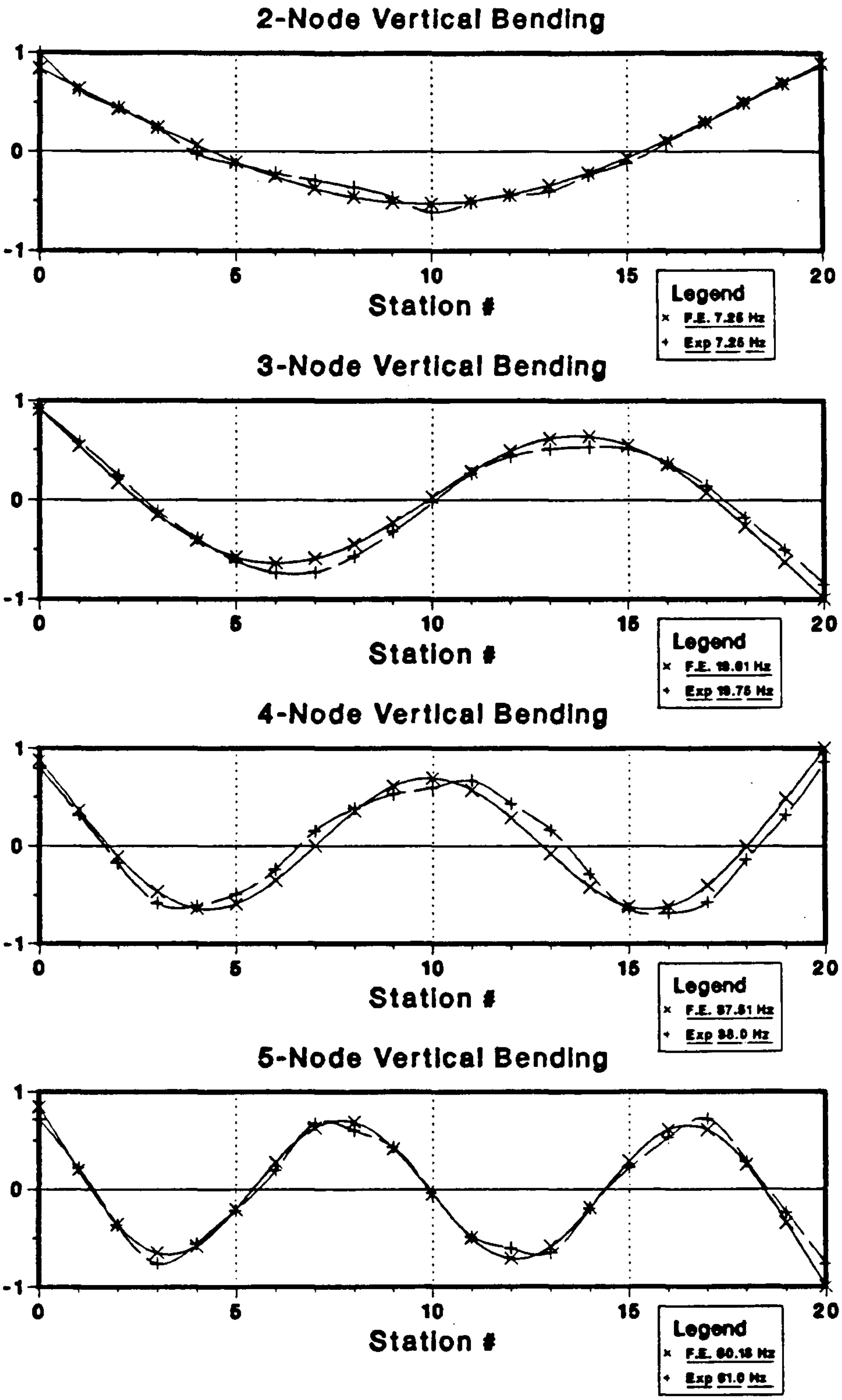

Figure 5.25 - Finite Element and Experimental Vertical Modes of the Ship Model Water for 40 lb Load Condition

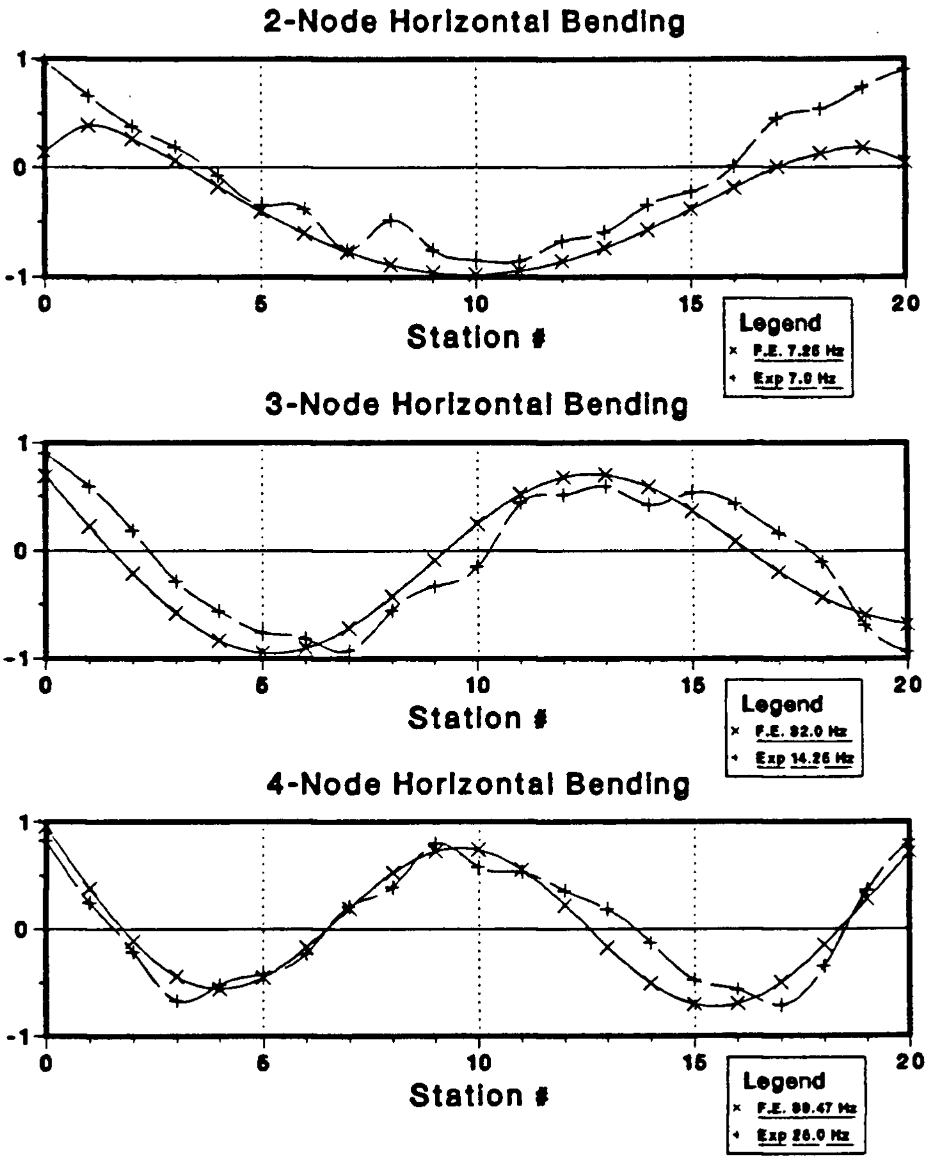

Figure 5.26 - Finite Element and Experimental Horizontal Modes of the Ship Model Water for 40 lb Load Condition

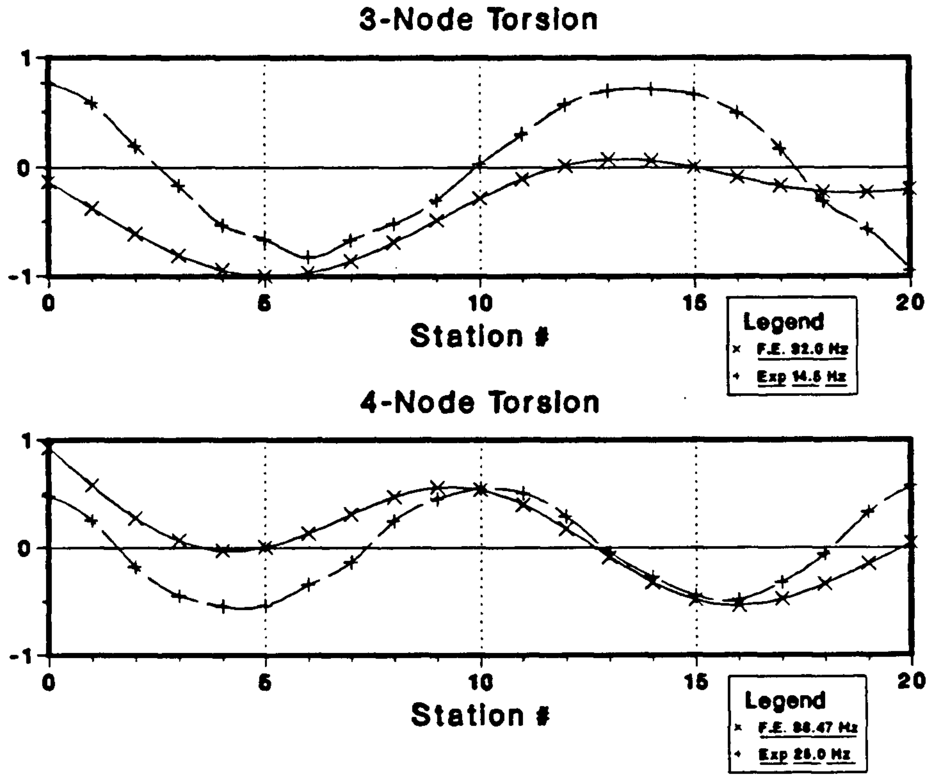

Figure 5.27 - Finite Element and Experimental Torsional Modes of the Ship Model Water for 40 lb Load Condition

6. CONCLUSIONS

The investigation of the fluid modelling capabilities of VAST shows that the extent of the finite element fluid domain is important. If this domain is not extended far enough from the vibrating structure, the numerical results will be higher than those that would be determined experimentally. With regard to discretization of the fluid domain, the 20-noded fluid element performs better than the 8-noded fluid element. In meshes that contain either the 8 or the 20-noded fluid element but have the same number of degrees of freedom, the 20-noded fluid element predicts the experimental frequencies more accurately than the 8-noded fluid element. As well, meshes that contain the infinite element in their last row run faster and have slightly better results than meshes that do not contain the infinite fluid element. However, if the real fluid flow has vortex shedding, the frequencies predicted by the finite element representation of the fluid will be below the actual results.

In the experimental testing of the ship model, the lowest four modes of vertical, horizontal, and torsional vibration were identified, and the effect of draught on the frequencies and modes shapes was recorded. This experimental work will prove useful when compared with numerical methods of predicting the frequencies and mode shapes in both air and water. The experimental results show that the added mass of the fluid has little effect on the lowest mode shapes of vibration; however, if there is local bending occurring in the air mode shapes, the fluid reduces this local bending. As well, these results show that the effect of the added mass decreases as the complexity of the mode shapes increases.

When the experimentally obtained frequencies and mode shapes for the ship model are compared with the numerical predictions of VAST, good agreement is found in both air and water tests for the vertical vibration modes. However, there is little agreement with the horizontal and torsional modes. This poor agreement is due to the finite element's inability to model the shear flow and warping effects encountered in the horizontal-torsional coupled modes.

BIBLIOGRAPHY

[1] Ahmah, S., Irons, B.M., and Zienkiewicz, O.C. "Analysis of Thick and Thin Shell Structures by Curved Finite Elements." International Journal for Numerical Methods in Engineering, 2 (1970), 419-451.

[2] Anderson, G., and Norrand, K. "A Method for the Calculation of Vertical Vibration with Several Nodes and Some Other Aspects of Ship Vibration." Transactions, Royal Institution of Naval Architects, 111 (1969), 367-383.

[3] Archer, J.S. "Consistant Mass Matrix Formulation for Structural Analysis Using Finite Element Techniques." Journal of the American Institute of Aeronautics and Astronautics, 3, No.10 (1965), 1910-1918.

[4] Armand, J.L., and Orsero, P. "A Method for Evaluating the Hydrodynamic Added Mass in Ship Hull Vibration." Transactions, Society of Naval Architects and Marine Engineers, 87 (1979), 99-120.

[5] Armand, J.L., Orsero, P., and Robert, O. "Dynamic Analysis of the Afterbody of a Ship--Towards a Successful correlation Between Analytical and Experimental Results." Ship Vibration Symposium, Society of Naval Architects and Marine Engineers, 1978, M1-M16.

[6] Beer, G., and Meek, J.L. "Infinite Domain Elements." International Journal for Numerical Methods in Engineering, 17 (1981), 43-52.

[7] Bettess, P. "Infinite Elements." International Journal for Numerical Methods in Engineering, 11 (1977), 53-64.

[8] Bishop, R.E.D., and Gladwell, G.M.L. "An Investigation into the Theory of Resonance Testing." Transactions, Proceedings of the Royal Society of Philosophical, 255, 241-80.

[9] Bishop, R.E.D., and Price, W.G. "Coupled Bending and Twisting of a Timoshenko Beam." Journal of Sound and Vibration, 50 (1977), 469-477.

[10] Bishop, R.E.D., and Price, W.G. Hydroelasticity of Ships. Cambridge University Press, 1979.

[11] Bishop, R.E.D., Price, W.G., and Temarel, P. "Antisymmetric Vibration of Ship Hulls." Transactions, Royal Institution of Naval Architects, 122 (1980), 197-208.

[12] Bishop,R.E.D., Price, W.G., and Temarel, P. "A Study of Mode Shapes in Hull Vibration of Low Frequency." Transactions, Royal Institution of Naval Architects, 120 (1978), 121-134.

[13] Bishop, R.E.D., Price, W.G., and Temarel, P. "A Unified Dynamical Analysis of antisymmetric Ship Response to Waves." Transactions, Royal Institution of Naval Architects, 122 (1980), 349-365.

[14] Burrill,L.C., Robson, W., and Townsin, R.L. "Ship Vibration : Entrained Water Experiments." Transactions, Royal Institution of Naval Architects, 104 (1962), 415-445.

[15] Cook, R.D. Concepts and Applications of Finite Element Analysis. 2nd ed. New York: John Wiley and Sons Inc. 1981.

[16] Daidola, J.C. "Natural Vibrations of Beams in a Fluid with Applications to Ships and Other Marine Structures." Transactions, Society of Naval Architects and Marine Engineers, 92 (1984), 331-351.

[17] Deruntz, J.A., and Geers, T.L. "Added Mass Computation by the Boundary Integral Method." International Journal for Numerical Methods in Engineering, 12 (1978), 531-549.

[18] Ewins, D.J. Modal Testing: Theory and Practice. Hertfordshire, England: John Wiley and Sons Inc. 1984.

[19] Haszpra, O. Modelling Hydroelastic Vibrations. Pitman 1977, 46-70.

[20] Hylarides, S., and Vorus, W.S. "The Added Mass Matrix in Ship Vibration, Using a Source Distribution Related to the Finite Element Grid of the Ship Structure." Intenational Shipbuilding Progress, 24, No.330 (1982), 34-43.

[21] Instruction Manual of Model 660A Dual-Channel FFT Analyzer, Nicolet Scientific Corporation.

[22] Kiefling, L., and Feng, G.C. "Fluid-Structure Finite Element Vibrational Analysis." Journal of the American Institute of Aeronautics and Astronautics, 14, No.2 (1976), 199-203.

[23] Kim, C.H. "Effect of Mesh Size on the Accuracy of Finite-Water Added Mass." Journal of Hydronautics, 9, No.3 (July 1975), 125-126.

[24] Kumai, T. "Virtual Inertia Coefficients and Response Factors in Higher Modes of Main Hull Vibration." Transactions Royal Institution of Naval Architects, 119 (1977).

[25] Kuo, C. "Vertical Ship Vibration Ingestigation with an 11 ft. Xylonite Model." Doctor of Philosophy Thesis, University of Glasgow, 1960.

[26] Landweber, L., and deMacaque, M.C. "Added Mass of Two-Dimensional Forms Oscilating in a Free Surface." Journal of Ship Research, 1, No.3 (November 1957), 20-30.

[27] Landweber, L., and Macagno, M. "Added Masses of Two-Dimensional Forms by Conformal Mapping." Journal of Ship Research, 11, No. 2 (June 1967), 109-116.

[28] Lewis, F.M. "The Inertia of Water Surrounding a Vibrating Ship." Transactions, Society of Naval Architects and Marine Engineers, 37 (1929), 1-20.

[29] Lindholm, U.S., Kana, D.D., Chu, W.-H.,and Abramson, H.N. "Elastic Vibration Characteristics of Cantilever Plates in Water." Journal of Ship Research, 9, No.1 June 1965), 11-22.

[30] Marcus, M.S. "A Finite-Element Method Applied fo the Vibration of Submerged Plates." Journal of Ship Research, 22, No.2 (June 1978), 94-99.

[31] Meirovitch, L. Analytical Methods in Vibration. London: Collier-MacMillan Ltd., 1967.

[32] Moullin, E.B., Browne, A.D., and Perkins, A.J. "The Added Mass of Prisms Floating in Water." Proceedings, Cambridge Philosophical Society, 1930, 258-272.

[33] Murray, M.A., Agar, T.J., and Jennings, A. "Evaluation of Virtual Mass Matrices for Ship Hulls Using Fluid Singularities." Recent Advances in Structural Dynamics, 2 (1980), 403-415.

[34] Newman, J.N. Marine Hydrodynamics. Cambridge, Massachusetts and London, England: MIT Press, 1977.

[35] Norwood, M.E. "Analysis of Shell Structures by Curved Finite Elements." Halifax, Nova Scotia: Martec Limited, 1975.

[36] Norwood, M.E. "Application of the Finite Element Method for the Calculation of the Hydrodynamic Added Mass of Marine Propeller Blades." Halifax, Nova Scotia: Martec Limited, 1977.

[37] Orsero, P., and Armand, J.L. "A Numerical Determination of the Entrained Water in Ship Vibrations." International Journal for Numerical Methods in Engineering, 13 (1978), 35-48.

[38] Piezoelectric Accelerometers and Vibration Preamplifiers Theory and Application Handbook, Brüel & Kjær, 1978.

[39] Restad, K., Volcy, G.C., Garnier, H., and Masson, J.C. "Investigation on Free and Forced Vibrations on an LNG Tanker with Overlapping Propeller Arrangements." Transactions, Society of Naval Architects and Marine Engineers, 81 (1973), 307-347.

[40] Talyor, J.L. "Some Hydrodynamic Inertia Coefficients." Philosophical Magazine, 9 (1930), 161-183.

[41] Thomson, W.T. Theory of Vibration with Applications. 2nd ed., Englewood Cliffs, New Jersey: Prentice Hall Inc., 1981.

[42] Townsin, R.L. "Virtual Mass Reduction Factors, 'J' Values for Ship Vibration Calculations Derivied from Tests with Beams Including Ellipsods and Ship Models." Transactions, Royal Institution of Naval Architects, 111 (1969), 385-397.

[43] Troesh, A.W. "Wave-Induced Hull Vibrations : An Experimental and Theoretical Study." Journal of Ship Reseach, 28, No.2 (June 1984), 141-150.

[44] Tse, F.S., Morse, I.E., and Hinkle, R.T. Mechanical Vibrations Theory and Applications. 3rd ed. Boston: Allyn and Bacon Inc., 1978.

[45] Vibration and Strength Analysis Program VAST : User's Manual Version #4, Martex Limited, Halifax, Nova Scotia 1986.

[46] Vorus, W.S., and Hylarides, S. "Hydrodyanmic Added-Mass Matrix of Vibrating Ship Based on a Distribution of Hull Surface Sources." Transactions, Society of Naval Architects and Marine Engineers, 89 (1981), .

[47] Zienkiewicz, O.C. The Finite Element Method. 3rd ed. London: McGraw-Hill Ltd., 1983.

[48] Zienkiewicz, O.C., and Bettess, P. "Fluid-Structure Dynamic Interaction and Wave Forces, An Introduction to Numerical Treatment." International Journal for Numerical Methods in Engineering, 13 (1978), 1-16.

[49] Zienkiewicz, O.C., and Bettess, P. "Infinite Elements in the Study of Fluid Structure Interaction Problems." 2nd International Symposium, Computational Methods in Applied Science and Engineering, Versailles, France 1975, 133-157.

[50] Zienkiewicz, O.C., Kelly, D.W., and Bettess, P. "The Coupling of the Finite Element Method and Boundary Solution Procedures." International Journal for Numerical Methods in Engineering, 11 (1977), 355-375.

APPENDIX A - VARIATIONAL PRINCIPLE

This appendix will show that the variational principle that governs the fluid problem is given by

$$\delta\iiint \frac{1}{2}\left[\left(\frac{\partial\phi}{\partial x}\right)^2+\left(\frac{\partial\phi}{\partial y}\right)^2+\left(\frac{\partial\phi}{\partial z}\right)^2\right]dxdydz - \delta\iint \frac{\partial\phi}{\partial n}\,\phi\, dS_n = 0 \quad (A.1)$$

where ϕ is the velocity potential of the fluid, S_n is the interface area between the fluid and the structure, and v_n is the velocity normal to S_n. The velocity potential ϕ may be taken as zero at the boundaries and on the free surface (as discussed in Section 2.1). This variational principle can be shown to be the correct one for the problem, if

$$I = \iiint \frac{1}{2}\left[\left(\frac{\partial\phi}{\partial x}\right)^2+\left(\frac{\partial\phi}{\partial y}\right)^2+\left(\frac{\partial\phi}{\partial z}\right)^2\right]dxdydz - \iint \frac{\partial\phi}{\partial n}\,\phi\, dS_n \quad (A.2)$$

Taking the first variation of equation A.2, the following is obtained

$$\delta I = \iiint\left[\phi_x\delta\phi_x + \phi_y\delta\phi_y + \phi_z\delta\phi_z\right]dxdydz - \iint \frac{\partial\phi}{\partial n}\,\delta\phi\, dS_n = 0 \quad (A.3)$$

where the subscript x stands for derivative by x, and so on. Applying Green's theorem

$$\iiint_{\Omega} \nabla u \nabla v d\mathbb{V} = -\iiint_{\Omega} u\nabla^2 v d\mathbb{V} + \iint u(\nabla v\cdot n)dS$$

to equation A.3, it becomes

$$\delta I = - \iiint \nabla^2\phi \ \delta\phi \ dxdydz + \iint (\nabla\phi \cdot n)\delta\phi \ dS - \iint \frac{\partial\phi}{\partial n} \ \delta\phi \ dS_n = 0$$

Noting that $\nabla\phi \cdot n = \dfrac{\partial\phi}{\partial n}$, then

$$\delta I = - \iiint \nabla^2\phi \ \delta\phi \ dxdydz + \iint \frac{\partial\phi}{\partial n} \ \delta\phi \ dS - \iint \frac{\partial\phi}{\partial n} \ \delta\phi \ dS_n = 0$$

$$\delta I = - \iiint \nabla^2\phi \ \delta\phi \ dxdydz = 0 \tag{A.4}$$

and for arbitrary $\delta\phi$

$$\nabla^2\phi = 0 \tag{A.5}$$

with the appropriate boundary conditions (as discussed in Section 2.1).

APPENDIX B - FLUID ELEMENT SHAPE FUNCTIONS

This appendix will present the shape functions of the three fluid elements that were used in the numerical work. As well, there were two interface elements that were used to connect the fluid elements to the structure. These elements assured that the boundary condition of

$$\frac{\partial \phi}{\partial n} = v_n \tag{2.10a}$$

was met on the fluid-strucutre interface.

B.1 8-Noded Fluid Element

This element was a three-dimensional element with 8 nodes, one at each corner. This element had linear shape functions given by

$$N_i = \frac{1}{8} (1 + \xi\xi_i)(1 + \eta\eta_i)(1 + \zeta\zeta_i) \tag{B.1}$$

(Figure B.1 presents a general representation of this element.)

B.2. 4-Noded Interface Element

This element was used to connect the 8-noded fluid element to the structure that the fluid was surrounding. The shape functions for this element were

$$N_i = \frac{1}{4} (1 + \eta\eta_i)(1 + \zeta\zeta_i) \qquad \text{(B.2)}$$

(Figure B.1 presents a general representation of this element.)

B.3. 20-Noded Fluid Element

This element was a three-dimensional element with 20 nodes, one at each corner and one at each mid-side. This element had quadratic shape functions and was an isoparametric element.

corner nodes:

$$N_i = \frac{1}{8} (1 + \xi\xi_i)(1 + \eta\eta_i)(\xi\xi_i + \eta\eta_i + \zeta\zeta_i - 2) \qquad \text{(B.3)}$$

mid-side nodes:

$$N_i = \frac{1}{4} (1- \xi^2)(1 + \eta\eta_i)(1 + \zeta\zeta_i) \qquad \xi_i = 0 \qquad \text{(B.4)}$$

$$N_i = \frac{1}{4} (1- \eta^2)(1 + \xi\xi_i)(1 + \zeta\zeta_i) \qquad \eta_i = 0 \qquad \text{(B.5)}$$

$$N_i = \frac{1}{4} (1- \zeta^2)(1 + \zeta\zeta_i)(1 + \eta\eta_i) \qquad \zeta_i = 0 \qquad \text{(B.6)}$$

(Figure B.2 presents a general representation of this element.)

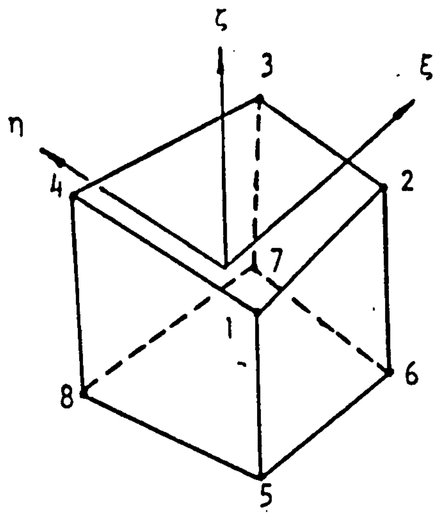

a) 8-Noded Fluid Element

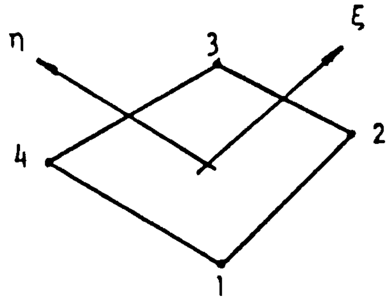

b) 4-Noded Interface Element

Figure B.1 - 8-Noded Fluid Element and 4-Noded Interface Element

B.4. 8-Noded Interface Element

This element was used to connect the 20-noded fluid element to the structure that the fluid was surrounding. The shape functions for this element were

corner nodes:

$$N_i = \frac{1}{4} (1 + \eta\eta_i)(\eta\eta_i + \zeta\zeta_i - 1) \tag{B.7}$$

mid-side nodes:

$$N_i = \frac{1}{2} (1- \eta^2)(1 + \zeta\zeta_i) \qquad \eta_i = 0 \tag{B.8}$$

$$N_i = \frac{1}{2} (1- \zeta^2)(1 + \eta\eta_i) \qquad \zeta_i = 0 \tag{B.9}$$

(Figure B.2 presents a general representation of this element.)

B.5. 8-Noded Infinite Fluid Element

This element was a three-dimensional infinite element with 8 nodes, one at each corner. In the two non-infinite coordinates, the shape functions were standard, while in the infinite direction ξ_n, special shape functions N_i^{∞} were used. The velocity potential was given as

$$\phi_e = \sum_{i=1}^{NNE} \bar{N}_i \phi_i \tag{B.10}$$

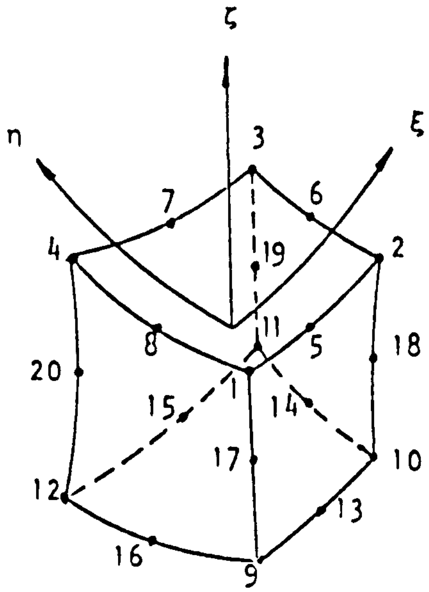

a) 20-Noded Fluid Element

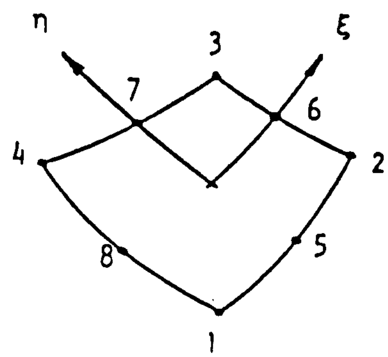

b) 8-Noded Interface Element

Figure B.2 - 20-Noded Fluid Element and 8-Noded Interface Element where

$$\bar{N}_i = N_i N_i^{\alpha} \tag{B.11}$$

with

$$N_i = \frac{1}{8} (1 + \eta\eta_i)(1 + \zeta\zeta_i) \tag{B.12}$$

and

$$N_i^{\alpha} = 2 (\xi_i + \frac{1}{2}) \xi + 1 + \zeta_i \qquad \xi_i < 0 \tag{B.13}$$

$$N_i^{\alpha} = 2 (\xi_i + \frac{1}{2})\left[\frac{\xi}{1 - \xi} \right] + 1 + \zeta_i \qquad \xi_i > 0 \tag{B.14}$$

Note that $\sum \bar{N}_i = 1$, which was the normal isoparametric criterion for an element's shape functions. (Figure B.3 presents a general representation of this element.)

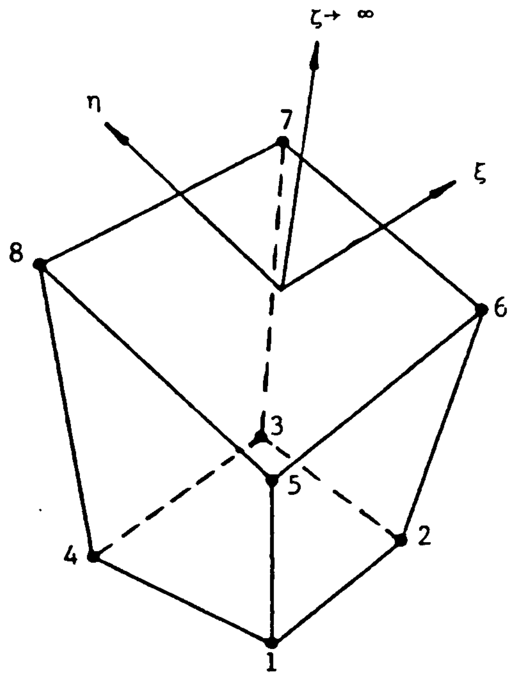

Figure B.3 - 8-Noded Infinite Fluid Element

APPENDIX C - THICK/THIN SHELL ELEMENT MASS AND STIFFNESS MATRIX

This appendix will present the isoparametric formulation of the curved shell element available in the Finite Element Program VAST as presented by Norwood [35] and developed by Ahmah et al [1]. This element is knowng as the Thick/Thin Shell element IEC = 1 in VAST. This element has 8 nodes in total, 4 corner nodes and 4 mid-side nodes, with 5 local degrees of freedom per node, 3 translations, and 2 rotations.

By drawing from the development of large curvilinear elements for three-dimensional analysis, this element overcomes some of the previous approximations to geometry of the structure and the neglection of shear deformation. As well, the formation of the element takes advantage of the fact that even for thick shells, the 'normals' to the middle surface remain practically straight after deformation.

Consider the three-dimensional isoparametric element (shown in Figure C.1). The external faces of the element are curved, while the sections across the thickness are generated by straight lines. If ξ and η are two curvilinear coordinates in

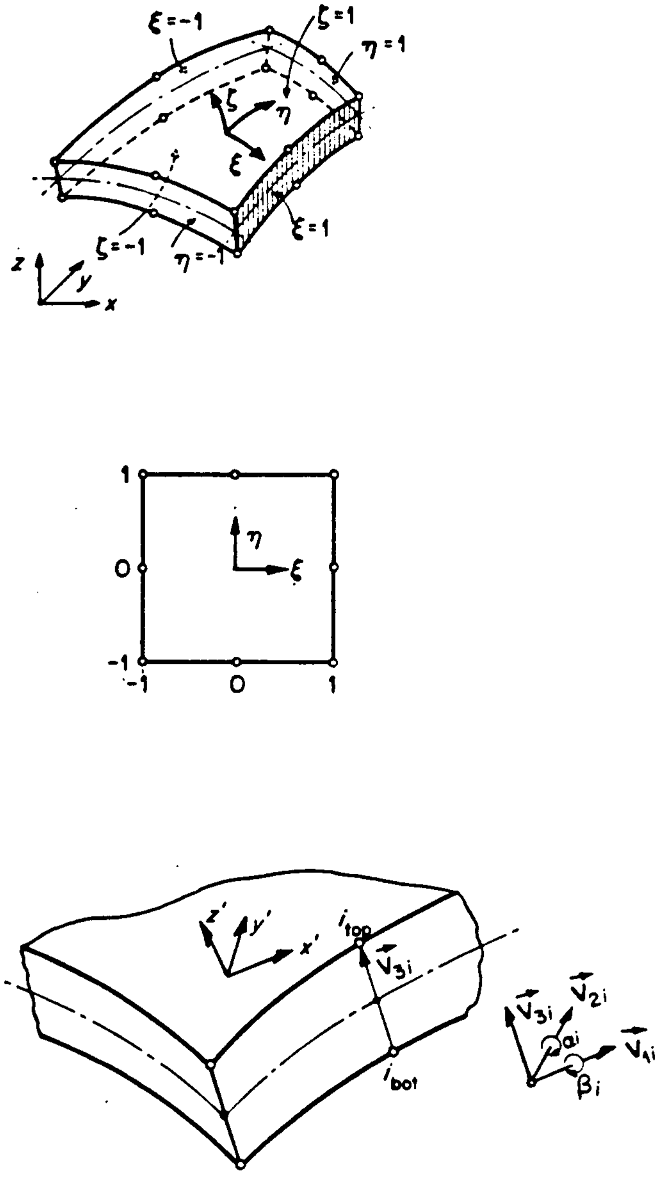

Figure C.1 - Curved Shell Element

the middle plane of the element, and ζ is a linear coordinate in the thickness direction varying between +1 and -1, then a relation between the local curvilinear coordinates and the xyz Cartesian coordinate system can be established as

$$\begin{Bmatrix} x \\ y \\ z \end{Bmatrix} = \sum N_i(\xi,\eta) \frac{(1+\zeta)}{2} \begin{Bmatrix} x_i \\ y_i \\ z_i \end{Bmatrix}_{top} + \sum N_i(\xi,\eta) \frac{(1+\zeta)}{2} \begin{Bmatrix} x_i \\ y_i \\ z_i \end{Bmatrix}_{lower} \quad (C.1)$$

Here, $N_i(\xi,\eta)$ is a shape function, taking a value of unity at node i, and zero at all other nodes. If the shape functions are chosen so that compatibility is achieved between elements at their interface, then the shape functions may be written as

corner nodes :

$$N_i = \frac{1}{4}(1+\xi\xi_i)(1+\eta\eta_i)(\xi\xi_i+\eta\eta_i-1) \quad (C.2)$$

mid-side nodes :

$$N_i = \frac{1}{2}(1+\xi\xi_i)(1-\eta^2) \qquad (\xi = \pm 1,\ \eta = 0) \quad (C.3)$$

$$N_i = \frac{1}{2}(1+\eta\eta_i)(1-\xi^2) \qquad (\eta = \pm 1,\ \xi = 0) \quad (C.4)$$

It is convenient to rewrite equation C.1 in a form specified by a vector connecting the upper and lower surfaces and the coordinates of the mid-surface. Thus

$$\begin{Bmatrix} x \\ y \\ z \end{Bmatrix} = \sum N_i(\xi,\eta) \begin{Bmatrix} x_i \\ y_i \\ z_i \end{Bmatrix}_{mid} + \sum N_i(\xi,\eta) \frac{\zeta}{2} \mathbf{V}_{3i} \quad (C.4)$$

with

$$\mathbf{V}_{3i} = \begin{Bmatrix} x_i \\ y_i \\ z_i \end{Bmatrix}_{top} - \begin{Bmatrix} x_i \\ y_i \\ z_i \end{Bmatrix}_{lower} \quad (C.5)$$

Assuming the strains normal to the mid-surface are negligible, the displacement at any point in the element can be defined by the three Cartesian components of the mid-surface node displacement i and two rotations of the modal vector $\mathbf{V}_{3i}$ about orthogonal directions normal to it. The displacement of the element is given by

$$\left\{ \begin{matrix} u \\ v \\ w \end{matrix} \right\} = \sum N_i(\xi,\eta) \left\{ \begin{matrix} u_i \\ v_i \\ w_i \end{matrix} \right\}_{mid} + \sum N_i \zeta \frac{t_i}{2} [\mathbf{v}_{1i} - \mathbf{v}_{2i}] \left\{ \begin{matrix} \alpha_i \\ \beta_i \end{matrix} \right\} \qquad (C.6)$$

where u, v, and w are displacements in the Cartesian coordinate system, t_i is the shell thickness at node i, $\mathbf{v}_{2i}$ and $\mathbf{v}_{1i}$ are orthogonal unit vectors normal to $\mathbf{V}_{3i}$, and α_i and β_i are scalar rotations about the vectors $\mathbf{v}_{2i}$ and $\mathbf{v}_{1i}$, respectively.

As an infinite number of vectors $\mathbf{V}_{2i}$ and $\mathbf{V}_{1i}$ can be generated normal to the vector $\mathbf{V}_{3i}$, a particular scheme has to be devised to ensure a unique definition, and the choice of scheme is quite arbitrary. If $\mathbf{i}$ is a unit vector along the x axis, then

$$\mathbf{V}_1 = \mathbf{i} \times \mathbf{V}_3 \qquad (C.7)$$

Which makes the vector $\mathbf{V}_1$ perpendicular to the plane defined by the direction $\mathbf{V}_3$ and the global x axis. As $\mathbf{V}_2$ has to be orthogonal to both $\mathbf{V}_3$ and $\mathbf{V}_1$, it is given as

$$\mathbf{V}_2 = \mathbf{V}_3 \times \mathbf{V}_1 \qquad (C.8)$$

The required unit vectors $\mathbf{v}_1$, $\mathbf{v}_2$, and $\mathbf{v}_3$ may be formed from the vectors V_1, V_2, and V_3 by dividing them by their scalar length, given by

$$v_i = \frac{V_i}{|V_i|} \quad i = 1,\ 2,\ 3 \tag{C.9}$$

The strains and stresses have to be defined in order to determine the elemental stiffness matrix [k]. If the strains normal to the surface ζ = constant are assumed to be negligible, using the assumptions of Shell Theory, it is necessary that the components of the strain and stress in two orthogonal directions tangent to the surface ζ = constant exist. To establish these directions, a normal z' can be erected to the surface and two other orthogonal axes x' and y', but tangent to the surface. The strain components of interest are then

$$\{\epsilon'\} = \begin{Bmatrix} \epsilon_{x'} \\ \epsilon_{y'} \\ \gamma_{x'y'} \\ \gamma_{x'z'} \\ \gamma_{y'z'} \end{Bmatrix} = \begin{Bmatrix} \dfrac{\partial u'}{\partial x'} \\ \dfrac{\partial v'}{\partial y'} \\ \dfrac{\partial u'}{\partial y'} + \dfrac{\partial v'}{\partial x'} \\ \dfrac{\partial w'}{\partial x'} + \dfrac{\partial u'}{\partial z'} \\ \dfrac{\partial w'}{\partial y'} + \dfrac{\partial v'}{\partial z'} \end{Bmatrix} \tag{C.10}$$

with the strains in the z' direction neglected, so as to be consistent with the Shell Theory assumptions.

The stresses corresponding to these strains are related by the elasticity matrix [D′], such that

$$\{\sigma'\} = \begin{Bmatrix} \sigma_{x'} \\ \sigma_{y'} \\ \tau_{x'y'} \\ \tau_{x'z'} \\ \tau_{y'z'} \end{Bmatrix} = [D']\{\epsilon'\} \tag{C.11}$$

The 5 x 5 matrix [D′] for isotropic materials is given by

$$[D'] = \frac{1}{(1 - \nu^2)} \begin{bmatrix} 1 & \nu & 0 & 0 & 0 \\ & 1 & 0 & 0 & 0 \\ & & \frac{1-\nu}{\nu} & 0 & 0 \\ & & & \frac{1-\nu}{2k} & 0 \\ & \text{sym.} & & & \frac{1-\nu}{2k} \end{bmatrix} \tag{C.12}$$

where E and ν are Young's modulus and Poisson's ratio, respectively. The factor k included in the last two shear terms is a correction to improve the shear displacement approximation and is taken equal to 1.2.

In the standard finite element way, the elemental stiffness matrix may now be determined from

$$[k]_e = \iiint_V [B]^T[D'][B]dxdydz \tag{C.13}$$

where [B] is the so called strain-displacement matrix

$$\{\epsilon'\} = [B]\{\delta\}_e \tag{C.14}$$

and $\{\delta\}_e$ contains the elemental displacements u_i, v_i, w_i, α_i, and β_i for node i. All that remains is to express equation C.13 in terms of the curvilinear coordinates ξ, η, and ζ. This can be accompished by a number of transformations.

Equation C.6 relates the global displacements u, v, and w to the curvilinear coordinates. The derivative of these displacements with respect to the global x, y, and z axes is given by

$$\begin{bmatrix} \frac{\partial u}{\partial x} & \frac{\partial v}{\partial x} & \frac{\partial w}{\partial x} \\ \frac{\partial u}{\partial y} & \frac{\partial v}{\partial y} & \frac{\partial w}{\partial y} \\ \frac{\partial u}{\partial z} & \frac{\partial v}{\partial z} & \frac{\partial w}{\partial z} \end{bmatrix} = [J]^{-1} \begin{bmatrix} \frac{\partial u}{\partial \xi} & \frac{\partial v}{\partial \xi} & \frac{\partial w}{\partial \xi} \\ \frac{\partial u}{\partial \eta} & \frac{\partial v}{\partial \eta} & \frac{\partial w}{\partial \eta} \\ \frac{\partial u}{\partial \zeta} & \frac{\partial v}{\partial \xi} & \frac{\partial w}{\partial \xi} \end{bmatrix} \tag{C.15}$$

where [J] is the Jacobian matrix defined by

$$[J] = \begin{bmatrix} \frac{\partial x}{\partial \xi} & \frac{\partial y}{\partial \xi} & \frac{\partial z}{\partial \xi} \\ \frac{\partial x}{\partial \eta} & \frac{\partial y}{\partial \eta} & \frac{\partial z}{\partial \eta} \\ \frac{\partial x}{\partial \zeta} & \frac{\partial y}{\partial \zeta} & \frac{\partial z}{\partial \zeta} \end{bmatrix} \tag{C.16}$$

which can be expressed in terms of the coordinate definition of equation C.4. Thus, for every set of curvilinear coordinates, the corresponding global displacements may be calculated numerically.

However, a further transformation is needed to relate the local displacement directions x′, y′, and z′ to the global coordinates x, y, and z. The directions of the local axes have to be determined. The vector $\mathbf{V}_3$ defines a vector that is normal to the surface ζ = constant and can be found as the vector product of any two vectors tangent to the surface, such that

$$\mathbf{V}_3 = \begin{Bmatrix} \frac{\partial x}{\partial \xi} \\ \frac{\partial y}{\partial \xi} \\ \frac{\partial z}{\partial \xi} \end{Bmatrix} \times \begin{Bmatrix} \frac{\partial x}{\partial \eta} \\ \frac{\partial y}{\partial \eta} \\ \frac{\partial z}{\partial \eta} \end{Bmatrix} = \begin{Bmatrix} \frac{\partial y}{\partial \xi}\frac{\partial z}{\partial \eta} - \frac{\partial y}{\partial \eta}\frac{\partial z}{\partial \xi} \\ \frac{\partial x}{\partial \eta}\frac{\partial z}{\partial \xi} - \frac{\partial x}{\partial \xi}\frac{\partial z}{\partial \eta} \\ \frac{\partial x}{\partial \xi}\frac{\partial y}{\partial \eta} - \frac{\partial x}{\partial \eta}\frac{\partial y}{\partial \xi} \end{Bmatrix} \tag{C.17}$$

Following the process described above, two perpendicular vectors $\mathbf{V}_2$ and $\mathbf{V}_1$ may be formed and reduced to unit magnitude. A matrix of unit vectors may be formed. This is actually the direction cosine matrix

$$[\theta] = [\mathbf{v}_1, \mathbf{v}_2, \mathbf{v}_3] \tag{C.18}$$

The global derivatives of displacements u, v, and w can be transformed to the local dervatives of the local orthogonal displacements by

$$\begin{bmatrix} \frac{\partial u'}{\partial x'} & \frac{\partial v'}{\partial x'} & \frac{\partial w'}{\partial x'} \\ \frac{\partial u'}{\partial y'} & \frac{\partial v'}{\partial y'} & \frac{\partial w'}{\partial y'} \\ \frac{\partial u'}{\partial z'} & \frac{\partial v'}{\partial z'} & \frac{\partial w'}{\partial z'} \end{bmatrix} = [\theta]^T \begin{bmatrix} \frac{\partial u}{\partial x} & \frac{\partial v}{\partial x} & \frac{\partial w}{\partial x} \\ \frac{\partial u}{\partial y} & \frac{\partial v}{\partial y} & \frac{\partial w}{\partial y} \\ \frac{\partial u}{\partial z} & \frac{\partial v}{\partial z} & \frac{\partial w}{\partial z} \end{bmatrix} [\theta] \tag{C.19}$$

The elemental stiffness matrix [k] may be written in terms of the curvilinear coordinates ξ, η, and ζ as

$$[k]_e = \int_{-1}^{1}\int_{-1}^{1}\int_{-1}^{1} [B]^T [D'] [B] |J| d\xi d\eta d\zeta \tag{C.20}$$

where $|J|$ is the determinate of the Jacobian matrix.

The elemental mass matrix $[m]_e$ may be formed in a similar manner using the shape functions given above, as

$$[m]_e = \int_{-1}^{1}\int_{-1}^{1}\int_{-1}^{1} \rho [N]^T [N] |J| d\xi d\eta d\zeta \tag{C.21}$$

APPENDIX D - DIMENSIONAL ANALYSIS

This appendix will present the details of the dimensional analysis of the model that was performed.

The structure of a ship is very complex and defies rigorous closed-form analysis. Damping, shear, and rotary inertia effects in the ship structure are difficult if not impossible to predict. Thus, it was believed that the only effective way to investigate the dynamic behaviour of the ship hull was to perform experiments with a scaled model, which could be analysed for its vibration characteristics both in air and water. In this way, the experimental results from the model could be compared with various numerical methods, and the accuracy and shortcomings of the various techniques could be determined. For this reason, a simple model was constructed of acrylic, with a constant semicircular cross-section over its length of 96 inches.

In order to construct a model of a ship, many variables had to be considered. Of prime importance was the model's ability to reproduce the dynamic behaviour of the full size ship. However, other issuses were important too, and, as is often the case in model scaling, not all of these issues could be satisfied by the same model. Which of these variables were most important must be determined. As well, the model was often forced to meet physical constraints. It was of no use to construct a model if its size prevented it from being tested or if the detail in the model made the testing so complex that it consumed large amounts of time. And finally, the material of construction needed to be considered. If the model was made of steel, the only way the model could have similar dynamic behaviour as the full size ship was if the dimensions of the model were the same as the ship. Clearly, this was not reasonable. Therefore, another construction material had to be chosen. In order to determine which properties were important and what material should be used, a dimensional analysis [19,25]of the relations that govern the vibration of a ship structure was conducted, as presented below.

The following discussion applies strictly to a simply supported beam of a uniform cross-section. The frequency of vibration is given as

$$\omega_i = \frac{(\beta_i l)^2}{l^2} \left[\frac{EI}{m} \right]^{1/2} \text{Hz} \qquad (D.1)$$

where $\beta_i l$ is a constant that depends on the end conditions of the beam, l is the length of the beam, E is Young's modulus, I is the moment of inertia of the cross-section, and m is the mass per unit length of the beam. Now let the subscribes $_m$ and $_f$ denote the model and full scale ship, respectively, and let the variable K denote the ratio of the full scale variable to the model variable of the term of interest. Then

$$K_{\omega} = \frac{\omega_{i_f}}{\omega_{i_m}} = \frac{l_f^2}{l_m^2} \left[\frac{I_f}{I_m} \frac{E_f}{E_m} \frac{m_m}{m_f} \right]^{1/2} \tag{D.2}$$

or

$$K_{\omega} = \frac{1}{K_L^2} \left[\frac{K_I K_E}{K_M} \right]^{1/2} \tag{D.3}$$

where

$$K_{\omega} = \frac{\omega_{i_f}}{\omega_{i_m}} , \; K_L = \frac{l_f}{l_m} , \; K_I = \frac{I_f}{I_m} , \; K_E = \frac{E_f}{E_m} , \; K_M = \frac{m_m}{m_f} \tag{D.4}$$

The moment of inertia of the cross-section is given as

$$I = I_o + Ad^2 \tag{D.5}$$

which is approximately

$$I = Ad^2 = tLd^2 \tag{D.6}$$

So

$$K_I = \frac{t_f}{t_m} \frac{L_f}{L_m} \frac{d_f^2}{d_m^2} \tag{D.7}$$

which is

$$K_I = K_t K_L^3 \tag{D.8}$$

if the model is geometrically similar except for the shell thickness. Now examine K_M. If the mass of the structure in water can be expressed as

$$m_W = (1 + C) m_S \tag{D.9}$$

then

$$m_s = A\rho \qquad (D.10)$$

which leads to

$$K_M = \frac{A_f}{A_m} \qquad (D.11)$$

Using equations D.8 and D.11, equation D.3 can be expressed as

$$K_R^2 = \frac{K_t K_E}{K_L^3} \qquad (D.12)$$

Appling geometric similarity gives

$$\epsilon_f = \epsilon_m \qquad (D.13)$$

where ϵ is the strain. Note that

$$\epsilon = \frac{\sigma}{E} \qquad (D.14)$$

and that

$$\sigma = \frac{My}{I} \qquad (D.15)$$

where M is the bending moment, and y is the distance from the neutral axis to the point on the section where the stress is to be determined.

Assuming that the beam is simply supported, the bending moment is given by

$$M = \frac{Wl^2}{8} \qquad (D.16)$$

where W is the load per unit length of the beam. W is given by

$$W = \rho A \qquad (D.17)$$

By using equation D.13 and substituting in to it equations D.15, D.16, and D.17, the following equation can be developed

$$K_I = \frac{K_L^5}{K_E} \qquad \text{(D.18)}$$

or

$$K_t = \frac{K_L^2}{K_E} \qquad \text{(D.19)}$$

Thus, the relations that hold are

$$K_R^2 = \frac{K_t K_E}{K_L^3} \qquad \text{(D.12)}$$

and

$$K_t = \frac{K_L^2}{K_E} \qquad \text{(D.19)}$$

which lead to

$$K_R^2 = \frac{1}{K_L} \qquad \text{(D.20)}$$

Some of these parameters are determined by physical limitations. The thickness of the model's hull is determined by size limitations, therefore

$$t_{min} = 0.050"$$

and from the endeavour

$$t_f = 0.5"$$

The length of the model is determined by the size of testing tank, therefore

$$l_{max} = 6' - 10'$$

and from the endeavour

$$l_f = 300'$$

The ratio of the Young's modulus is determined by the materials available. If the material chosen is acrylic, then

$K_E = 50$

and the maximum length of a sheet is eight feet, and the minimum thickness of a sheet of acrylic is 0.079 inches; therefore

$K_L = 37.5$

$K_t = 6.3$

If the cross-section chosen is semi-circular with

D = 8.392"

t = 0.079"

L = 96"

then the full size ship has

Beam = 26′

Length = 300′

(See Figure D.1 for a diagram of the model with dimensions.)

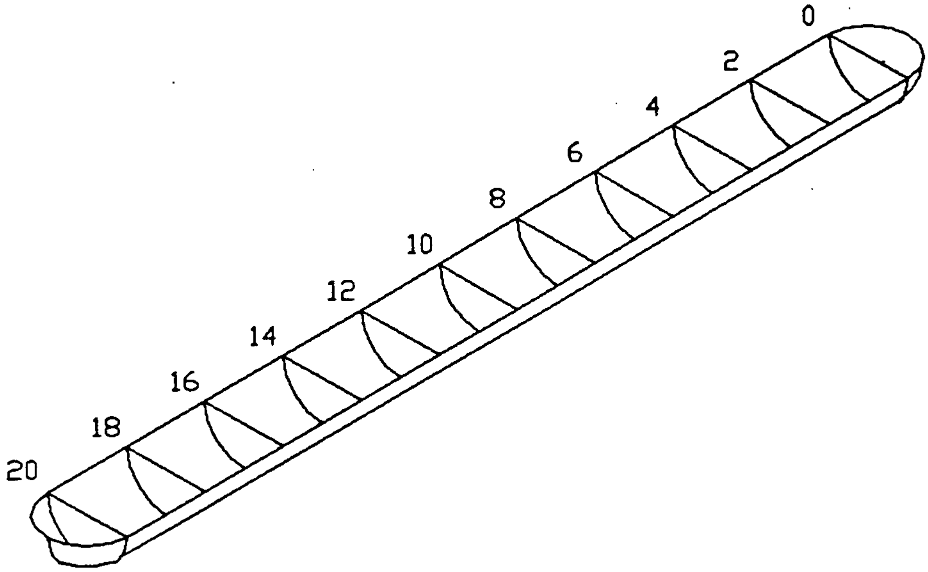

Length (between end bulkheads) 96" (2438mm)

Beam 8.391" (213mm)

Hull Thickness 0.079" (2mm)

Bulkhead - Thickness 0.236" (6mm)

- Diameter 8.3125" (211mm)

Endcaps - Thickness 0.079" (2mm)

- Radius 4.196" (107mm)

Unloaded Weight 5.56 lb (2530 grams)

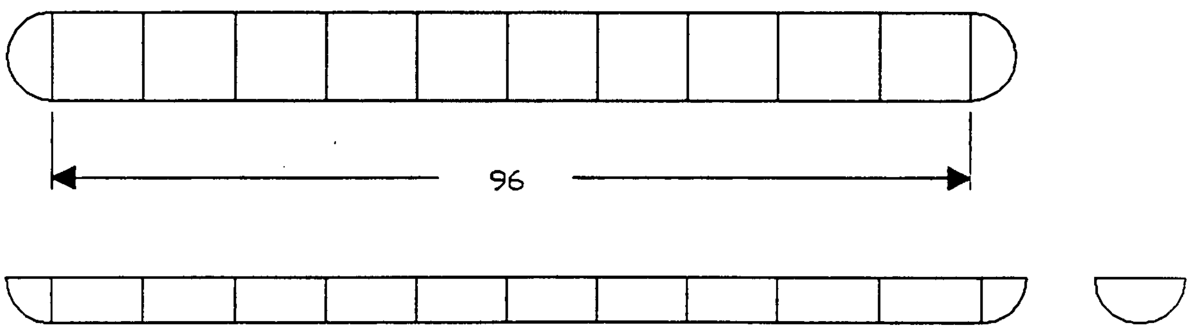

Figure D.1 - Ship Model

APPENDIX E - INSTRUMENTATION LIST

This appendix gives a list of the instrumentation used :

1. Brüel & Kjær Type 4332 Piezoelectric Accelerometer
2. Brüel & Kjær Type 4370 Piezoelectric Accelerometer
3. Brüel & Kjær Type 2635 Charge Preamplifier
4. Brüel & Kjær Type 4291 Accelerometer Calibrator
5. Nicolet 660A Dual Channel FFT Frequency Analyser
6. Tektronix 4662 Digital Plotter
7. Tektronix 5103N Digital Oscilloscope
8. Commodore PC 10-II Personal Computer (IBM Compatible)
9. VAX 11/750 Computer
10. Digital VT 101 Terminal with Retro-Graphics
11. PCB 208 A03 Impact Hammer

APPENDIX F - MODAL ANALYSIS PROGRAM

This appendix will describe the program MAP that was written by the author to assist with the collection and processing of the experimental data. This program was written in Turbo PASCAL on an IBM Personal Computer. The MAP program is a menu driven program with graphic capabilities and needs to be used in conjunction with a Hercules Graphics Card.

To use this program, the disk with the MAP program should be put in drive a and a blank disk or a disk with data files created by the MAP program should be put in drive b. After logging onto the a drive, MAP should be typed to the a:> prompt. This will start the program. The title page will then flash up on the screen. Typing any key will generate the next command. The program will then ask for the input of the file prefix of the file to create or look at. After this point the program will present the main menu. This menu offers the options of : Transfer from fft, Send to fft, Plot mode shape, Hardcopy, Change file group, and Exit. Option one, Transfer from fft, will be highlighted. Moving around in the menu is achieved by pressing the up or down arrow keys. Once the option desired is highlighted, the return key should be pressed.

F.1 Option - Transfer From FFT

This option allows the transfer of information in the Nicolet onto floppy disks for storage and further processing. In this option the baud rate of the transfer may be set. Note that the Nicolet baud rate has to correspond and must be set before any information is processed by the Nicolet. A baud rate of 9600 is the fastest, and it is the default for the MAP program.

Once this option has been choosen the program will ask you which fft is desired for transferral. (Only the Nicolet procedures have been written), the Nicolet fft is the default. Once the Nicolet has been chosen as the fft, the program asks which station this information is for (i.e. Station 0 - 20). Then it asks what the baud rate is (default 9600), and, once the return has been pressed, the transfer is started. The information that is transferred is the data from the Nicolet buffers 0, E, 4, 5, 6, and 7. These buffers contain : front panel settings, average status, averaged channel A power spectrum, averaged cross spectrum real, averaged cross spectrum imaginary, and averaged channel B power spectrum information, respectively. When the information has finished transferring, the program returns to the main menu.

F.2 Option - Send To FFT

This option is very similar to option Transfer from fft; in fact, it is just the opposite.

F.3 Option - Plot Mode Shape

This option will allow two tasks to be performed : 1) Look at data, which mimics the Nicolet functions RMS Spectrum, Transfer Function and Coherence; and 2) Plot the mode shape.

If this option is chosen, the program puts up another menu that asks which task is desired. If the Look at data option is chosen, the program will ask which station is perferred and then which function is desired : RMS spectrum, Transfer function, or Coherence. Once the function is chosen, it is displayed on the screen. A cursor may be moved back and forth, using either the right and left arrow keys or the home and page up keys. The two arrow keys move the cursor one box, while the home and page up keys move the cursor 10 boxes. Exiting from this section is acheived by pressing the enter key.

If the Plot mode shpae option is chosen, the program will ask how many stations there are in the datafile, and what the frequency of interest is. Once these questions have been answered, the program begins to scan the datafile for the correct information, namely the Transfer Funtion and the Phase angle. When the program has scanned throught the datafile it will plot the mode shape on the screen. It will then ask if this mode shape is correct. If it is it will write this information to a file that can be used by LOTUS for further processing. If the mode shpe is not coorect, the program will ask which station is wrong and it will then try to further smooth the data.

F.4 Option - Hardcopy

This option has not been written, but if it was included in the program, it would allow a hard copy of the mode shape and a table listing the tabular mode shape information to be plotted or printed.

F.5 Option - Change File Group

This option allows a change of file prefix while still in the program.

F.6 Option - Exit

This option allows the exit to DOS.

APPENDIX G - MATERICAL PROPERTIES OF ACRYLIC

G.1 Density

The density of the acrylic used to construct the model was determined by weighing a sample with known dimensions. The sample was 12 x 12 inches, 0.079 inches (2 mm) thick, and weighed 0.00324 lb. Its density was $\rho = 0.0369\ \text{lb/in}^3$ or $9.55\text{x}10^{-5}\ \text{lb.sec}^2/\text{in}^4$, given as

$$\rho = \frac{F}{gV}$$

where ρ is the density of acrylic, F is the force or weight (lbs), g is the acceleration of gravity, and V is the sample's volume.

G.2. Determination of Young's Modulus

Three different tests were performed to determine Young's modulus. The first test involved taking a sample of the acrylic that the hull was made of and mounting two strain gauges on it. This sample was then put into pure bending (as shown in Figure G.1). In this configuration, readings from the strain

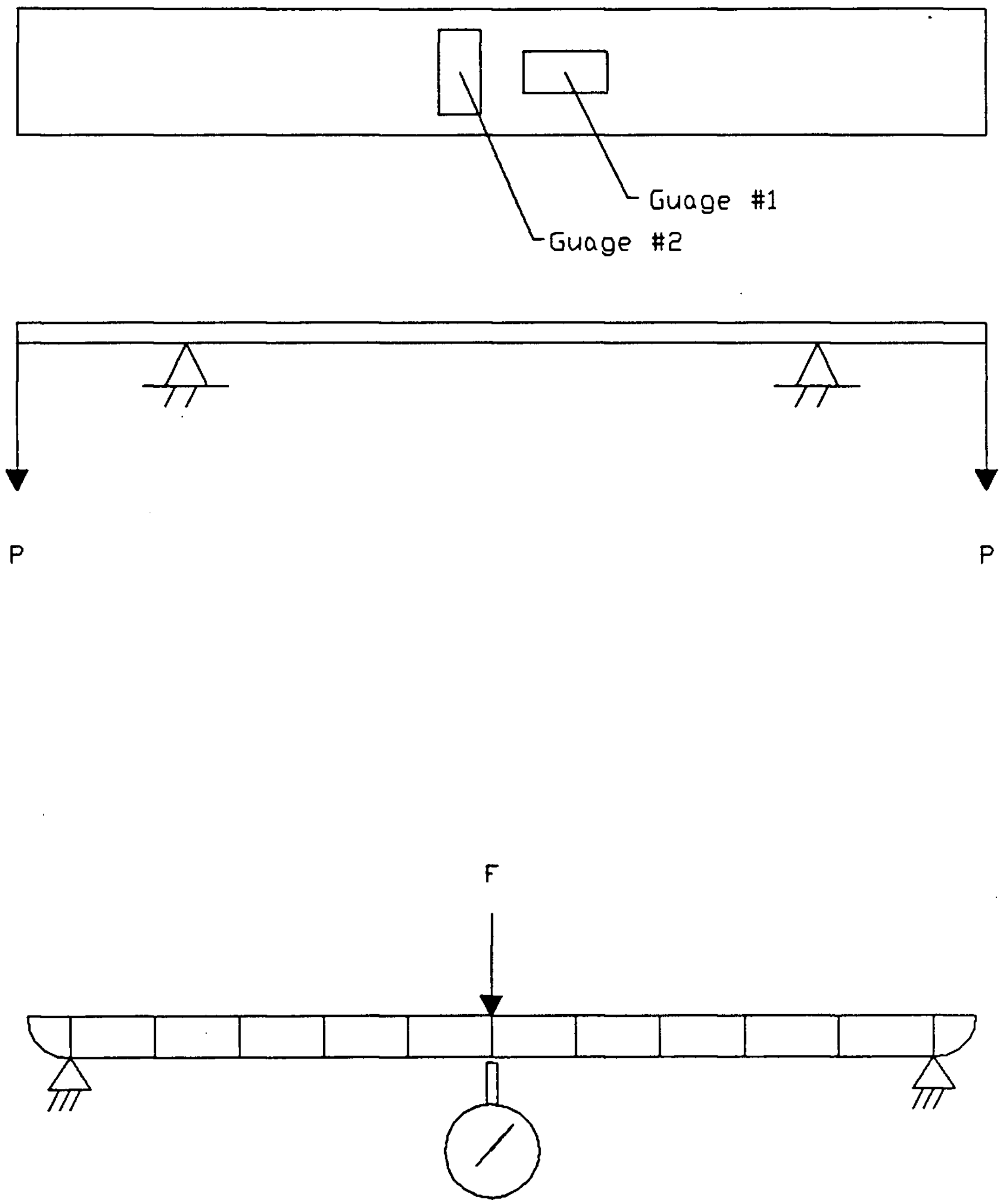

Figure G.1 - Strain-Guage Set Up and Bending Test of Ship Model gauges were measured and recorded (as shown in Table G.1).

	Strain					
Load grams	Gauge#1 $\mu\epsilon$	Gauge#2 $\mu\epsilon$	Moment lbs•in	Stress psi	E psi	υ
0	0	0	0	0	-	-
157	432	-162	1.99	214	495545	0.375
270	762	-278	3.42	368	483144	0.365
385	1106	-410	4.88	525	474650	0.371
498	1458	-526	6.31	679	465736	0.361
613	1780	-656	7.77	836	469579	0.369
726	2140	-778	9.21	990	462584	0.364
841	2476	-908	10.66	1147	463141	0.367
954	2832	-1028	12.10	1300	459328	0.363
841	2554	-934	10.66	1147	448997	0.366
726	2202	-806	9.21	990	449560	0.366
613	1896	-694	7.77	836	440850	0.366
498	1528	-560	6.32	679	444400	0.367
385	1216	-448	4.88	525	431713	0.368
270	854	-320	3.42	368	431096	0.375
157	534	-202	1.99	214	400890	0.378
0	82	-70	0	0	-	-

Table G.1 - Results from Strain-Gauge Test

Using these results, Young's modulus and Poisson's ratio were determined from

$$E = \frac{6Pl}{bh^2 \epsilon_x}$$

where E was Young's modulus, P was the load, l was the length between the load and the support (which was 5.750 inches), b was the width of the sample (b = 1.00 inches), h was the thickness of the sample (h = 0.23622 inches (6mm)), and ϵ_x was the strain on gauge # 1. Poisson's ratio was given by

$$\upsilon = - \frac{\epsilon_y}{\epsilon_x}$$

with ϵ_y = strain from gauge # 2. The average Young's modulus was E = 455,541 psi, and the average Poisson's ratio was $\upsilon = 0.368$.

The second method involved simply supporting the actual ship model at both ends, loading it in the middle, and then measuring the deflection. Then, a finite element model was run, and Young's modulus was varied until the results for the deflection matched the experimental results.

Weight lb	Deflection inches
1	0.021
2	0.042
3	0.065
4	0.085
5	0.105

Table G.2 - Results for Deflection

This method resulted in a Young's modulus of 302,000 psi.

The third method was a dynamic test. Strain gauge # 1 was connected to the Nioclet 660A FFT analyser, and the piece of acrylic was simply supported and made to vibrate in its first mode by an impulse in the middle of the beam. The frequency for the first mode was determined (by examining Figure G.2) as

$\omega_1 = 29.25$ Hz

From this information, and using the expression

$$\omega = \frac{1}{2\pi}\left(\frac{\beta_1 l}{l}\right)^2\sqrt{\frac{EI}{\mu}}$$

Young's modulus was determined to be 622,056 psi.

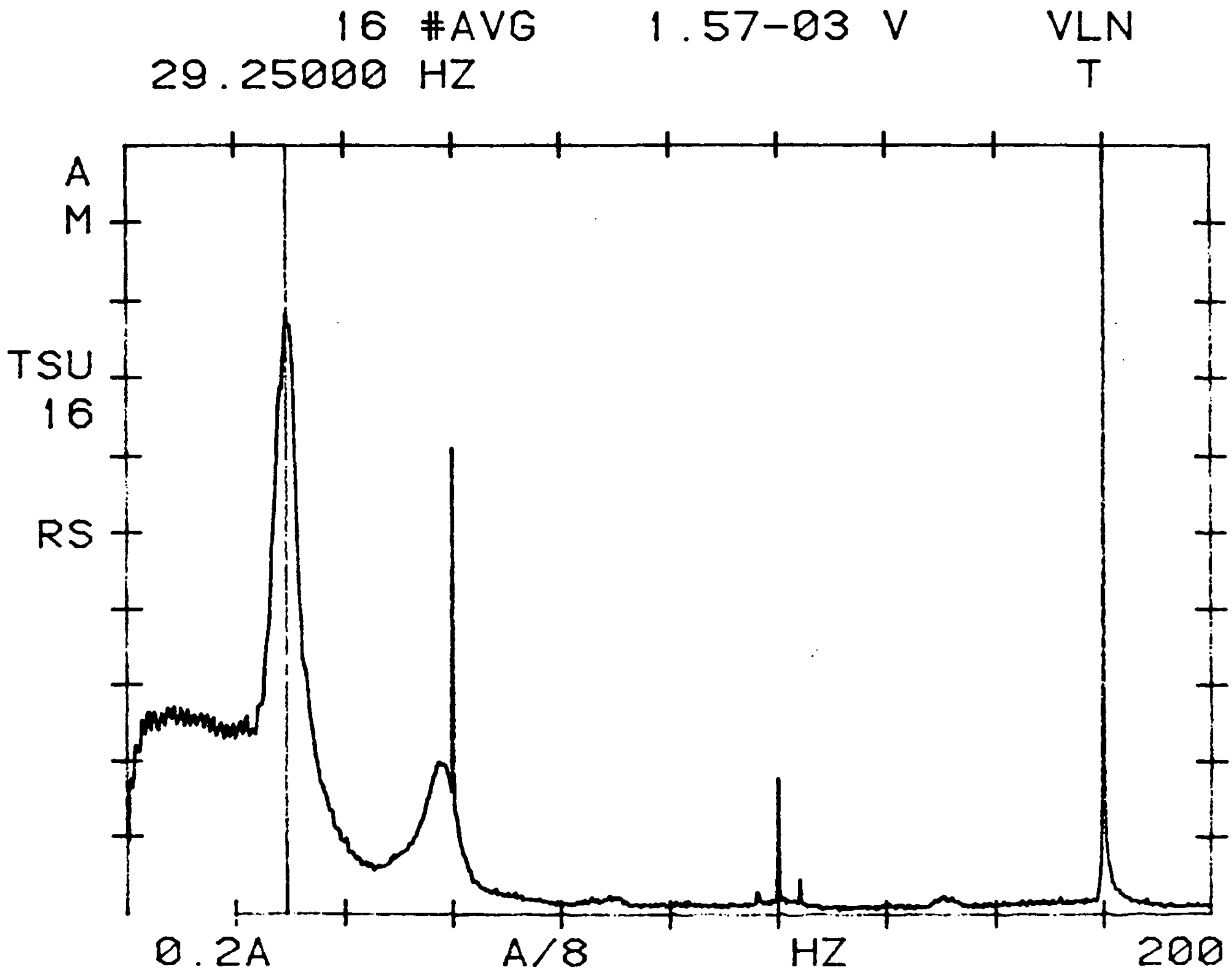

Figure G.2 - Natural Frequency of Simply Supported Beam